Universidad Autónoma de Madrid
Departamento de Física Teórica

Study of the internal structure of Jets and Measurement of the Inclusive and Dijet Cross Sections in Charged Current DIS at HERA

Trabajo de Investigación
por D. Mónica Luisa Vázquez Acosta

Directores : D. Jose del Peso Malagón
D. Juan Terrón Cuadrado

Dedico este trabajo a mis padres. Gracias a su dedicación y sacrificio he podido llegar tan lejos ...

Abstract

The hadronic final state in charged current deep inelastic ep scattering in the kinematic range $Q^2 > 200$ GeV^2 and $y < 0.9$ has been studied with the ZEUS detector at HERA using an integrated luminosity of 44.97 pb^{-1}. Events having one or more jets with transverse energies $E_T^{jet} > 8$ GeV in the final state have been selected using the longitudinally-invariant k_T algorithm in the laboratory frame. The inclusive jet and dijet cross sections have been measured as a function of E_T^{jet} and η^{jet}. The internal structure of the jets has been studied in terms of the jet shape and the mean subjet multiplicity. The data has been compared with leading-order perturbative QCD calculations convoluted with the CTEQ4 parametrisations of the proton parton density functions. The inclusive jet cross sections and the internal structure of jets are well described by LO predictions. LO QCD calculations describe well the shape of the measured dijet cross section but fail to describe the measured normalisation.

The results of this manuscript (see chapter 7) , have been presented by the author in the Photon'2001 conference in Ascona. Furthermore, they have been published by ZEUS as a contributed paper to the International Europhysics Conference on High Energy Physics, Budapest, Hungary (2001) [ZE01].

Contents

1 Introduction **15**

1.1 The Standard Model 15

1.2 Deep Inelastic Scattering 18

1.2.1 Kinematic Variables for Lepton Nucleon Scattering 18

1.2.2 Reconstruction of Kinematics 19

1.2.3 Cross Sections and Proton Structure Functions 20

1.3 The Quark Parton Model 22

1.4 QCD 24

1.4.1 Factorization 25

1.4.2 QCD evolution equations 26

1.5 Photoproduction 29

2 The HERA collider and the ZEUS detector **31**

2.1 The Hadron Electron Ring Accelerator 31

2.2 The ZEUS Detector 33

2.2.1 The Central Tracking Detector 36

2.2.2 The Uranium-Scintillator Calorimeter (UCAL) 37

2.3 The Luminosity measurement 39

2.4 The ZEUS trigger and data acquisition systems 40

2.5 Event reconstruction and analysis 41

3 Jets **45**

3.1 Jets in QCD 45

3.2 Jet Finders 45

3.2.1 The Snowmass Convention 47

3.2.2 Cone Algorithm 47

3.2.3 Clustering Algorithms 48

3.3 Jet Internal Structure 48
3.3.1 Jet Shapes 49
3.3.2 Subjets 51
3.4 Jet production in DIS at HERA 51

4 Data Selection **53**
4.1 The $\not{p}_t$ threshold and background events 53
4.2 Online Event Selection - Trigger Logic 54
4.2.1 First Level Trigger 54
4.2.2 Second Level Trigger 55
4.2.3 Third Level Trigger 56
4.3 Offline Event Selection 57
4.3.1 General Selection 57
4.3.2 Rejection of NC DIS events 58
4.3.3 Uranium-noise and spark suppression 58
4.4 Jet selection 59
4.5 Kinematic cuts 59
4.6 Charged Current event sample 60

5 Event and Detector Simulation **63**
5.1 Monte Carlo Models 64
5.2 Description of Data by the Simulation 65

6 Analysis Method **71**
6.1 Resolution in jet and kinematic variables 71
6.1.1 Jet Energy Correction 72
6.1.2 Correction of the Kinematic Variables 74
6.2 Correction of measured distributions 78
6.2.1 Determinatin of of cross sections 79
6.2.2 Determination of the corrected distributions in jet internal structure variables 81
6.3 Study of Systematic Uncertainties 81

7 Results **89**

8 Conclusions **103**

List of Figures

1.1 Kinematics of ep scattering - the scattering follows through the exchange of a gauge boson (γ^*, Z^0 or $W^{\pm}$). The lowest-order Feynman diagram for DIS is shown. The four-momenta of the particles are given in brackets. 18

1.2 Factorization: separation of the short-ranged and long-ranged physics. The parton distributions in the hadrons cannot be perturbatively calculated (long-ranged physics). The hard cross section $\sigma_{ij}(Q^2)$ is perturbatively calculable (short-ranged physics). 26

1.3 The proton structure function F_2 pictured assuming different compositions for the proton. The two top pictures show the case of QPM. The two bottom pictures show the modifications induced by QCD effects. 27

1.4 Measurement of the structure function F_2 as a function of Q^2 for different values of x. The F_2 measurements different values of x have been scaled by constant factors for display purposes. The evolution of the structure functions through the DGLAP equations are also shown. . . 28

2.1 View of DESY. 31

2.2 The HERA accelerator complex. Four experiments are located in the experimental halls : South (ZEUS), West (HERA-B), North (H1), and East (HERMES). 32

2.3 Integrated luminosity delivered by HERA in the different running periods (left plot) and the one taken with the ZEUS detector (right plot). The latter is used for physics analysis. 34

2.4 View of the ZEUS detector along the beam direction. 34

2.5 View of the ZEUS detector perpendicular to the beam direction. See text for a description of the components. 35

2.6 Layout of a CTD octant. Each octant has nine superlayers with the even numbered ones declined with respect to the beam axis (‘Stereo angle’). 37

2.7 Layout of a FCAL module The UCAL modules are subdivided into one electromagnetic (EMC) and two hadronic (HAC1,HAC2) sections, which in turn are divided into cells. A cell is read out on two opposite sides by one wavelength shifter each. 38

2.8 Location of ZEUS detectors in negative Z-direction. Shown are the gamma (LUMIG) and electron detectors (LUMIE) used for the luminosity measurement. 39

2.9 Schematic diagram of the ZEUS trigger and data acquisition systems. 41

2.10 Interrelationship of the ZEUS offline and Monte Carlo (MC) simulation programs. 42

3.1 Schematic diagram of a typical analysis using jets [Se95]. In the upper line the partons are produced from the hard scattering process and then radiate other partons (parton shower). Color-singlet states (hadrons) are produced through the process of hadronization. The hadrons deposit energy in the detector. At each stage the jet finding can be applied. From the measured data by the detector one can correct backwards, in principle, down to the parton level. 46

3.2 Gluon radiation within a jet. 49

3.3 Differential (left) and integrated (right) jet shape definitions 50

3.4 The internal structure of jets can be studied by resolving jet-like structures ("subjets"). As the resolution scale y_{cut} decreases an increasing number of "subjets" is resolved. 50

3.5 Feynman diagrams of different processes in Charged Current interactions at HERA: i) Born, ii) QCD-Compton and c) boson-gluon fusion processes. 51

3.6 An example of production of a new particle in Charged Current DIS. . 52

4.1 Lines of constant p_t, γ_h and y in the (x, Q^2) kinematic plane. 54

4.2 Example of a charged current one-jet event registered with the ZEUS detector. The energy and position measurements of the uranium calorimeter and the central tracking chamber for the event are displayed in the left side of the plot, where the $r - Z$ projection is shown. The right side of the figure shows the transverse energy deposits in the calorimeter as viewed in the $\eta - \phi$ plane. 61

4.3 Example of a charged current dijet event registered with the ZEUS detector. The energy and position measurements of the uranium calorimeter and the central tracking chamber for the event are displayed in the right side of the plot, where the $r-Z$ projection is shown. The left side of the figure shows the transverse energy deposits in the calorimeter as viewed in the $\eta - \phi$ plane. 62

5.1 Distributions of the kinematic variables Q^2, x and y reconstructed with the Jacquet-Blondel Method. The transverse momentum (p_t) measured with the CAL is also shown. The points are the ZEUS data and the solid(dashed) lines represent the ARIADNE(MEPS) Monte Carlo simulations. The Monte Carlo predictions are normalised to the data points. 66

5.2 Distributions of calorimeter quantities: the ratio of the total transverse momentum over the total transverse energy ($\not{p}_t/E_t$), the ratio of the total transverse momentum excluding the first ring of the FCAL over the total transverse momentum ($\not{p}_t^{-1r}/\not{p}_t$) and the ratio of the transverse energy of the calorimeter cell with highest transverse energy over the total transverse energy (E_t^{max}/E_t^{cal}). The distribution of the $E-P_z$ measured with the CAL is also shown. The points are the ZEUS data and the solid (dashed) lines represents the ARIADNE (MEPS) Monte Carlo simulations. The Monte Carlo predictions are normalised to the data points. 67

5.3 Distributions of tracking quantities measured with the CTD: the number of *good tracks*, the absolute difference between the azimuthal angle of the net momentum calculated with *good tracks* and the azimuthal angle measured by the calorimeter ($|\phi_{cal} - \phi_{track}|$), the ratio of the transverse momentum calculated with *good tracks* and the calorimeter ($\not{p}_t^{\text{good tracks}}/\not{p}_t^{cal}$) and the Z_{vertex} distribution. The points are the ZEUS data and the solid (dashed) lines represents the ARIADNE (MEPS) Monte Carlo simulations. The Monte Carlo predictions are normalised to the data points. 68

5.4 Distributions of the transverse energy (E_T^{jet}) and pseudorapidity (η^{jet}) of the jets reconstructed with the calorimeter. The points are the ZEUS data and the solid (dashed) lines represents the ARIADNE (MEPS) Monte Carlo simulations. The Monte Carlo predictions are normalised to the data points. 69

6.1 The distributions of $(E_T^{had} - E_T^{cal})/E_T^{cal}$, $\eta_{jet}^{had} - \eta_{jet}^{cal}$ and $\phi_{jet}^{had} - \phi_{jet}^{cal}$ using the ARIADNE MC sample. 73

6.2 The mean value $< E_T^{cal}(jet) >$ as a function of $E_T^{had}(jet)$ in different η^{jet} bins. The fits with the functional form $P_0 + P_1 \cdot < E_T^{cal} >$ as well as the values of the parameters are also shown. 74

6.3 The mean value $< E_T^{had} - E_T^{cal}/E_T^{cal} >$ as a function of η_{jet} (left) and ϕ_{jet} (right) before (top) and after (bottom) jet transverse energy corrections are applied. The ARIADNE MC sample has been used. . . . 75

6.4 The distribution of $(Q^2_{TRUE} - Q^2_{JB})/Q^2_{TRUE}$ (left) and the mean value $< (Q^2_{TRUE} - Q^2_{JB})/Q^2_{TRUE} >$ as a function of η_{jet}^{had} before (top) and after (bottom) energy corrections are applied. 76

6.5 The value of $log < Q^2_{JB} >$ as a function of $logQ^2_{TRUE}$ in different η^{jet} bins. The fits with the functional form $P_0 + P_1 \cdot logQ^2_{TRUE}$ as well as the values of the parameters are shown. 77

6.6 The distribution of $(y_{TRUE} - y_{JB})/y_{TRUE}$ before (left) and after (right) energy corrections are applied. 78

6.7 Efficiency (left) and Purity (right) of the E_T^{jet} distribution in inclusive jet CC DIS. The ARIADNE (solid lines) and MEPS (dashed lines) MC samples have been used. 78

6.8 Efficiency (left) and Purity (right) of the η^{jet} distribution in inclusive jet CC DIS. The ARIADNE (solid lines) and MEPS (dashed lines) MC samples have been used. 80

6.9 Systematic uncertainties of the measured inclusive jet cross section as a function of E_T^{jet}. The shaded band shows the statistical uncertainty of the data. a) the transverse energy of the jets, E_T^{jet}, is varied by $\pm 3\%$ b) the cut $\not{p}_t$ is raised from 11 to 12 GeV c) The Monte Carlo LEPTO-MEPS is used instead of ARIADNE-CDM to correct the data to hadron level d) The MRSA set of proton PDFs is used instead of the CTEQ4 set. 83

6.10 ystematic uncertainties of the measured inclusive jet cross section as a function of η^{jet}. The shaded band shows the statistical uncertainty of the data. a) the transverse energy of the jets, E_T^{jet}, is varied by $\pm 3\%$ b) the cut $\not{p}_t$ is raised from 11 to 12 GeV c) The Monte Carlo LEPTO-MEPS is used instead of ARIADNE-CDM to correct the data to hadron level d) The MRSA set of proton PDFs is used instead of the CTEQ4 set. 84

6.11 Systematic uncertainties of the measured mean subjet multiplicity as a function of y_{cut}. The shaded band shows the statistical uncertainty of the data.a) the transverse energy of the jets, E_T^{jet}, is varied by $\pm 3\%$ b) the energy in the CAL is varied by $\pm 3\%$ c) the cut $\not{p}_t$ is raised from 11 to 12 GeV d) The Monte Carlo LEPTO-MEPS is used instead of ARIADNE-CDM to correct the data to hadron level. 85

6.12 Systematic uncertainties of the measured mean subjet multiplicity as a function of η^{jet}. The shaded band shows the statistical uncertainty of the data.a) the transverse energy of the jets, E_T^{jet}, is varied by $\pm 3\%$ b) the energy in the CAL is varied by $\pm 3\%$ c) the cut $\not{p}_t$ is raised from 11 to 12 GeV d) The Monte Carlo LEPTO-MEPS is used instead of ARIADNE-CDM to correct the data to hadron level. 86

6.13 Systematic uncertainties of the measured mean subjet multiplicity as a function of E_T^{jet}. The shaded band shows the statistical uncertainty of the data.a) the transverse energy of the jets, E_T^{jet}, is varied by $\pm 3\%$ b) the energy in the CAL is varied by $\pm 3\%$ c) the cut $\not{p}_t$ is raised from 11 to 12 GeV d) The Monte Carlo LEPTO-MEPS is used instead of ARIADNE-CDM to correct the data to hadron level. 87

7.1 Measured mean subjet multiplicity corrected to hadron level, $< n_{sbj} >$, as a function of y_{cut}, for jets in the η^{jet} range between -1 and 2 in different E_T^{jet} regions (black dots). The error bars show the statistical and systematic uncertainties added in quadrature. For comparison, the predictions of the Monte Carlo models of CDM (solid line) and MEPS (dashed line) are shown. 92

7.2 Measured mean subjet multiplicity corrected to hadron level, $< n_{sbj} >$, as a function of y_{cut}, for jets in the E_T^{jet} range above 8 GeV in different η^{jet} regions (black dots). The error bars show the statistical and systematic uncertainties added in quadrature. For comparison, the predictions of the Monte Carlo models of CDM (solid line) and MEPS (dashed line) are shown. 93

7.3 Measured mean subjet multiplicity corrected to hadron level at a fixed value of $y_{cut} = 10^{-2}$ as a function of η^{jet} for jets with $E_T^{jet} > 8$ GeV (black dots). The error bars show the statistical and systematic uncertainties added in quadrature. For comparison, the predictions of the Monte Carlo models of CDM (solid line) and MEPS (dashed line) are shown. 94

7.4 Measured mean subjet multiplicity corrected to hadron level at a fixed value of $y_{cut} = 10^{-2}$ as a function of E_T^{jet} for jets with $-1 < \eta^{jet} < 2$ (black dots). For comparison, $< n_{sbj} >$ as a function of E_T^{jet} for NC DIS (open squares) at a fixed $y_{cut} = 10^{-2}$ is also shown. 94

7.5 Measured integrated jet shape corrected to hadron level, $\Psi(r)$, for jets with $E_T^{jet} > 8$ GeV and η^{jet} between -1 and 2 (black dots). For comparison, the predictions of the Monte Carlo models of CDM (solid line) and MEPS (dashed line) are shown. 95

7.6 Measured differential jet shapes corrected to hadron level, $\rho(r)$, in CC DIS for jets with $-1 < \eta^{jet} < 2$ in different E_T^{jet} regions (open circles). For comparison, a similar measurement in NC DIS (open squares) is shown. 96

7.7 Measured differential inclusive jet cross-section $d\sigma/dE_T^{jet}$ in CC DIS integrated over $-1 < \eta^{jet} < 2$ in the kinematic region defined by $Q^2 > 200$ GeV^2 and $y < 0.9$ (black dots). The inner error bars represent the statistical uncertainties of the data and the outer error bars show the statistical and the uncorrelated systematic uncertainties added in quadrature. The shaded band displays the uncertainty due to the correlated systematics. For comparison, the predictions of the Monte Carlo models of CDM (solid line) and MEPS (dashed line) are shown. In the lower part of the figure the ratio of the measured $d\sigma/dE_T^{jet}$ over the CDM Monte Carlo prediction is shown. 97

7.8 Measured differential inclusive jet cross-section $d\sigma/dE_T^{jet}$ in CC DIS integrated over $-1 < \eta^{jet} < 2$ in the kinematic region defined by $Q^2 > 200$ GeV^2 and $y < 0.9$ (black dots). For comparison the inclusive jet cross-section $d\sigma/dE_T^{jet}$ in NC interactions (black squares) for $Q^2 > 125$ GeV^2 is shown. The inner error bars represent the statistical uncertainties of the data and the outer error bars show the statistical and the uncorrelated systematic uncertainties added in quadrature. The shaded band displays the uncertainty due to the correlated systematics. The prediction of the Monte Carlo model of CDM (solid line) is shown. 98

7.9 Measured differential inclusive jet cross-section $d\sigma/d\eta^{jet}$ in CC DIS integrated over $E_T^{jet} > 8$ GeV in the kinematic region defined by $Q^2 > 200$ GeV^2 and $y < 0.9$ (black dots). The inner error bars represent the statistical uncertainties of the data and the outer error bars show the statistical and the uncorrelated systematic uncertainties added in quadrature. The shaded band displays the uncertainty due to the correlated systematics. For comparison, the predictions of the Monte Carlo models of CDM (solid line) and MEPS (dashed line) are shown. In the lower part of the figure the ratio of the measured $d\sigma/d\eta^{jet}$ over the CDM Monte Carlo prediction is shown. 99

7.10 Measured differential dijet jet cross-section $d\sigma/dE_T^{jet}$ integrated over $-1 < \eta^{jet} < 2$ in the kinematic region defined by $Q^2 > 200$ GeV^2 and $y < 0.9$ (black dots). The inner error bars represent the statistical uncertainties of the data, and the outer error bars show the statistical and the uncorrelated systematic uncertainties added in quadrature. The shaded band displays the uncertainty due to the correlated systematics. For comparison, the predictions of the Monte Carlo models of CDM (solid line) and MEPS (dashed line) are shown. In the lower part of the figure the ratio of the measured $d\sigma/dE_T^{jet}$ over the CDM Monte Carlo prediction is shown. 100

7.11 Measured differential dijet cross-section $d\sigma/d\eta^{jet}$ integrated over $E_T^{jet} > 8$ GeV in the kinematic region defined by $Q^2 > 200$ GeV^2 and $y < 0.9$ (black dots). The inner error bars represent the statistical uncertainties of the data and the outer error bars show the statistical and the uncorrelated systematic uncertainties added in quadrature. The shaded band displays the uncertainty due to the correlated systematics. For comparison, the predictions of the Monte Carlo models of CDM (solid line) and MEPS (dashed line) are shown. In the lower part of the figure the ratio of the measured $d\sigma/d\eta^{jet}$ over the CDM Monte Carlo prediction is shown. 101

7.12 Measured differential dijet cross-section $d\sigma/dm_{JJ}$ integrated over $-1 < \eta^{jet} < 2$ and $E_T^{jet} > 8$ GeV in the kinematic region defined by $Q^2 > 200$ GeV^2 and $y < 0.9$ (black dots). The inner error bars represent the statistical uncertainties of the data and the outer error bars show the statistical and the uncorrelated systematic uncertainties added in quadrature. The shaded band displays the uncertainty due to the correlated systematics. For comparison, the predictions of the Monte Carlo models of CDM (solid line) and MEPS (dashed line) are shown. In the lower part of the figure the ratio of the measured $d\sigma/dm_{JJ}$ over the CDM Monte Carlo prediction is shown. 102

Chapter 1

Introduction

1.1 The Standard Model

Particle physics studies the particles and their interactions. The elementary constituents of matter are quarks and leptons. They are fermions, with spin $1/2$ (spin is the intrinsic angular momentum of particles and is given in units[1] of $\hbar$).

There are six (known) leptons and six quarks. The leptons are : electron (e), muon (μ), tau (τ), electron neutrino (ν_e), muon neutrino (ν_μ) and tau neutrino (ν_τ). The quarks are : up quark (u), down quark (d), charm quark (c), strange quark (s), top quark (t) and bottom quark (b). For each particle, there exists a corresponding anti-particle with the same mass but opposite quantum numbers (see table 1.1).

There are four known fundamental interactions/forces in nature. In quantum field theory these forces are mediated by gauge bosons. The four known interactions are :

1. the Electromagnetic Interaction
   The Electromagnetic Force is the interaction occurring between particles which carry *electrical charge*, shortly *charged* particles. The gauge boson that mediates the electromagnetic force is the photon γ. Photons are massless and electrically neutral.

2. the Weak Interaction
   The Weak Force acts between fermions (spin $1/2$ particles) and is mediated via the $W^{\pm}$ and Z^0 gauge bosons. These gauge bosons are massive[2].

3. the Strong Interaction
   The Strong Force couples particles having *strong colour-charge*, or shortly *colour*. In this case the gauge bosons are the *gluons*. Gluons themselves are massless but carry colour-charges and are subject to the strong interaction.

4. the Gravitational Interaction
   The Gravitational Force is the force which acts between all particles. In quan-

[1] $\hbar = 6.58 \cdot 10^{-25} s \cdot GeV$

[2] The W-boson has a mass of 80.422 ± 0.047 GeV and the Z^0 boson 91.1876 ± 0.0021 GeV.

tum theories of the gravity, the gravitational field is mediated by a spin two ($s = 2$) boson which is called *Graviton*.

This interaction is the weakest of the four interactions and is long-ranged. Due to the weakness of this force, it can be neglected at present energies available in high energy physics experiments.

The Strong and the Weak Force are short-ranged and play a role only at sub-nuclear distances, in contrast to the long-ranged electromagnetic and gravitacional forces.

	Families			electric charge	Forces str	em	weak	grav
Quarks	u	c	t	$2/3$	$\times$	$\times$	$\times$	$\times$
	d	s	b	$-1/3$	$\times$	$\times$	$\times$	$\times$
Leptons	ν_e	ν_μ	ν_τ	0	-	-	$\times$	$\times$
	e	μ	τ	-1	-	$\times$	$\times$	$\times$

Masses of Quarks (MeV)					
d	u	s	c	b	t
< 100	< 100	~ 400	~ 1500	~ 5000	~ 150000

Table 1.1 - Generations of fermions in the Standard Model. The electrical charge of the particles is shown and the interactions they undergo. The symbol $\times$ means that the particles are subjet to the specific force, whereas $-$ indicates that the particles do not interact via that force. In the second table estimations of the masses of the quarks are given.

Quantum Electrodynamics (QED) is the theory of electromagnetic interactions. The results of QED can be calculated using perturbation theory since the electromagnetic coupling constant $\alpha \simeq 1/137$ is much smaller than unity. At larger distances the effective charges are less than the real ones. This is due to screening effects (charges emitt and absorb virtual photons which, in turn, fluctuate in electron-positron pairs). Therefore, at small distances (large energy scales) the electromagnetic coupling constant increases. For large scales / small distances the electromagnetic coupling constant increases. For the present energy scales in high energy physics (HEP) experiments α is small enough that the perturbative approach can be applied.

Strong interactions are described by Quantum Chromodynamics (QCD). The mediators of the strong interaction, the gluons, carry colour. Colour plays for the strong interaction the role of the charge in the electromagnetics interactions. Gluons interact between themselves strongly as opposed to the field quanta of the electromagnetic interactions (photons). Due to this fact the strong coupling constant α_s decreases as the energy scale increases (small distances). Calculation of results in QCD using perturbative methods is not always possible. In fact perturbative QCD (pQCD) cannot be always applied and its use depends also on the particular process for which the calculations are made. In contrast to the electromagnetic coupling constant α, the strong coupling constant α_s decreases as the scale increases. Some aspects

of QCD will be described in this chapter. Both QED and QCD are quantum field theories.

The electromagnetic and weak interactions are unified within the electroweak theory (EW) of Glashow, Salam and Weinberg [Gl61]. The combination of the Electroweak Theory with QCD constitutes the *Standard Model* (SM). In the context of this model the 12 elementary fermions (quarks and leptons) are classified in the Standard Model in three families (generations). The masses of the particles vary between families, but the way the particles interact remains the same (see also table 1.1).

The QCD and the electroweak theory are gauge theories[3] and can be derived from symmetry principles. For the strong interaction, the basic symmetry is $\mathrm{SU}(3)$, where the "3" refers to the three colour-charges, while for the electroweak interaction the basic symmetry is $\mathrm{SU}(2) \bigotimes \mathrm{U}(1)$.

Experimental evidence from a large number of high energy experiments has shown an overwhelming success of the Standard Model. Fundamental tests of its correctness have been made and precise determinations of its free parameters have been done. In spite of these successes, there are still many open questions concerning the Standard Model.

Some of the problems and still unresolved questions are listed below :

- *Quark Confinement* : the fact that no free quarks have been observed is not explained by the Standard Model (in particular by QCD).
- The Standard Model does not predict the masses of quarks and leptons.
- The existence of exactly three families of quarks and leptons is not predicted by the Standard Model.
- The scale of Quantum Gravity is not yet understood. The Standard Model cannot predict why this scale is so different from that of the electroweak scale.
- One of the main still unsolved questions in the Standard Model / High Energy Physics is the existence of the Higgs Boson. Its existence is related to the generation of elementary particle masses. Gauge bosons and fermions obtain their masses by interacting with the Higgs field. Associated with this mechanism is the existence of massive scalar particles called Higgs bosons. The proof for the Higgs mechanism would come directly from the observation of the Higgs particle. A clear experimental observation of the Higgs bosons has not yet been made. The LEP experiments at CERN[4] have observed a number of collisions compatible with the production of a Higgs particle with a mass of around 115 GeV. However, these events were also compatible with other known processes [LE00].
- The Standard Model failes to account for the solar and atmospheric neutrino data which strongly indicate the need for neutrino conversions, as would arise from neutrino-mass-induced oscillations [Ne00].

[3] The equations of the interactions are invariant under a gauge transformation

[4] CERN - **C**onseil **E**uropéen pour la **R**echerche **N**ucléaire - Switzerland.

1.2 Deep Inelastic Scattering

Many aspects of the Standard Model have been discovered in the deep inelastic lepton-hadron scattering (DIS). The first experimental evidence for the structure of the proton came from such experiments performed at the High Energy Physics Laboratory at Stanford University in the early 1950s [Ho53].

In the following section the kinematics of ep scattering is described in detail.

1.2.1 Kinematic Variables for Lepton Nucleon Scattering

The scattering of positrons (electrons) off protons proceeds through the exchange of a gauge boson : γ^* or Z^0 in the case of Neutral Current (NC) interactions and $W^{\pm}$ in the case of Charged Current (CC) interactions (in this case the incoming positron is converted into an anti-neutrino). In this section the kinematic variables are defined. The ep collision can be viewed as a $\gamma^* p$ ($Z^0 p, W^{\pm} p$) collision with the lepton emitting the gauge photon. A Feynman diagram for the single gauge-boson exchange process is depicted in figure 1.1.

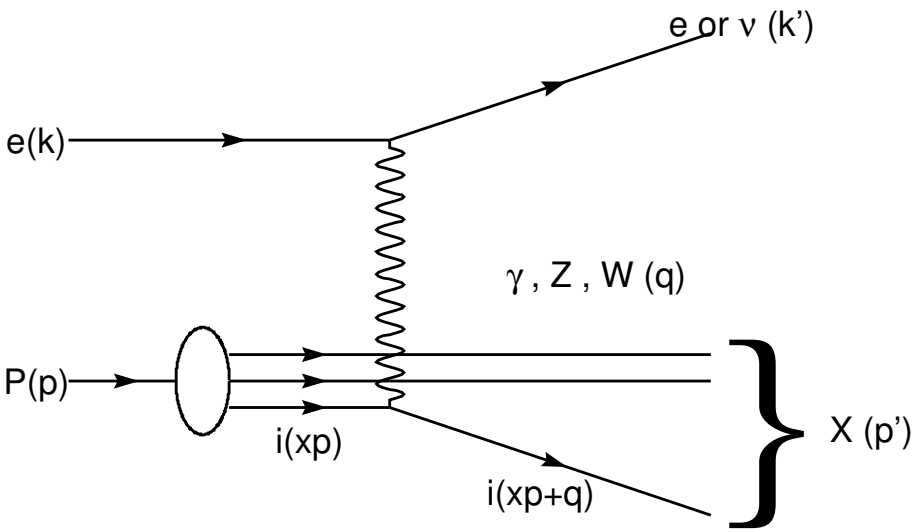

Figure 1.1 - Kinematics of ep scattering - the scattering follows through the exchange of a gauge boson (γ^*, Z^0 or $W^{\pm}$). The lowest-order Feynman diagram for DIS is shown. The four-momenta of the particles are given in brackets.

The four momenta for the incoming positron (electron) and proton in the laboratory frame, are given by :

$$\begin{aligned} k &= (E_e, 0, 0, -E_e) \\ p &= (E_p, 0, 0, E_p) \end{aligned}$$

where $E_e = 27.5$ GeV and $E_p = 820$ GeV are the energies of the electron and proton, respectively. The coordinate system is defined such that the incoming protons

move in the positive z-direction. Some important (Lorentz invariant) variables for the description of the kinematics of the ep scattering are :

- the center-of-mass energy squared of the ep system :

$$s = (p + k)^2 \simeq 4E_e E_p \ , \tag{1.1}$$

  where the approximation of neglecting the rest masses of the particles has been used.

- the virtuality (negative of the invariant mass squared) of the exchanged boson (γ^*, Z^0 or $W^{\pm}$) :

$$Q^2 = -q^2 = -(k - k')^2 \tag{1.2}$$

  The upper limit of Q^2 is s : $Q^2 \leq s$.

- The Bjorken variable x is in the QPM the fraction of the protons momentum carried by the struck quark :

$$x = \frac{Q^2}{2p \cdot q} \tag{1.3}$$

- the inelasticity y is the relative energy transfer from the positron to the proton in the protons rest frame :

$$y = \frac{p \cdot q}{p \cdot k} \tag{1.4}$$

- the center of mass energy squared of the photon-proton system :

$$W^2 = (q + p)^2 \simeq sy - Q^2 \tag{1.5}$$

- the (absolute) energy transfer from the positron to the proton in the protons rest frame :

$$\nu = \frac{p \cdot q}{M} \simeq \frac{Q^2}{2Mx} \tag{1.6}$$

  where M is the proton mass.

The variables Q^2, x, and y are not independent. They are related through the following formula :

$$Q^2 = s \cdot x \cdot y \tag{1.7}$$

1.2.2 Reconstruction of Kinematics

A precise reconstruction of the kinematics (x, Q^2) is vital for the description of DIS events. In DIS the reconstruction is based on measurements of the final state of the event with the detector.

1.2.2.1 The Jacquet - Blondel Method

The kinematics of CC DIS events are determined from the hadrons since the neutrino in the final state escapes without detection. Jacquet and Blondel proposed the following reconstruction method of the kinematics [Ja79]

$$\begin{aligned} y_{JB} &= \frac{E - P_z}{2E_e}\,, \\ Q^2_{JB} &= \frac{\not{p}_t^{\,2}}{1 - y_{JB}}\,, \\ x_{JB} &= \frac{\not{p}_t^{\,2}}{s \cdot y_{JB}(1 - y_{JB})} = \frac{Q^2_{JB}}{s \cdot y_{JB}}\,, \end{aligned} \tag{1.8}$$

where the total four-momentum of the event is given as $P = (E, P_x, P_y, P_z)$.

The $\not{p}_t$ is the absolute value of the missing transverse momentum $\overrightarrow{\not{p}_t}$:

$$\begin{aligned} \overrightarrow{\not{p}_t} &\equiv (-P_x, -P_y) \\ \not{p}_t &\equiv |\vec{\not{p}_t}| = \sqrt{P_x^2 + P_y^2} \end{aligned} \tag{1.9}$$

The total transverse energy of the event, E_t, is defined as

$$E_t \equiv \sum_i \sqrt{(P_x^i)^2 + (P_y^i)^2}\,, \tag{1.10}$$

where i runs over all the final-state hadrons. An advantage of this method is that the particles which escape without detection through the forward beam pipe, contribute little to $E - P_z$ and $\not{p}_t$, and hence to the reconstructed kinematic variables.

The angle (γ_h) and energy (E_q) of the hadronic system are defined as

$$\cos\gamma_h \equiv \frac{\not{p}_t^{\,2} - (E - p_z)^2}{\not{p}_t^{\,2} + (E - p_z)^2}\,, \tag{1.11}$$

$$E_q \equiv \frac{\not{p}_t}{\sin\gamma_h}\,, \tag{1.12}$$

respectively. In the naive Quark Parton Model (see section 1.3), γ_h and E_q are equivalent to the scattering angle and energy of the struck quark, respectively.

1.2.3 Cross Sections and Proton Structure Functions

In DIS ep experiments the exchanged high Q^2 virtual gauge bosons are used to probe the proton structure. The momentum transfer (squared) can be related to the wavelength of the virtual boson through Heisenberg's uncertainty principle :

$$\lambda \simeq \frac{\hbar}{\sqrt{Q^2}} \tag{1.13}$$

The wavelenth of the virtual boson is inversely proportional to $\sqrt{Q^2}$, implying that with increasing Q^2 the virtual boson probes smaller distances.

The *Deep Inelastic Scattering* regime is that where Q^2 is much larger than the mass squared of the proton. In this regime, the proton can be viewed as a group of quasi-free constituents one of which interacts with the boson while the rest (proton remnant) moves unperturbed. At a given center-of-mass energy $\sqrt{s}$ the kinematics of inclusive DIS scattering is completely described by two Lorentz-invariant quantites, e.g. x and Q^2.

In the single boson-exchange approximation the cross section for deep inelastic ep scattering can be factorised into a leptonic tensor $L_{\mu\nu}$, associated to the leptonic vertex, and a hadronic tensor $W^{\mu\nu}$, which describes the structure of the hadron :

$$d\sigma \sim L_{\mu\nu} W^{\mu\nu} \tag{1.14}$$

The leptonic tensor, which is symmetric in μ and ν, can be calculated exactly using the Electroweak theory (EW). For the charged-current (CC) DIS process in electron-proton collisions, $L_{\mu\nu}$ can be written as

$$\begin{aligned}
L_{\mu\nu}(e^- p \to \nu X) &\equiv \left[\overline{\nu_e}(k')\,\gamma_\mu\left(\frac{1-\gamma_5}{2}\right)e(k)\right]\left[\overline{\nu_e}(k')\,\gamma_\nu\left(\frac{1-\gamma_5}{2}\right)e(k)\right]^* \\
L_{\mu\nu}(e^+ p \to \overline{\nu} X) &\equiv \left[\overline{e}(k)\,\gamma_\mu\left(\frac{1-\gamma_5}{2}\right)\nu_e(k')\right]\left[\overline{e}(k)\,\gamma_\nu\left(\frac{1-\gamma_5}{2}\right)\nu_e(k')\right]^* \\
L_{\mu\nu} &= 2\left[k_\mu k'_\nu + k'_\mu k_\nu - g_{\mu\nu}\, k\cdot k' \pm i\varepsilon_{\mu\nu\alpha\beta}k^\alpha k'^\beta\right] ,
\end{aligned} \tag{1.15}$$

where the upper and lower signs are for an electron and positron beam, respectively, and the incoming-lepton mass has been neglected.

The structure of the proton and, hence, the details of the interaction at the hadronic vertex are parametrised in the hadronic tensor $W^{\mu\nu}$. The most general form of the tensor $W^{\mu\nu}$ which can be constructed with Lorentz invariant terms using the metric tensor $g^{\mu\nu}$ and the independent variables p and q is

$$W_{\mu\nu} = -W_1 g^{\mu\nu} + \frac{W_2}{M^2}p^\mu p^\nu + i\varepsilon^{\mu\nu\rho\sigma}p_\rho q_\sigma W_3 + \frac{W_4}{M^2}q^\mu q^\nu + \frac{W_5}{M^2}(p^\mu q^\nu + q^\mu p^\nu) \tag{1.16}$$

The conservation of the four-vector current yields

$$W_5 = -\frac{p\cdot q}{q^2}W_2 \qquad \text{and} \qquad W_4 = \left(\frac{p\cdot q}{q^2}\right)^2 W_2 + \frac{M^2}{q^2}W_1 . \tag{1.17}$$

The three remaining functions W_1, W_2 and W_3 depend on two independent Lorentz-invariant scalar variables, traditionally chosen to be ν and Q^2.

Nowadays a slightly different notation is used :

$$\begin{aligned}
F_1(x,Q^2) &= M\cdot W_1(\nu,Q^2) \\
F_2(x,Q^2) &= \nu\cdot W_2(\nu,Q^2) \\
F_3(x,Q^2) &= \nu\cdot W_3(\nu,Q^2)
\end{aligned} \tag{1.18}$$

The functions F_i are called *proton structure functions* and can be interpreted in terms of the parton density functions in the proton.

The Born cross section for *Charged Current* DIS, $ep \to \nu X$, can be written in terms of the structure functions of the proton F_i as follows [Ha84] :

$$\begin{aligned}\frac{d^2\,\sigma(e^{\pm}p)}{dx\;dQ^2} &= \frac{G_F^2}{4\pi x}\left(\frac{M_W^2}{M_W^2+Q^2}\right)\left[\,y^2 x\,F_1^{CC} + (1-y)\,F_2^{CC} \mp \left(y-\frac{y^2}{2}\right) x\,F_3^{CC}\,\right] \\ &= \frac{G_F^2}{4\pi x}\left(\frac{M_W^2}{M_W^2+Q^2}\right)\left[\,Y_+\cdot F_2^{CC} - y^2\cdot F_L^{CC} \mp Y_-\cdot x\,F_3^{CC}\,\right], \qquad (1.19)\end{aligned}$$

where M_W is the mass of the W boson and G_F is the Fermi coupling constant.
The kinematic factor $Y_\pm$ is defined as $Y_\pm = 1 \pm (1-y)^2$ and the longitudinal structure function F_L is given by

$$F_L = F_2 - 2xF_1\,. \qquad (1.20)$$

$F_3(x, Q^2)$ describes the parity violation contribution due to the weak interaction and is only relevant in the high Q^2 region ($Q^2 \gtrsim M_W^2$).

Similarly, the cross section for the *Neutral Current* DIS, $ep \to eX$ can be written as:

$$\frac{d^2\,\sigma(e^{\pm}p)}{dx\;dQ^2} = \left(\frac{2\pi\alpha^2}{xQ^4}\right)\left[\,Y_+\cdot F_2^{NC} - y^2\cdot F_L^{NC} \mp Y_-\cdot xF_3^{NC}\,\right] \qquad (1.21)$$

The parity violating contribution arises from Z^0 exchange and is important when $Q^2 \gtrsim M_Z^2$.

Within the single-photon approximation, the ep cross section can be written as a product of the photon flux with the (virtual) photon-proton cross section, $\sigma_{tot}^{\gamma^* p}$, provided the photon lifetime is longer than its interaction time with the proton. Virtual photons can be transversely or longitudinally polarised. The cross section can therefore be written as a sum of two parts - the longitudinal and the transverse one :

$$\sigma_{tot} = \sigma_L + \sigma_T \qquad (1.22)$$

The structure functions F_i can be related to these transverse and longitudinal cross sections as follows :

$$F_1 = \frac{Q^2}{8x\pi^2\alpha}\cdot\sigma_T\,;\;\; F_2 = \frac{Q^2}{4\pi^2\alpha}\cdot(\sigma_T+\sigma_L)\,;\;\; F_L = \frac{Q^2}{4\pi^2\alpha}\cdot\sigma_L \qquad (1.23)$$

The structure functions F_i are defined with respect to the Born cross section given by equation 1.21.

1.3 The Quark Parton Model

Two models were developed to describe the proton structure and that of other hadrons, the *Parton Model* from Feynman [Fe69] and the *Quark Model* by Gell-Mann and Zweig [Ge64]. In the parton model the proton is considered to consist of

(quasi) free point-like objects, called partons. Each parton i carries a fraction of the total momentum of the proton : $p_i = \xi_i \cdot p$, where p is the total momentum of the proton, p_i is momentum of parton i, and $0 \leq \xi_i \leq 1$. Therefore, the ep interaction is viewed as an incoherent sum of scatterings of the electron with the quasi-free partons in the proton.

Since in the Parton Model the partons are pointlike, an increase in the momentum transfer Q^2 will not make any new detail visible. As a consequence the structure functions are expected to be independent of Q^2. This effect is called *scale invariance*, or shortly *scaling*, which was predicted (1968) by Bjorken. In the high energy limit $Q^2 \to \infty$ but $x = Q^2/2pq$ finite, the structure functions depend only on the dimensionless scaling variable x :

$$\begin{aligned} F_1(x, Q^2) &\longrightarrow F_1(x) \\ F_2(x, Q^2) &\longrightarrow F_2(x) \end{aligned} \tag{1.24}$$

In the frame in which the proton carries infinite momentum, all the transverse momenta are negligible. In this frame the scaling variable x can be interpreted as the fractional longitudinal momentum ξ carried by the struck parton. After scattering with the positron, the momentum of the struck parton is given by $q' = \xi \cdot p + q$. Neglecting the parton and proton masses it follows that

$$0 \simeq m^2 = (\xi p + q)^2 = \xi^2 p^2 + q^2 + 2\xi qp = \xi^2 p^2 - Q^2 + 2\xi qp \Rightarrow$$

$$\xi = \frac{Q^2}{2pq} = x \tag{1.25}$$

Bjoerken and Paschos suggested (1969) that the fermions which made up the proton according to the two models (partons and quarks) were one and the same thing. Thus the model is called the *Quark Parton Model*. The scaling behaviour was confirmed by the SLAC measurements [Bl69].

In the proton infinite momentum frame, the rate at which partons interact with one another is slowed down, due to Lorentz contraction and relativistic time dilatation. During the time the virtual exchanged boson interacts with the quark, the quark itself is essentially a free particle, not interacting with the other quarks in the proton. In other words, the parton distributions during the ep collision are effectively "frozen", so that only one parton takes part in the interaction. The probability for an additional parton to take part in the interaction is suppressed as $1/(\pi r_p^2 Q^2)$, where r_p is the radius of the proton. Therefore the inelastic ep amplitude of the cross section is then given as the incoherent sum of amplitudes of elastic electron-parton scattering :

$$\frac{d^2\,\sigma}{dx\;dQ^2} = \sum_i e_i^2\; f_i(x, Q^2) \left(\frac{d^2\,\sigma_i}{dx\;dQ^2} \right) \tag{1.26}$$

where e_i is the charge of parton i and $f_i(x, Q^2)$ is the probability of finding a parton i with momentum fraction between x and $x + dx$ in the proton. In the QPM the structure functions F_1 and F_2 are related to the parton distributions functions of the proton. The structure function F_2 is the charge square weighted sum of the first momenta in x of the parton distribution functions :

$$F_2(x) = \sum_i e_i^2 \; x \; f_i(x) \; . \tag{1.27}$$

The charges e_i are given in units of the proton charge e. The QPM relates also the structure functions F_1 and F_2 to one another :

$$F_1(x) = \frac{1}{2x} \; F_2(x) \tag{1.28}$$

The above relation is known as the Callan-Gross relation [Ca69]. It implies that the structure function F_L is zero. This can also be proved using general considerations. By applying helicity conservation [Ha84], it follows that the quarks in the QPM can only couple to transversely polarised photons. Therefore, $\sigma_L = 0 \Rightarrow F_L = 0$.

The QPM was very succesful in explaining many results obtained in ep experiments. This model is though not perfect and some problems became apparent. One of them is the prediction that all the parton momentum is carried by quarks. The experimental data proved this prediction to be wrong. In fact, from experimental measurements it was obtained that less than 50% of the proton's momentum is carried by the charged valence quarks :

$$\sum_i \int_0^1 dx \; x f_i(x) \simeq 0.5 \; . \tag{1.29}$$

That is, half of the momentum of the proton is carried by neutral particles. In addition, the fact that no free quarks can be observed experimentally could not be explained by the QPM. Both these problems were solved by Quantum Chromodynamics (QCD). In the limit $Q^2 \to \infty$, QCD reproduces the QPM. In the QCD improved parton model, the proton no longer consists merely of quasifree quarks, but also of a sea of gluons and virtual quark-antiquark pairs.

1.4 QCD

Quantum Chromodynamics (QCD) is the gauge theory of the strong interactions. The interactions of quarks and gluons are described in QCD, a non-Abelian gauge theory based on the SU(3) colour symmetry group. The quarks can have one of three colours. They interact by the exchange of gluons, which are electrically neutral but form a colour charge octet. Gluons were experimentally observed through three-jet events at the PETRA collider at DESY in 1979.

A plausible property of QCD is *confinement*, which keeps quarks bounded into colourless hadrons. This prevents the observation of free quarks. The colour degree of freedom and confinement explain why observed hadrons are made either of $q\bar{q}$ or of triple-quark states. These combinations ensure that the hadrons are colourless and have integer electrical charges. In the presence of QCD, the naive QPM picture of hadrons has to be altered to take into account the radiation and absorption of gluons by quarks as well as the radiation of $q\bar{q}$ pairs by gluons.

QCD has properties which make it much more difficult to work with theoretically than electroweak theory. The strong coupling constant α_s becomes large at large distances. This makes the use of perturbation theory very difficult. The effective strong coupling constant α_s depends on the scale at which the QCD process occurs, on the number of active quark flavours, and on a free scale parameter :

$$\alpha_s(Q^2) = \frac{4\pi}{(11 - 2n_f/3)\ln(\frac{Q^2}{\Lambda^2})} , \tag{1.30}$$

where Q^2 is the scale at which α_s is probed. Λ is a the free scale parameter. Measurements show that $\Lambda^{(5)}_{\overline{MS}} = 208^{+25}_{-23}$ MeV (Particle Data Group : [Pa00]). The known number of flavours is 6, so $(11 - 2n_f/3)$ is positive. At large Q^2 α_s is small and the quarks are quasi-free. In this region of asymptotic freedom perturbative QCD (pQCD) is applicable and predictions on the properties of strong interactions can be made.

1.4.1 Factorization

Hadron-hadron and lepton-hadron interactions are described in QCD as an incoherent sum of the interaction of the constituent partons (quarks, gluons) from one hadron with those of the other hadron or with the lepton[5]. The distributions of partons in hadrons cannot be calculated,at present, from first principles.

A separation of the short-ranged (hard processes) and long-ranged (soft-processes) physics is introduced. This separation is called *factorization*. The QCD factorization theorem [Co85] states that for hard scattering reactions the cross section can be decomposed into the flux of incoming particles and the cross section for the hard process (see figure 1.2) :

$$\sigma = f_{i/1}(x_1) \otimes \sigma_{i,j}(Q^2) \otimes f_{j/2}(x_2) , \tag{1.31}$$

where $f_{i/1}(x_1)$ and $f_{j/2}(x_2)$ are the fluxes of the incoming particles. $\sigma_{i,j}(Q^2)$ is the cross section (matrix element) for the hard scattering of the two partons i and j.

The flux of incoming particles depends on the parton distribution functions, i.e. on the probability to find a particular parton having a momentum fraction in the range $(x, x + dx)$. So $f_{i/1}(x_1) \cdot dx_1$ is the probability to find the parton i in the first hadron carrying a fraction x_1 of its momentum.

Generally, parton distribution functions give the probability to find partons (quarks and gluons) in a hadron as a function of the fraction x of the hadron's momentum they carry.

In order to perform the factorization, a hard scale μ_F - the factorization scale - has to be introduced. The long-ranged (non perturbative) processes are absorbed into the parton distribution functions (PDFs). These parton distribution functions are

[5]The total amplitude of the interaction is an incoherent sum of the amplitudes of the interactions of the constituents.

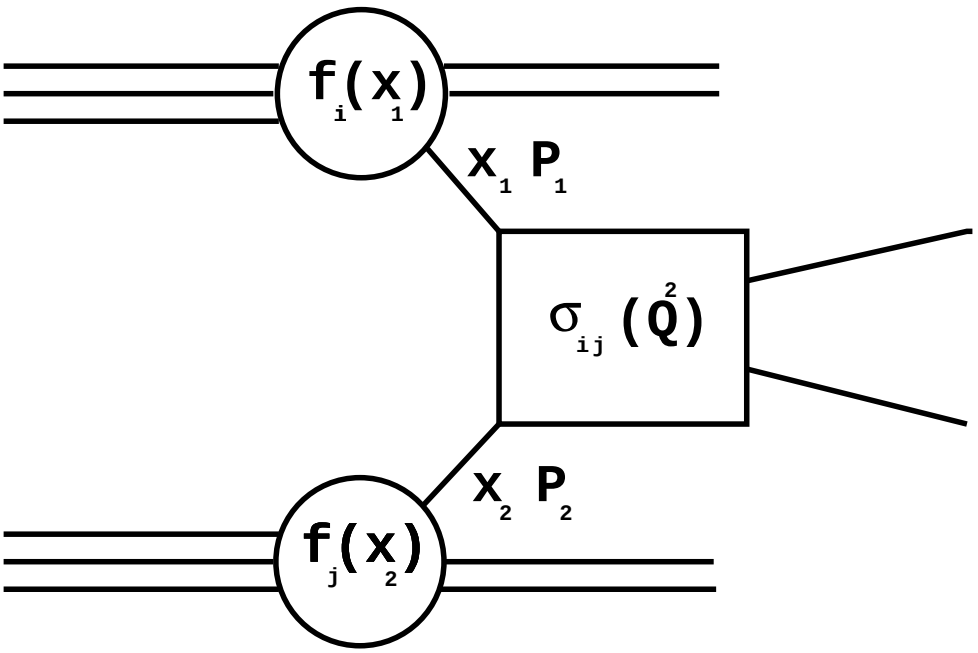

Figure 1.2 - Factorization: separation of the short-ranged and long-ranged physics. The parton distributions in the hadrons cannot be perturbatively calculated (long-ranged physics). The hard cross section $\sigma_{ij}(Q^2)$ is perturbatively calculable (short-ranged physics).

assumed to be universal, i.e. process independent. At present it is not possible to calculate them in QCD and their values are fixed from experimental results.

On the other hand, the cross section for the hard process is a short-ranged process and can be perturbatively calculated.

In addition, pQCD introduces another scale μ_R - the renormalization scale. By introducing the renormalization scale the divergences coming from the calculation of virtual corrections (which yield divergent integrals) are absorbed into the definition of the parameters of the theory. Several renormalization schemes are used, the most important being the *minimal subtraction scheme* - $\overline{MS}$ and the *deep inelastic scattering scheme* - DIS.

1.4.2 QCD evolution equations

The Q^2 dependence of the parton distribution functions can be calculated within pQCD. The main origin of this dependence is that a quark seen at a certain scale Q_0^2 as carrying a certain fractional momentum of the hadron x_0 can be resolved into more quarks and gluons if it is probed at a higher scale Q^2. The resolved quarks and gluons carry a smaller fractional momentum of the hadron ($x < x_0$). The change of the structure function F_2 with increasing scale is schematically shown in figure 1.3. Thus, when all QCD effects are included, the structure function F_2 is expected to rise at low x. This is because the low x region is populated by gluons and sea quarks and the quark density is large. The resulting logarithmic dependence of F_2 on Q^2 at

fixed x is known as *scaling violation*.

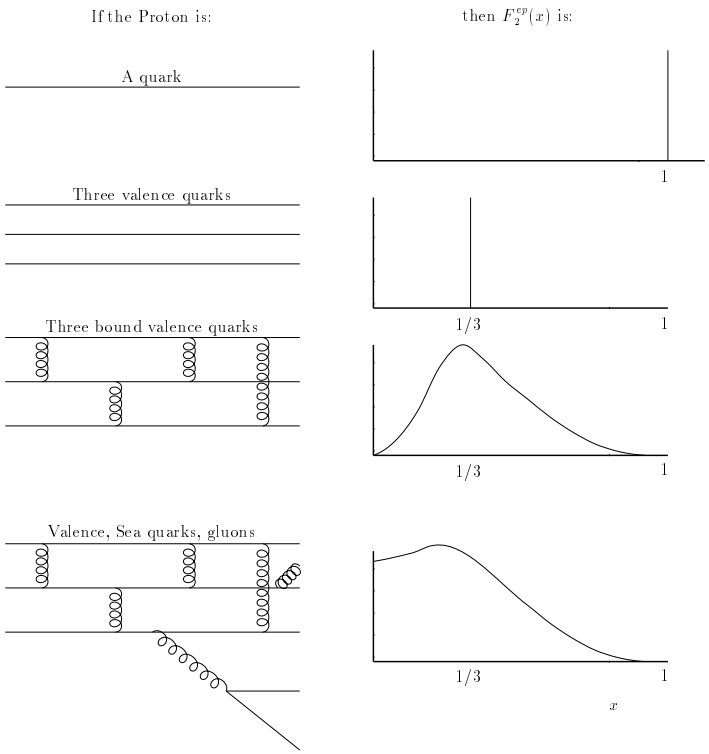

Figure 1.3 - The proton structure function F_2 pictured assuming different compositions for the proton. The two top pictures show the case of QPM. The two bottom pictures show the modifications induced by QCD effects.

At HERA, the structure function F_2 has been measured in a very wide range of Q^2 and x and the scaling violation at low x has been demonstrated. This is shown in figure 1.4.

The DGLAP (Dokshitzer - Gribov - Altarelli - Parisi [Al77]) equations are a set of $(2n_f + 1)$ coupled integro-differential equations. They can be used to determine the quark and gluon distribution functions for any value of Q^2 provided they are know at a particular value Q_0^2 within the range of applicability of perturbative QCD. These equations are derived by requiring that the structure functions F_1 and F_2 be independent of the choice of the factorization scale μ_F, that is :

$$\mu_F^2 \left(\frac{dF_i(x, Q^2)}{d\mu_F^2} \right) = 0 \qquad ; \qquad i = 1, 2 \tag{1.32}$$

In a first step, the DGLAP equations were derived in the *leading log approximation* - LLA. The terms which give the dominant contributions at large x and Q^2 were summed to all orders. All other terms were neglected.

In a compact form the DGLAP equations can then be written as :

$$\frac{\partial}{\partial \ln Q^2} \begin{pmatrix} q \\ g \end{pmatrix} = \frac{\alpha_s(Q^2)}{2\pi} \begin{bmatrix} P_{qq} & P_{qg} \\ P_{gq} & P_{gg} \end{bmatrix} \otimes \begin{pmatrix} q \\ g \end{pmatrix} \tag{1.33}$$

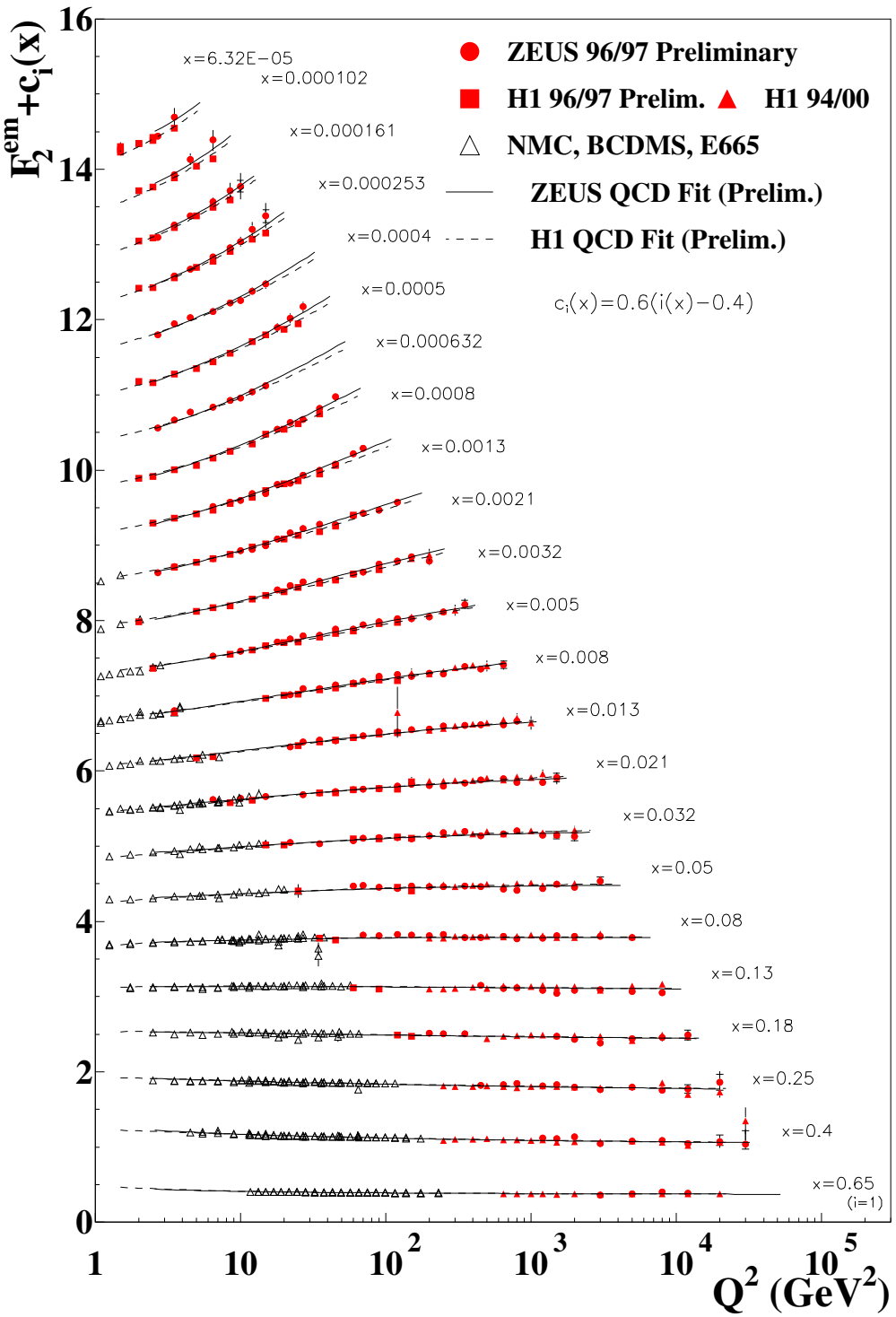

Figure 1.4 - Measurement of the structure function F_2 as a function of Q^2 for different values of x. The F_2 measurements different values of x have been scaled by constant factors for display purposes. The evolution of the structure functions through the DGLAP equations are also shown.

where $q(x, Q^2)$ ($g(x, Q^2)$) are the quark (gluon) distributions, and $P_{ij}(x)$ are the splitting functions. The latter describe the probability to find a parton of type i with given fractional momentum originating from the parton of type j, where i, j can be a quark or a gluon.

Given a specific factorization and renormalization schemes, the splitting functions are obtained in pQCD as expansion series in α_s :

$$\frac{\alpha_s}{2\pi}P_{ij}(x, Q^2) = \frac{\alpha_s}{2\pi}P_{ij}^{(1)}(x) + (\frac{\alpha_s}{2\pi})^2 P_{ij}^{(2)}(x) + ... \tag{1.34}$$

The truncation after the first two terms in the series defines the next-to-leading order (NLO) DGLAP evolution equations.

The DGLAP equations are valid as long as the impact of the neglected terms is small. At very low x this is not true anymore. In this region another approach is used and the calculations lead to the BFKL (Balitsky - Fadin - Kuraev - Lipatov [Ku76]) equations. DGLAP deals with the Q^2 evolution and is inadequate at very low x. BFKL deals with the $\frac{1}{x}$ evolution and is inadequate at large Q^2.

The inclusive measurement of F_2 at HERA has shown that the evolution of structure functions through the DGLAP equations is in good agreement with the experimental results (figure 1.4). Until now no experimental evidence for BFKL effects has been observed.

Attempts have been made to achieve a unified description embodying both DGLAP- and BFKL-type of evolution. Evolution equations which allow an evolution in Q^2 as well as in x are included in the CCFM (Ciafaloni - Catani - Fiorani - Marchesini [Ci88]) evolution equations.

1.5 Photoproduction

The kinematical regime where Q^2 is very small ($Q^2 \simeq 0$) is called *Photoproduction*. In photoproduction events the scattered electron has a very small angle with respect to the incoming one. Therefore, most of the time it goes undetected through the rear beam pipe[6]. The exchanged photon is quasi-real.

In photoproduction the hard scale of the interaction cannot be identified with Q^2 but the transverse energy of the (hard) outgoing partons. The situation now is reversed and the proton is not anymore being probed by the photon. In fact, both the proton and photon are probed by the exchanged virtual partons.

[6] At HERA, in some cases the very-low-angle scattered electron can be detected in the luminosity monitor.

Chapter 2

The HERA collider and the ZEUS detector

2.1 The Hadron Electron Ring Accelerator

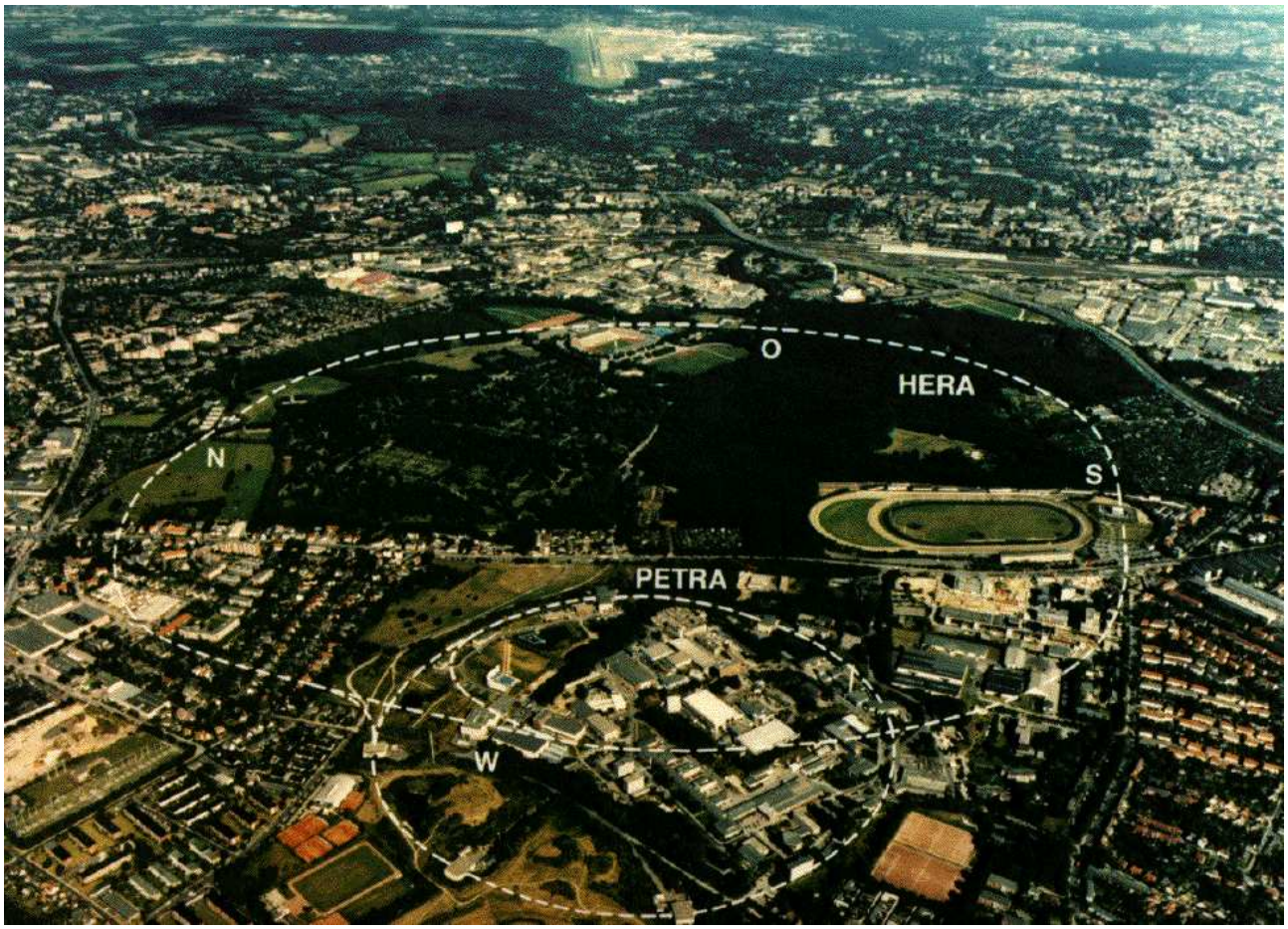

Figure 2.1 - View of DESY.

The HERA (Hadron Elektron Ring Anlage) collider is located at DESY in Hamburg, Germany. It offers unique opportunities to explore the structure of the proton as it is the first ep collider in the world. Figure 2.1 shows an aerial view of DESY and the

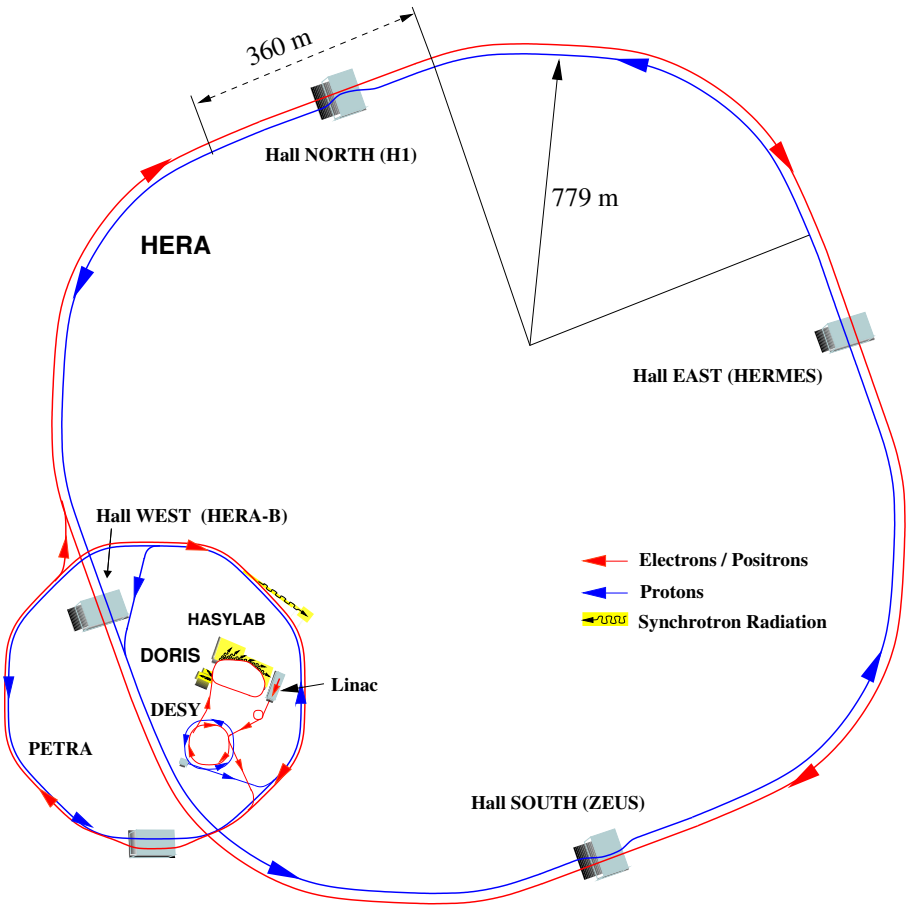

Figure 2.2 - The HERA accelerator complex. Four experiments are located in the experimental halls : South (ZEUS), West (HERA-B), North (H1), and East (HERMES).

surrounding area including the location of the two largest accelerators HERA and PETRA.

HERA was approved in 1984 and first collisions were observed in 1991. Operations for physics started in 1992. HERA consists of one storage ring for protons and one for electrons.The design energy is 30 GeV for electrons and 820 GeV for protons. Each storage ring consists of four 90° arcs connected by 360 m long straight sections and is located (10–25) m below ground. Superconducting magnets are used for the proton storage ring. Four experimental halls (North, South, East, West) are situated in the middle of the straight sections. The two collider experiments, H1 and ZEUS, are located in the northern and southern experimental halls, respectively. In both interaction regions electrons and protons collide head-on at zero crossing angle. Two fixed-target experiments, HERMES and HERA-B, have been installed in the eastern and western experimental halls, respectively. They make use of only the HERA electron (HERMES) and proton (HERA-B) beams, respectively. HERMES [HE93] is investigating the spin structure of the nucleon and HERA-B [HB94] aims to study the $\mathcal{CP}$-violation in the $\mathrm{B^0\overline{B}^0}$-system. Figure 2.2 shows the layout of the HERA collider, the four experimental halls and the system of pre-accelerators used at DESY. In a first step electrons and protons are accelerated using linear accelerator. A small

HERA parameters	Design Values		Values of 1997	
	$e^{\pm}$	p	e^{+}	p
Circumference (m)	6336			
Energy (GeV)	30	820	27.6	821.2
Center-of-mass energy (GeV)	314		301	
Injection energy (GeV)	14	40	12	40
Energy loss per turn (MeV)	127	$1.4 \cdot 10^{-10}$	127	$1.4 \cdot 10^{-10}$
Current (mA)	58	160	36	78
Magnetic field (T)	0.165	4.65	0.165	4.65
Number of bunches	210	210	174+15	174+6
Bunch crossing time (ns)	96			
Horizontal beam size (mm)	0.301	0.276	0.200	0.200
Vertical beam size (mm)	0.067	0.087	0.054	0.054
Longitudinal beam size (mm)	0.8	11	0.8	11
Specific luminosity ($cm^{-2}s^{-1}mA^{-2}$)	$3.6 \cdot 10^{29}$		$5.0 \cdot 10^{29}$	
Instantaneous luminosity ($cm^{-2}s^{-1}$)	$1.6 \cdot 10^{31}$		$1.45 \cdot 10^{31}$	
Integrated luminosity per year (pb^{-1}/a)	35		36.5	

Table 2.1 - HERA parameters. In 1997 HERA operated with 174 colliding bunches, 15 positron-pilot bunches and 6 proton-pilot bunches.

storage ring PIA (Positron-Intensity-Accumulator) is used in between the linear accelerator and DESY II to accumulate electrons until sufficient intensity is reached. In a next step the particles are injected into DESY II (electrons) and DESY III (protons). After injection into PETRA and further acceleration, electrons and protons are injected into HERA. From 1995 to 1997 positrons were used instead of electrons because severe lifetime problems of the electron beam were observed. The reason is most likely the capturing of positively-charged dust which originates from ion getter pumps from the HERA electron vacuum system by the electron beam [DE94]. With the installation of new pumps in the winter shutdown 1997/1998 the problem has been significantly reduced and HERA switched back to electrons in 1998. Several HERA parameters from the 1997 runing period and the corresponding design values are given in table 2.1.

2.2 The ZEUS Detector

The ZEUS detector is a general purpose magnetic detector designed to study various aspects of electron-proton scattering. It has been in operation since 1992 [ZE93] and consists of various sub-components to measure the hadrons and leptons in the final-state and, therefore, to characterize the final-state in terms of energy, direction, and type of the produced particles.

The coordinate system of the ZEUS detector is a Cartesian right-handed coordinate system. The origin ($(X, Y, Z) = (0, 0, 0)$) is located at the nominal interaction point. The Z-axis points in the proton beam direction, the Y-axis upwards, and the X-axis horizontally towards the center of HERA. The polar (azimuthal) angle θ (ϕ) is deter-

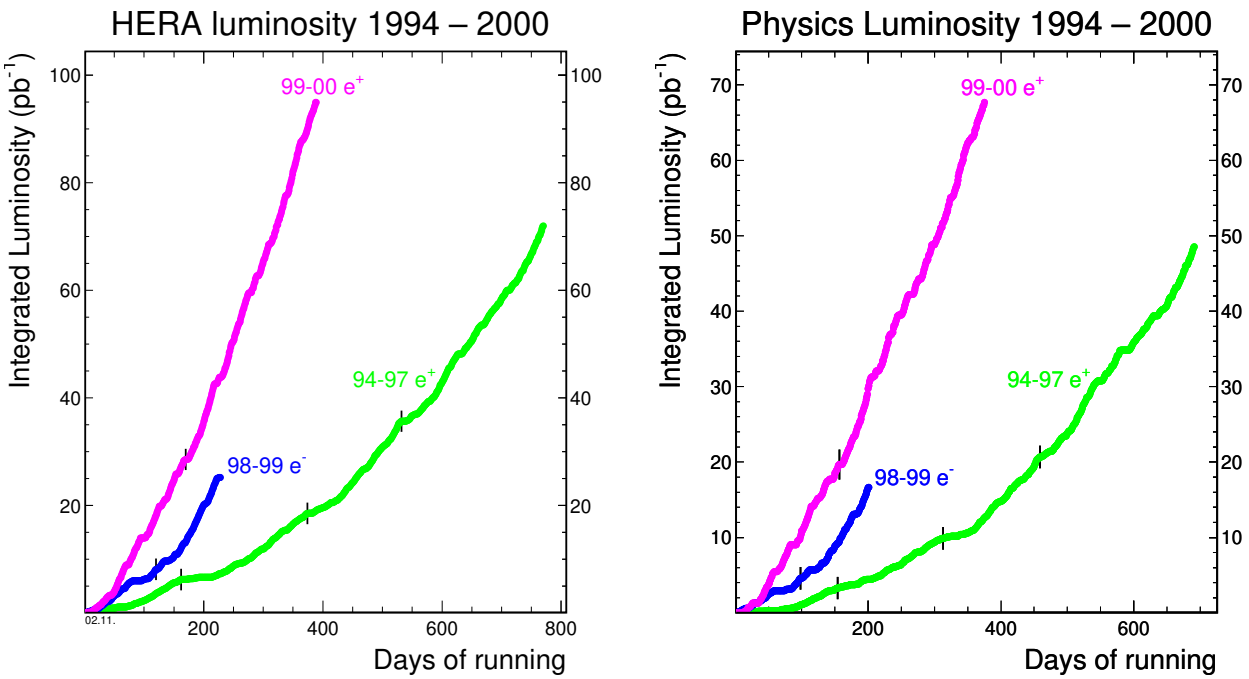

Figure 2.3 - Integrated luminosity delivered by HERA in the different running periods (left plot) and the one taken with the ZEUS detector (right plot). The latter is used for physics analysis.

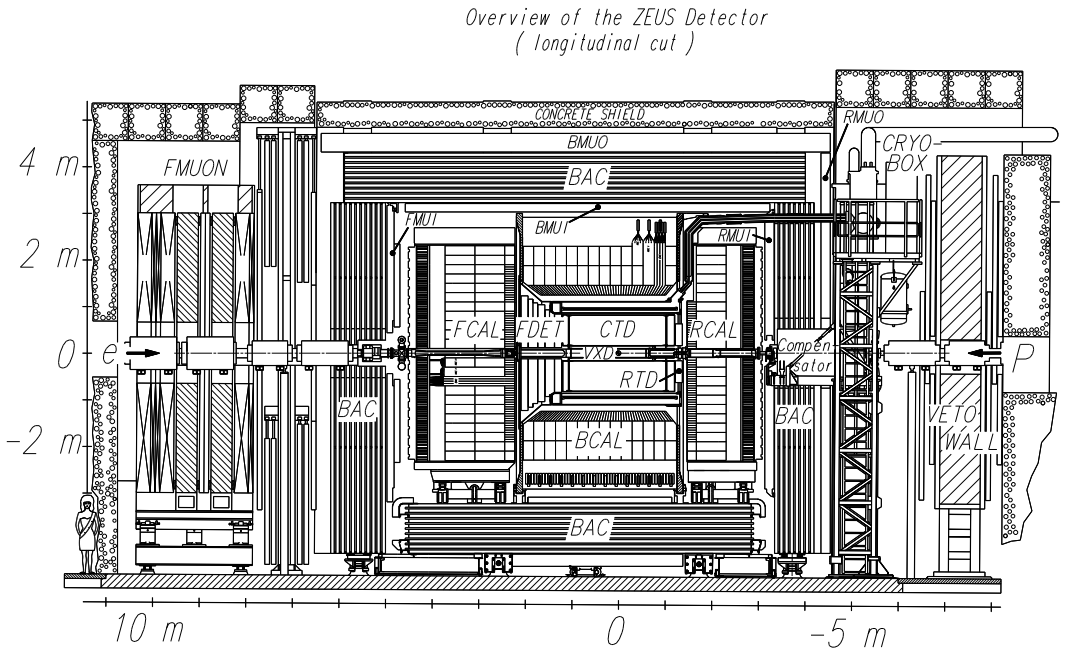

Figure 2.4 - View of the ZEUS detector along the beam direction.

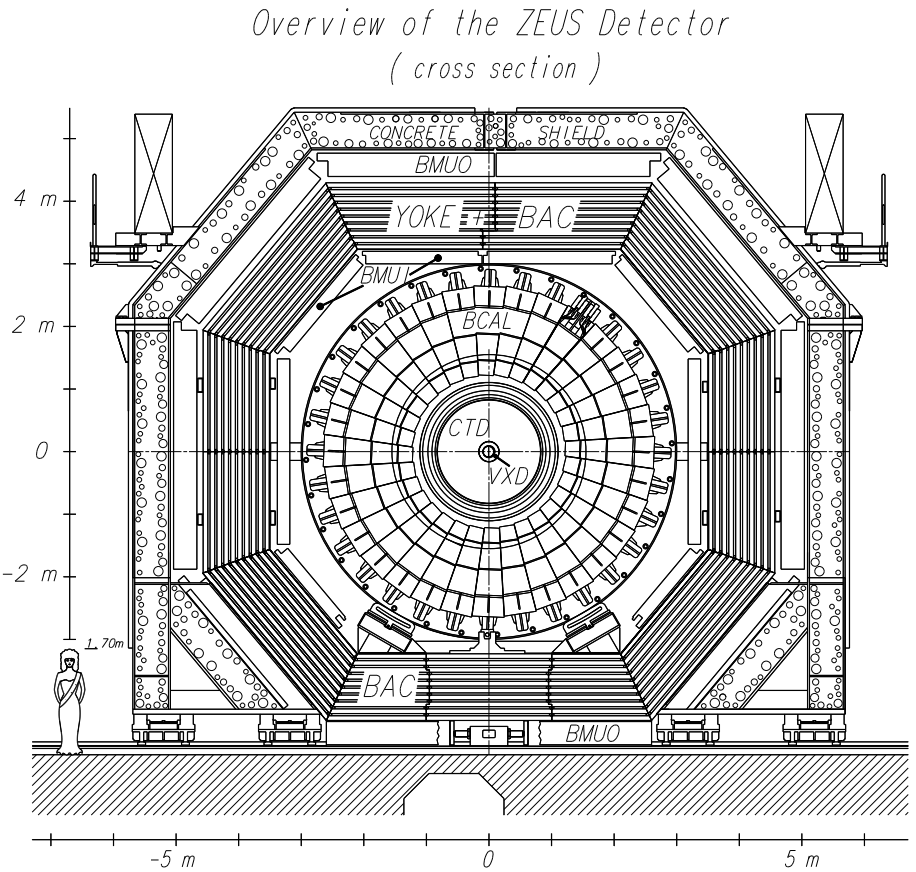

Figure 2.5 - View of the ZEUS detector perpendicular to the beam direction. See text for a description of the components.

mined relative to the positive Z-axis (X-axis). With this definition the polar angle of the incoming electron beam is $180°$ and the one of the incoming proton beam is $0°$. The +Z-direction is referred as the *forward*, and the –Z-direction as the *backward* direction.

The ZEUS detector consists of the main detector located around the nominal interaction point and several small detectors positioned along the beam line in both positive and negative Z-directions. The main detector is shown in figurea 2.4 and 2.5 along and perpendicular to the beam direction, respectively. The design is asymmetric with respect to the Z-axis because of the large forward-backward asymmetry of the final-state system. The difference in the energy of the electron beam (27.5 GeV) and proton beam (820 GeV) results in a center-of-mass system which is moving in the direction of the proton beam relative to the laboratory frame.

The inner part of the main detector consists of the tracking system enclosed by a superconducting solenoid which produces an axial magnetic field of 1.43 T. The CTD, a cylindrical drift chamber, surrounds the beam pipe at the interaction point. In order to provide additional means of track reconstruction in the forward (backward) direction, the CTD was supplemented by the FTD (RTD). The FTD consists of three sets of planar drift chambers with transition radiation detectors (TRD) in between. The RTD is one planar drift chamber with three layers. The vertex detector VXD measures the event vertex and possibly secondary vertices and improves the momentum and

angular resolution of charged particles as determined with the CTD alone. In 1994 high voltage problems and damage due to synchrotron radiation caused part of the VXD to be off and it was removed.

The high resolution uranium calorimeter (UCAL) encloses the tracking detectors. It is subdivided into the forward (FCAL), barrel (BCAL), and rear (RCAL) parts.

The UCAL in turn is surrounded by an iron yoke made of 7.3 cm thick iron plates. The yoke serves two purposes: it provides a return path for the solenoid magnetic field flux and is in addition instrumented with proportional chambers. The latter design feature makes it possible to measure energy leakage out of the UCAL. The yoke is therefore referred to as the backing calorimeter (BAC). As the yoke is magnetized to 1.6 T by copper coils it is used to deflect muons. In order to detect and measure the momentum of muons, limited streamer tubes are mounted surrounding the iron yoke in the barrel (BMUI, BMUO) and the rear (RMUI, RMUO) regions. As the particle density and the muon momentum in the forward direction is higher than in the barrel and rear directions due to the energy difference of the electron and proton beam, the muon chambers in the forward direction are designed differently. Limited streamer tubes mounted on the inside of the iron yoke (FMUI) and drift chambers and limited streamer tubes mounted outside the iron yoke (FMUO) are used for this purpose. Two iron toroids provide a toroidal magnetic field of 1.7 T. In the backward direction at $Z = -7.3$ m, a veto wall outside the detector composed of iron and scintillator strips is used to reject background events dominated by proton-beamgas reactions.

2.2.1 The Central Tracking Detector

The tracking system of the ZEUS detector consists of the forward, central and rear tracking devices, which operate under a high magnetic field of 1.43 T to achieve a high resolution for high momentum tracks. All the tracking quantities used in this analysis are provided by the Central-Tracking Detector (CTD) [Fo93]. The CTD is a cylindrical drift chamber which provides a high precision measurement of the direction and transverse momentum of charged particles and of the event vertex. The position resolution in $r-\phi$ is about $230\ \mu$m and the transverse momentum resolution is

$$\frac{\sigma(p_t)}{p_t} = 0.0058 \cdot p_t(\text{GeV}) \oplus 0.0065 \oplus \frac{0.0014}{p_t}, \qquad (2.1)$$

where the first term corresponds to the resolution of the hit positions, the second term to smearing from multiple scattering within the CTD and the last term to multiple scattering before the CTD. The position of the interaction point in X and Y is measured with a resolution of 0.1 cm and in Z with a resolution of 0.4 cm.

The CTD is filled with a mixture of argon, CO_2, and ethane. Particle identification is possible by measurements of the mean energy loss dE/dx of charged particles within the tracking detector. The CTD covers a polar angle of $15° < \theta < 164°$ and the full range of the azimuthal angle ϕ. Its active volume has a length of 205 cm, an inner radius of 18.2 cm, and an outer radius of 79.4 cm.

The CTD is designed as a multi-cell superlayer chamber and subdivided into eight

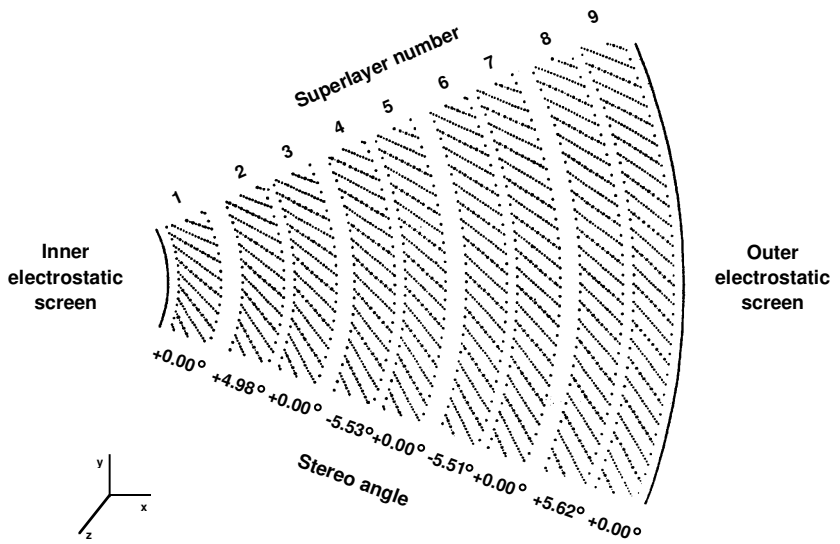

Figure 2.6 - Layout of a CTD octant. Each octant has nine superlayers with the even numbered ones declined with respect to the beam axis ('Stereo angle').

sections and nine superlayers. One octant is shown in figure 2.6. The CTD consists of 576 cells with each cell being equipped with eight sense wires. The number of cells increases from 32 in the innermost superlayer to 96 cells for the outermost superlayer. Every other superlayer has its sense wires rotated by a certain angle with respect to the beam axis. The angles for each superlayer are given in figure 2.6. With this configuration the Z position of a track can be reconstructed with an accuracy of aproximately 2 mm.

2.2.2 The Uranium-Scintillator Calorimeter (UCAL)

Calorimeters in particle physics measure the energy of particles by their absorption in a medium that becomes ionised or excited through shower processes. The ZEUS calorimeter (UCAL) has been designed as a sampling calorimeter, where absorber layers alternate with scintillator layers, which are the optical readout. The calorimeter is required to be hermetic with a nearly full solid-angle coverage and to have a good hadronic energy resolution by achieving an equal response to electromagnetic and hadronic particles.

The UCAL is divided into three parts, which cover different polar angles [De91]. All parts of the calorimeter, FCAL ($2.2^\circ < \theta < 39.9^\circ$), BCAL ($36.7^\circ < \theta < 128.1^\circ$), and RCAL ($128.1^\circ < \theta < 176.5^\circ$) are built of alternating layers of 3.3 mm thick depleted uranium and 2.6 mm thick plastic scintillator plates (SCSN38). The natural radioactivity of ^{238}U is used as a reference signal to calibrate the readout channels to a precision of $< 0.2\%$.

Uranium is an advantageous absorber for hadron calorimetry, since it provides a high yield of spallation neutrons which impart the energy to the hydrogen nuclei of the scintillator. Together with an additional contribution of photons from neutron cap-

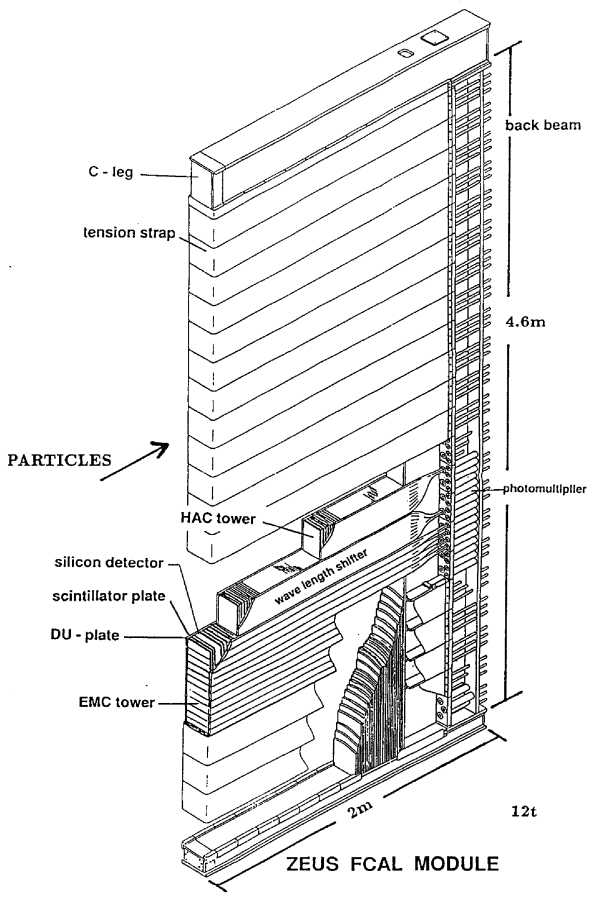

Figure 2.7 - Layout of a FCAL module The UCAL modules are subdivided into one electromagnetic (EMC) and two hadronic (HAC1,HAC2) sections, which in turn are divided into cells. A cell is read out on two opposite sides by one wavelength shifter each.

ture of the uranium, this helps compensating the signal loss of hadrons suffer from the loss of binding energy, nuclear fission fragments and from undetected decay products. Electrons and photons do not suffer such losses as they interact predominantly with the atomic electrons and not with the nuclei. The ratio between the pulse heights of electrons and hadrons, e/h, which has been achieved is

$$e/h = 1.00 \pm 0.03 \tag{2.2}$$

The three calorimeter parts are subdivided into modules. The modules are transversally separated into towers and the towers in turn longitudinally into electromagnetic (EMC) and hadronic sections (HAC). The design of an FCAL module is shown in figure 2.7. FCAL and RCAL are planar and perpendicular with respect to the beam axis (see figure 2.4), while the BCAL modules are wedge-shaped and projective in the polar angle. The calorimeter modules are further segmented into cells. The design of the three calorimeter parts takes into account the different particle densities and energies due to the asymmetric electron and proton beam energies. Each EMC section is segmented transversally into four cells (two in RCAL), while a HAC tower is not divided transversally. They are instead longitudinally subdivided into two (one

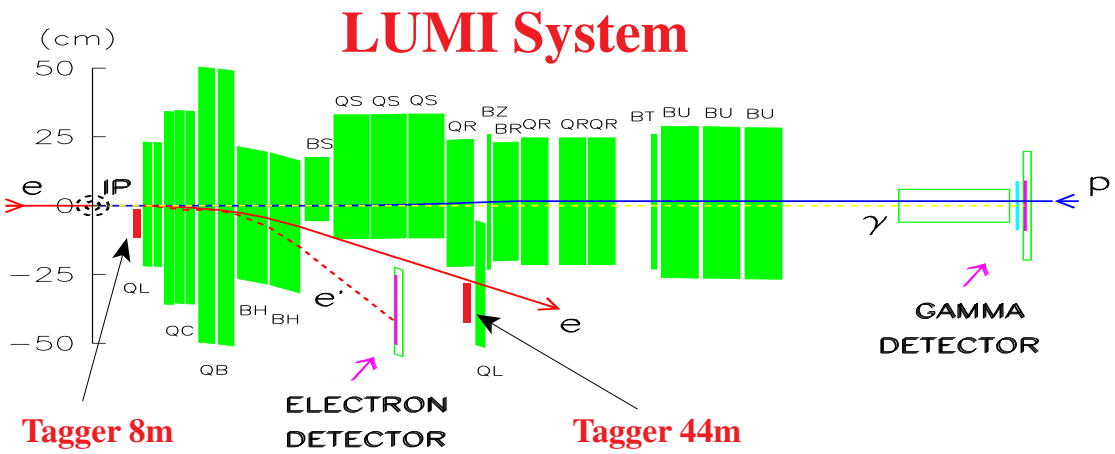

Figure 2.8 - Location of ZEUS detectors in negative Z-direction. Shown are the gamma (LUMIG) and electron detectors (LUMIE) used for the luminosity measurement.

in RCAL) hadronic cells (HAC1, HAC2). Each cell has read out on two opposite sides. This is done on each side by a wavelength shifter coupled to one photomultiplier tube. The information of both photomultiplier tubes is used to provide a limited reconstruction of the position of the measured particle and to check the uniformity of the readout.

The energy resolution for electrons and hadrons was determined in test-beam experiments to be $\sigma_E/E = 0.18/\sqrt{E}$ and $\sigma_E/E = 0.35/\sqrt{E}$ respectively, where E is mesured in GeV.

2.3 The Luminosity measurement

The luminosity, $\mathcal{L} \equiv N/\sigma$, relates the number of events N with the cross section σ. A precise determination of the luminosity is essential for any cross section measurement in a high energy physics experiment. The luminosity of ep-collisions at HERA is measured by observing the rate of hard bremsstrahlung photons from the Bethe-Heitler process $ep \rightarrow e\gamma p$ [Be34]. As the theoretical cross section is known to an accuracy of 0.5% from QED calculations, a precise measurement of the photon rate permits a precise determination of the ep-luminosity at HERA.

Figure 2.8 shows the layout of the HERA magnet system and the ZEUS luminosity detectors in the backward (–Z)-direction. In the case of ZEUS this is done by two lead/scintillator electromagnetic calorimeters at $Z = -34$ m (LUMIE) and $Z = -107$ m (LUMIG). Photons with $\theta_\gamma < 0.5$ mrad originating from the Bethe-Heitler process $ep \rightarrow e\gamma p$ are detected by the LUMIG detector [An92]. The energy resolution of the LUMIG detector was measured under test-beam conditions to be $18\%/\sqrt{E}$. It was also determined that the carbon/lead filter placed in front of the detector to shield it against synchrotron radiation degrades the resolution to $23\%/\sqrt{E}$. The impact position of incoming photons can be determined with a resolution of 0.2 cm in X and

Y, because at a depth of $7X_0$ 1 cm wide scintillator strips are installed within the LUMIG detector. The LUMIG detector is also used to determine the electron beam tilt and to measure photons from initial-state radiation.

The LUMIE calorimeter [An92] at Z $= -35$ m detects electrons in the limited energy range from 7 to 20 GeV which are produced under polar angles of less than 5 mrad with respect to the electron beam direction. These electrons are deflected by the HERA magnet system and leave the beam pipe at Z $= -27$ m through an exit window similar to the one in front of the LUMIG detector. The LUMIE detector has an energy resolution of $18\%/\sqrt{E}$ under test-beam conditions. It was initially designed to measure the electrons of the Bethe-Heitler process $ep \rightarrow e\gamma p$ at the same time as the photons of this process are measured in the LUMIG detector. It was found that this was not necessary to have a precise measurement of the luminosity.

2.4 The ZEUS trigger and data acquisition systems

The short bunch crossing time at HERA of 96 ns, equivalent to a rate of of about 10^7 crossings per second , is a technical challenge and puts stringent requirements on the ZEUS trigger and data acquisition systems. The total interaction rate, which is dominated by background from upstream interactions of the proton beam with residual gas in the beampipe, is of the order 10 - 100 kilo-events per second (10 - 100 kHz) while the rate of ep physics events in the ZEUS detector is of the order of a few Hz [Sm84, Yo92]. Other background sources are electron beam gas collisions, beam halo and cosmic events.

ZEUS employs a sophisticated three-level trigger system in order to select ep physics events efficiently while reducing the rate to a few Hz. A schematic diagram of the ZEUS trigger system is shown in figure 2.9.

The First Level trigger (FLT) is a hardware trigger, designed to reduce the input rate below 1 kHz. Each detector component has its own FLT, which stores the data in a pipeline, and makes a trigger decision within 2 μs after the bunch crossing. The decision from the local FLTs are passed to the Global First Level Trigger (GFLT), which decides whether to accept or reject the event, and returns this decision readout within 4.4 μs. The typical information available at FLT are CAL activities (total transverse energy, missing transverse momentum,...), CTD tracks (number of tracks,...), hits in the muon chambers, etc.

If the event is accepted, the data is fully digitalised and transferred to the Second Level Trigger (SLT). The trigger signals at the SLT have a better resolution than those at FLT. Moreover, some information is first available at the SLT like CAL timings, which are useful in rejecting non-ep background events. The SLT is designed to reduce the rates to the order of 50-100Hz. Each detector component has its own SLT, which passes a trigger decision to the Global Second trigger (GSLT) [Ui92].

If the event is accepted by the GSLT, all detector components send their data to the Event Builder (EVB), which combines all the data of an event into a single record of ADAMO [Fi93] database tables. This is the data structure on which the Third Level Trigger (TLT) code runs. The TLT is software based and runs part of the offline

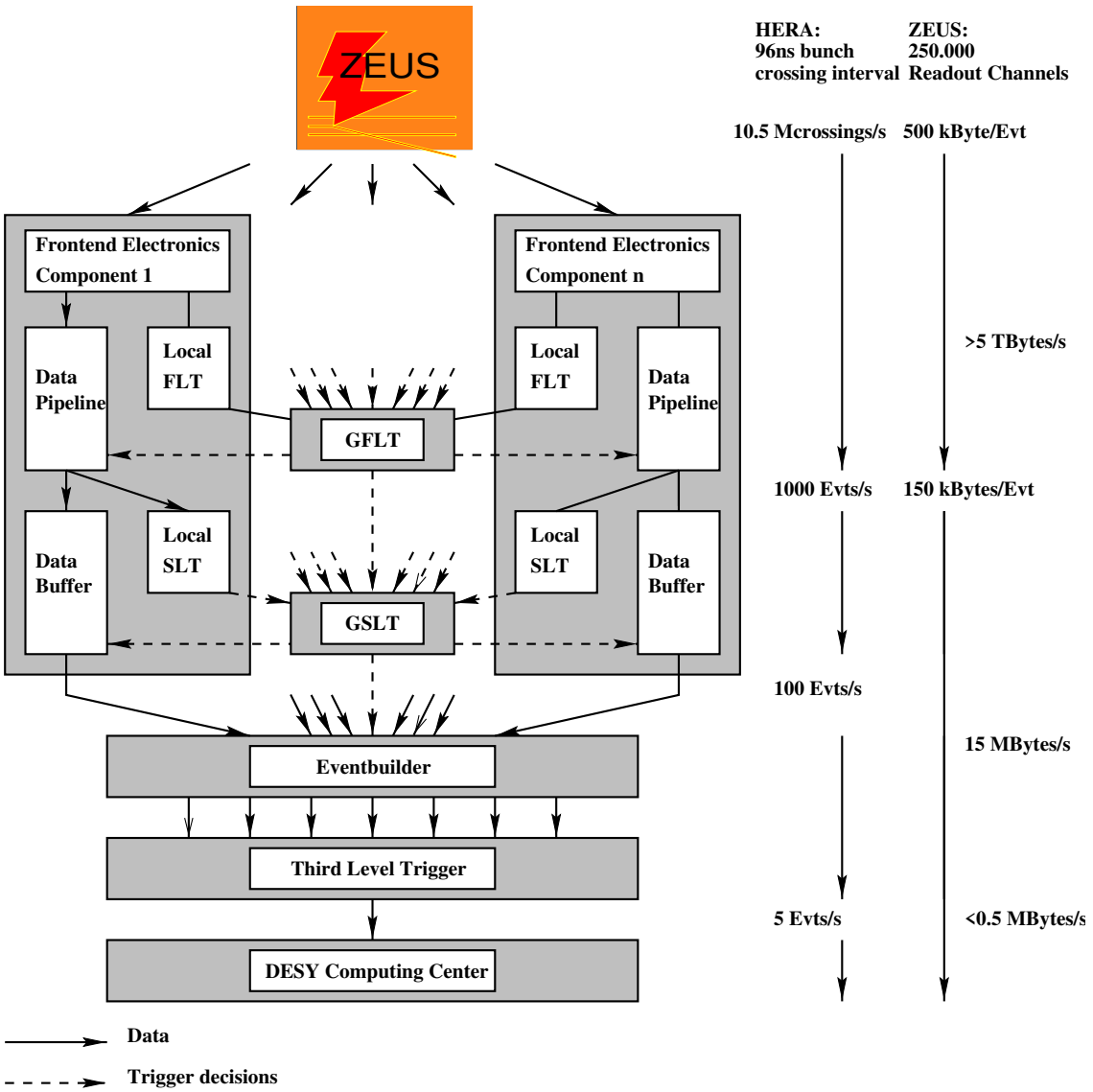

Figure 2.9 - Schematic diagram of the ZEUS trigger and data acquisition systems.

reconstruction code. It is designed to reduce the rate to a few Hz.

2.5 Event reconstruction and analysis

The scheme of the ZEUS offline and Monte Carlo (MC) simulation programs is shown in figure 2.10. Events from the real detector or simulated events are reconstructed by the program ZEPHYR. The signals of the different calorimeter components are calibrated and highly complex tasks like tracking reconstruction are performed. After reprocessing the raw data, the user has access to the raw and reconstructed quantities via the program EAZE. In the framework of EAZE, the user writes his own analysis program in either Fortran or C. It is used to reconstruct relevant quantities and perform selection cuts. Subsets of the data or MC simulated

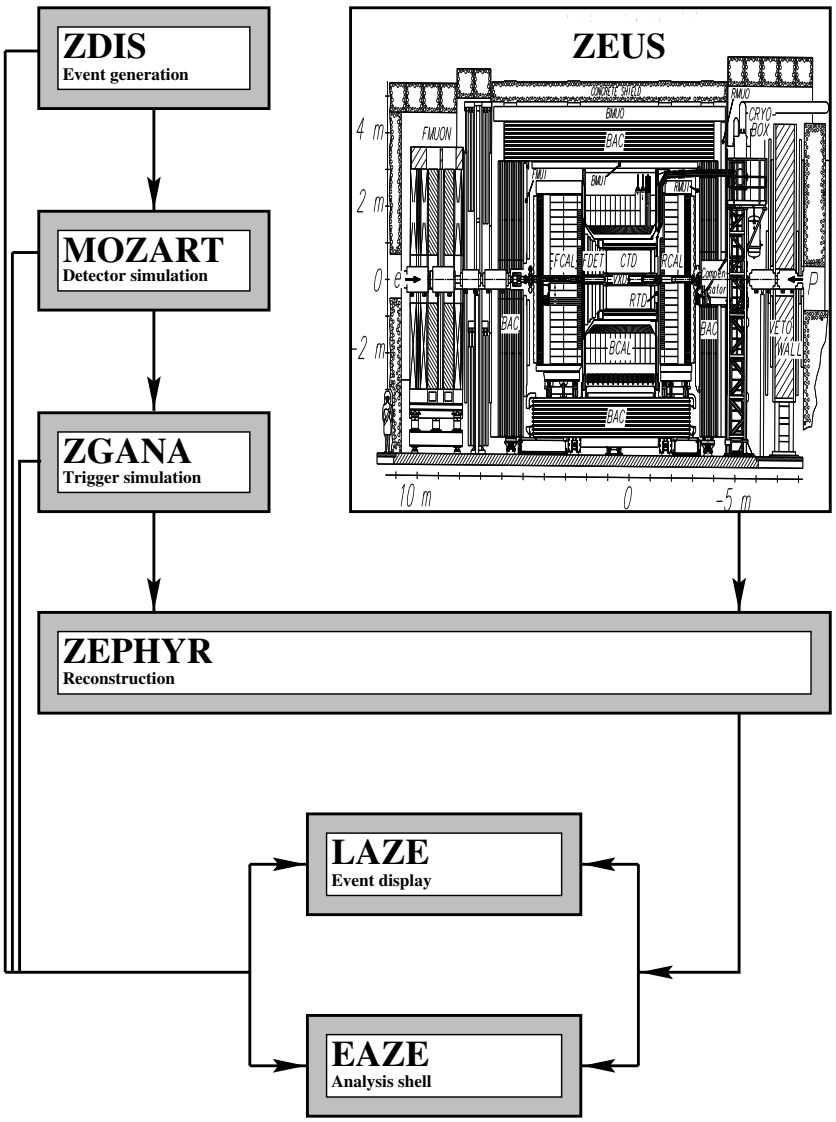

Figure 2.10 - Interrelationship of the ZEUS offline and Monte Carlo (MC) simulation programs.

events can be saved for further analysis. The program LAZE is an event display program which allows to view graphically various aspects of an event including e.g. the tracks of charged particles in the CTD, energy depositions in the CAL, and other component-related quantities. To allow fast access to specific types of events during reconstruction it is checked wether each event meets one of the conditions designed by the ZEUS analysis groups. If a specific condition is met, a flag called a DSTBIT is set. Before analyzing detailed component information in the user's EAZE program, the events can be preselected by requiring certain DSTBITS. This allows a faster loop over the whole data sets since only those events are processed further. In most cases the DSTBITs correspond to certain TLT slots.

MC events are generated using the program ZDIS which contains a shell environment to steer a number of MC generator programs. The output data is stored in the same (ADAMO) format as the data from the real detector and passed to the ZEUS

detector simulation program MOZART, based on the CERN GEANT program [Br89]. A simulation of the ZEUS trigger chain is done by the program ZGANA. Interfaces between the programs used for MC generation and the programs EAZE and LAZE provide specific MC information such as generated kinematic quantities, vertices and particles to the user. An overview of the physics analysis environment of the ZEUS experiment can be found in [Ba95].

Chapter 3

Jets

3.1 Jets in QCD

In HEP reactions partons are produced in the final state as a result of the hard underlying process. Because of color confinement it is not possible to observe quarks and gluons as final-state particles of the reactions. The partons will radiate other partons (parton shower) and will finally recombine to form color-singlet states (hadrons). This last process is called hadronization.

The resulting hadrons will form a collimated "stream" of particles around the direction of the original parton. This collimation of the final-state particles around the direction of the initial partons has to do with the fact that the transverse energies involved in the hadronization process are of the order of 300 MeV while the hard scatterings are of the order of several GeV. These collimated flows of particles are called *jets*. Jets will be correlated to the primary partons, but one should not think that by measuring jets we are measuring a primary parton. The jet is merely an event property that is largely determined by the primary parton [Se95].

During a HEP reaction, the low transverse momentum particles are also generated from the extra hadronic activity in the event (not directly related to the hard scattering) and form the *soft underlying event*. The soft underlying event overlaps with the jet formed by the hard scattering. This is one of the difficulties in assigning final state jets to original partons. The hadronization effects are generally theoretically not understood and are estimated using phenomenological models.

3.2 Jet Finders

A jet algorithm assigns partons or hadrons to jets and calculates the physical quantities (transverse energy, pseudorapidity, etc.) related to these new objects (jets). There are different ways of defining jets. A jet should be well defined and easy to measure from the hadronic final state, easy to calculate order-by-order in pQCD, and it should have a close correspondence to the outgoing partons. For quantitative measurements, jets are defined using jet finding algorithms which are based on the

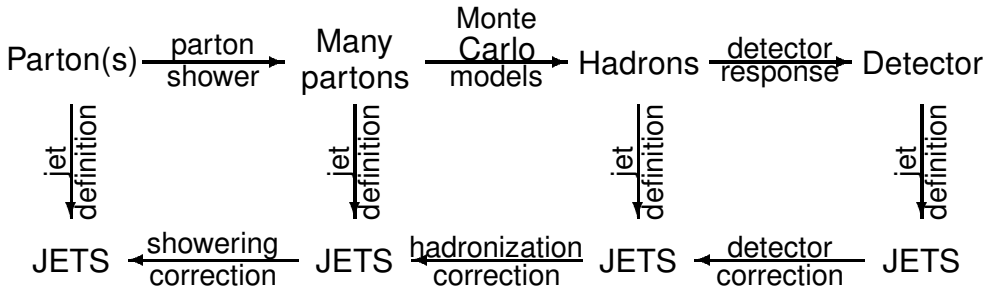

Figure 3.1 - Schematic diagram of a typical analysis using jets [Se95]. In the upper line the partons are produced from the hard scattering process and then radiate other partons (parton shower). Color-singlet states (hadrons) are produced through the process of hadronization. The hadrons deposit energy in the detector. At each stage the jet finding can be applied. From the measured data by the detector one can correct backwards, in principle, down to the parton level.

assumption that the final state particles belonging to a jet are close to each other in phase space.

There are two main types of jet-finders (algorithms) commonly used: the cone algorithms, used mainly in $p\bar{p}$ experiments, and the clustering algorithms, used mainly in e^+e^- experiments. The cone algorithms define a direction that maximizes the energy flowing into a cone drawn around it. The clustering algorithms are based on iterative clustering procedures in which particles are merged together into pseudoparticles, which are the output jets.

From the theoretical and from the experimental points of view, a jet finding algorithms should fulfill the following two requirements:

1. **collinear safe** : the jet finding should treat a collinear pair of particles identically to a single particle with their combined momentum. From the theoretical point of view this means that the jet finding is independent of a particle splitting into two parallel travelling partons. Such a dependence would cause divergencies in the theoretical calculations, which are called *collinear divergencies*.

   From the experimental point of view, such a property means that the jet finding is largely independent of the granularity of the detector. Particles which go in the same calorimeter cell cannot be resolved anyway.

2. **infrared safe** : the jet finding should be insensitive to the emission of low energy particles. Theoretically, this property avoids the soft divergencies in perturbative calculations. Experimentally, cuts to suppress the detector noise are applied to make the jet finding as independent as possible of low energy deposits.

A schematic diagram of an analysis using jets is shown in figure 3.1. The jet finding can be done on: 1. detector objects (for example calorimeter cells), 2. hadrons or 3. partons. The comparison with the theory should be done at parton level but, since the hadronization corrections are difficult to calculate and are model dependent, the comparison in this analysis is done at the hadron level.

3.2.1 The Snowmass Convention

Jet finding algorithms are applied to objects in the final state. These can be calorimeter cells or hadrons (partons) in the final state of real events or a Monte Carlo simulated events. Below it is explained the way these objects are assigned to jets. After the jets are defined, the transverse energy and the coordinates (angles) of the jet are calculated from the energies and coordinates (angles) of the objects which form that jet. The quantities used in this analysis to characterize jets, namely the transverse energy, E_T^{jet}, the pseudorapidity [1], η^{jet}, and the azimuthal angle, ϕ^{jet}, are calculated using the *Snowmass Convention* [Hu90] :

$$\begin{aligned} E_T^{jet} &= \sum_i E_T^i \,, \\ \eta^{jet} &= \frac{1}{E_T^{jet}} \sum_i E_T^i \cdot \eta^i \,, \\ \phi^{jet} &= \frac{1}{E_T^{jet}} \sum_i E_T^i \cdot \phi^i \,, \end{aligned} \tag{3.1}$$

where the sums in the above expressions run over all the objects assigned to the given jet.

3.2.2 Cone Algorithm

There are different cone algorithms generally used. They all associate hadrons within a cone of radius R in the $\eta - \phi$ space to the same jet. Here we discuss shortly the cone algorithm which is traditionally used (EUCELL) [El92].

At the beginning clusters are determined using a grid in the $\eta - \phi$ space. All the objects with transverse energy larger than a certain value (at ZEUS this is 300 MeV) are selected as seed "cells" for beginning the jet finding.

A cone of radius R is then placed around the seed with highest transverse energy and all objects within this cone, that is all objects fullfilling the condition

$$(\phi_{object} - \phi_{seed})^2 + (\eta_{object} - \eta_{seed})^2 < R^2 \tag{3.2}$$

are assigned to a jet and this jet (the objects belonging to it) is removed from further consideration. This procedure is repeated until no seed above the threshold is found. Typical values for the cone radius are $R = 1$ and $R = 0.7$.

Such an algorithm can be run with an upper pseudorapidity (η) cut on the found jets, so that very little, if any, proton remnant is included in the jets found. Cone algorithms are collinear safe but not infrared safe at higher orders. Low energy radiation between two jets done in the $\eta - \phi$ plane could lead to a change of the seed position and, consequently, the found jets can be completely different.

[1] The pseudorapidity η is defined as $\eta = -\ln\left(\tan\frac{\theta}{2}\right)$, where θ is the polar angle with respect to the proton beam direction

The cone algorithms are usually faster to implement than clustering algorithms for this reason, they are used at the TLT trigger stage. The main problem of cone algorithms is the overlapping of jets, these algorithms are not able to unambiguously separate between jets which overlap. In addition, there is a bias coming from the choice of seeds.

3.2.3 Clustering Algorithms

The clustering jet finding algorithms have some advantages in comparison to the cone algorithms. The clustering algorithms have no overlapping jets since they unambiguously assign every object to a single jet. Furthermore, that is there is no seed choice dependence. The clustering algorithms are collinear and infrared safe.

Here we describe shortly the longitudinally invariant k_T-cluster algorithm [Ca93]. The k_T algorithm is applied in the following steps:

1. for every object i its distance to the beam is calculated as $d_i = E_{Ti}^2$
2. for every pair of objects the distance between them is calculated in the following way: $d_{ij} = min\left[E_{Ti}^2, E_{Tj}^2\right] \cdot \left((\eta_i - \eta_j)^2 + (\phi_i - \phi_j)^2\right)$
3. If the smallest of all the d_i and d_{ij} quantities is a d_{ij}, the objects i and j are recombined into a new object k following the p_T recombination scheme:

$$\begin{aligned} E_{Tk} &= E_{Ti} + E_{Tj} \\ \eta_k &= \frac{E_{Ti} \cdot \eta_i + E_{Tj} \cdot \eta_j}{E_{Ti} + E_{Tj}} \\ \phi_k &= \frac{E_{Ti} \cdot \phi_i + E_{Tj} \cdot \phi_j}{E_{Ti} + E_{Tj}} \end{aligned}$$

4. If the smallest of all d_i and d_{ij} quantities is a d_i the object i is defined as a protojet and is no longer merged. This protojet is removed from the further clustering.
5. the procedure is repeated for the remaining particles until none is left.

Jets are all the protojets with the transverse energy above a certain (analysis defined) value E_T^{cut}.

3.3 Jet Internal Structure

A large fraction of the hadronic final states in hadron-hadron, electron-hadron and electron-positron collisions consists of high-energy jets. These jets have an extended structure in phase space which can be studied both experimentally and theoretically. Measurements of the internal structure of jets are very interesting because

the hard and soft part of QCD are probed. Possible measurements of such structure are jet shapes and subjets, which are defined in sections 3.3.1 and 3.3.2.

The internal structure of jet is expected to depend mainly on the type of primary parton, quark or gluon, and to lesser extent on the particular hard scattering process. In QCD there are three fundamental vertices representing the three- and four-gluon coupling, and the coupling of a quark current to a gluon. Neglecting the four gluon coupling, which is $\mathcal{O}(\alpha_S^2)$, three fundamental processes are described by these vertices : radiation of a gluon by a quark ($q \rightarrow qg$) or by another gluon ($g \rightarrow gg$) and the splitting of a gluon into quark-antiquark pair ($g \rightarrow q\overline{q}$). The probabilities of these processes are given by the splitting amplitudes and are proportional to the colour factors C_F, C_A and T_F, respectively (which are the structure constants of the SU(3) colour symmetry group of QCD). As the main contribution to particle production in hadronic events is due to radiation of gluons, the internal structure of jets is mostly sensitive to C_A and C_F.

Calculations of multiplicity distributions in QCD [El96] predict that the average multiplicity of any type of object in a gluon jet should asymptotically become C_A/C_F times larger than in quark-initiated jets :

$$\langle N_g \rangle \sim \frac{C_A}{C_F} \langle N_g(Q^2) \rangle \tag{3.3}$$

The multiplicity distribution should also become wider for a gluon jet by a factor $\sqrt{C_A/C_F}$

$$\sigma_{N_q} \sim \left(1 + \frac{C_F}{3C_A}\right) N_q^2 \quad ; \quad \sigma_{N_g} \sim \frac{4}{3} N_g^2 \,, \tag{3.4}$$

where σ_{N_q} (σ_{N_g}) are the second multiplicity moments for quark(gluon) jets. At sufficiently high transverse energy of the jet, the internal structure of jets is expected to be driven mainly by gluon emission of the primary parton (figure 3.2. The differences between quark and gluon jets arise from the larger strength of the gluon-gluon coupling ($\sim C_F$) with respect to that quark-gluon coupling ($\sim C_A$). As a consequence, QCD predicts gluon jets to be broader than quark jets.

3.3.1 Jet Shapes

The *differential jet shape* is defined as the average fraction of the jet's transverse energy that lies inside an annulus in the η - ϕ plane of inner (outer) radius $r - \Delta r/2$

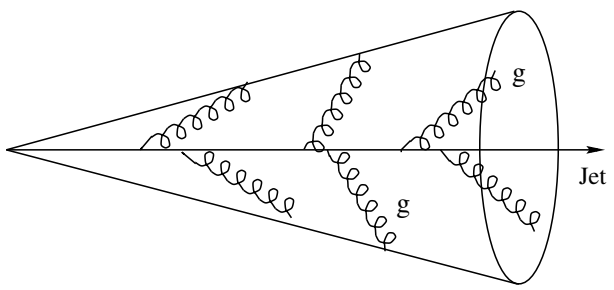

Figure 3.2 - Gluon radiation within a jet.

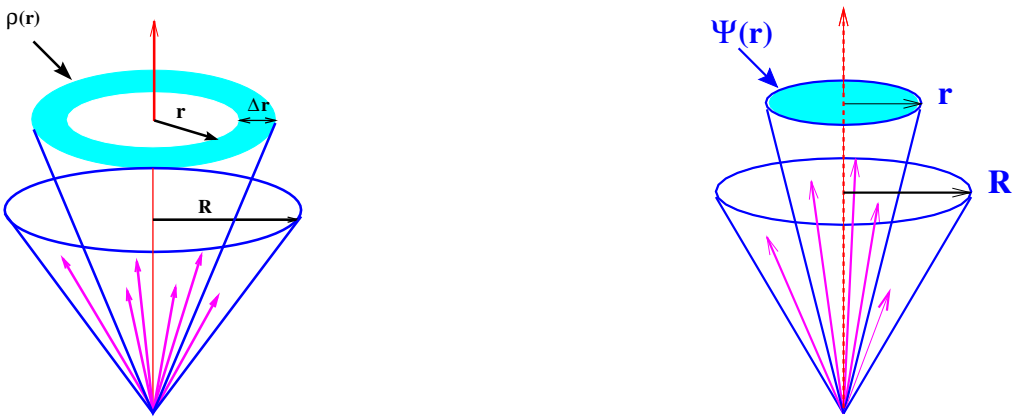

Figure 3.3 - Differential (left) and integrated (right) jet shape definitions

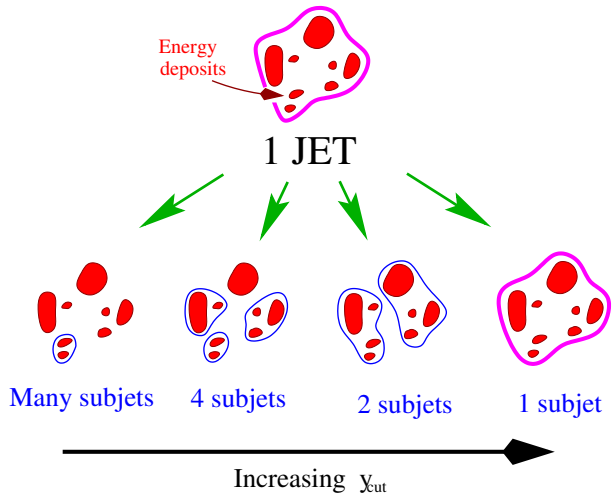

Figure 3.4 - The internal structure of jets can be studied by resolving jet-like structures ("subjets"). As the resolution scale y_{cut} decreases an increasing number of "subjets" is resolved.

$(r + \Delta r/2)$ concentric with the jet axis (see figure 3.3) :

$$\rho(r) = \frac{1}{N_{jets}} \sum_{jets} \frac{1}{\Delta r} \frac{E_T(r - \Delta r/2, r + \Delta r/2)}{E_T(0, R)} , \tag{3.5}$$

where $E_T(r - \Delta r/2, r + \Delta r/2)$ is the transverse energy within the given annulus and N_{jets} is the total number of jets in the sample. The measurements of jet shapes have been done with r values varying from 0.05 to 0.95 in $\Delta r = 0.1$ increments and R=1.

The *integrated jet shape* is defined as (see figure 3.3) :

$$\Psi(r) = \frac{1}{N_{jets}} \sum_{jets} \frac{E_T(0, r)}{E_T(0, R)} \tag{3.6}$$

This quantity has been measured for r values varying from 0.1 to 1.0 in $\Delta r = 0.1$ increments and R=1. By definition, $\Psi(R) = 1$.

3.3.2 Subjets

The *"subjets"* are jet-like structures within a given jet. To define such structures the K_T clustering algorithm is re-applied to all the particles assigned to a given jet until the distances between every pair of particles verify for a given resolution scale (y_{cut})

$$d_{ij} > y_{cut} \left(E_T^{jet} \right)^2 \tag{3.7}$$

At each y_{cut} the resulting particles found inside a jet are called *"subjets"*. The mean number of subjets inside a jet ($< n_{sbj} >$) or "mean subjet multiplicity" is an observable which can be measured and compared with pQCD predictions.

The number of "subjets" inside a jet increases as the resolution scale decreases (see figure 3.4). For small values of y_{cut} the hadrons inside the jet are resolved.

If the transverse energy of the jet is of the order of E_T^{jet} ~10 GeV, to be able to resolve subjets of transverse energy of $E_{T_i} \sim 1$ GeV the resolution scale must be of the order of $y_{cut} \sim 10^{-2}$. In this case, for resolution scales smaller than $y_{cut} \sim 10^{-2}$ perturbative QCD cannot be applied. As the transverse energy of the jet increases, perturbative QCD calculations can be performed for smaller values of the resolution scale.

3.4 Jet production in DIS at HERA

Jet production in DIS is the manifestation of QCD effects and, therefore, a sensitive probe of colour dynamics. Studies of jets in DIS provide a testing ground for understanding perturbative and non-perturbative aspects of QCD.

At HERA, clean jet structures can develop thanks to the large available center-of-mass energy. In the identification of jets from the hard subprocess, it is preferred to have as little contamination as possible from the remnant of the proton. Therefore, the jet finders must have some feature which reduces this contamination. The most suitable algorithm for jet studies at HERA is the K_T algorithm. In the K_T algorithm the clustering of particles is weighted in transverse energy which implicitly removes the proton remnant (E_T[proton remnant]~ 0) .

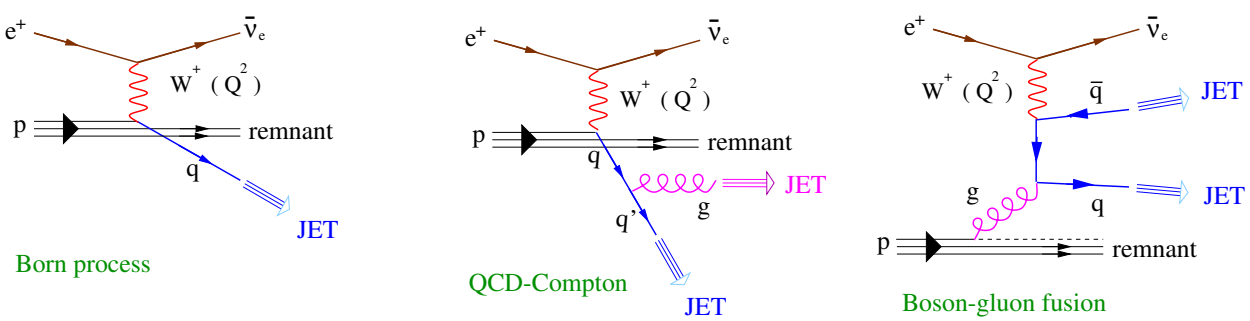

Figure 3.5 - Feynman diagrams of different processes in Charged Current interactions at HERA: i) Born, ii) QCD-Compton and c) boson-gluon fusion processes.

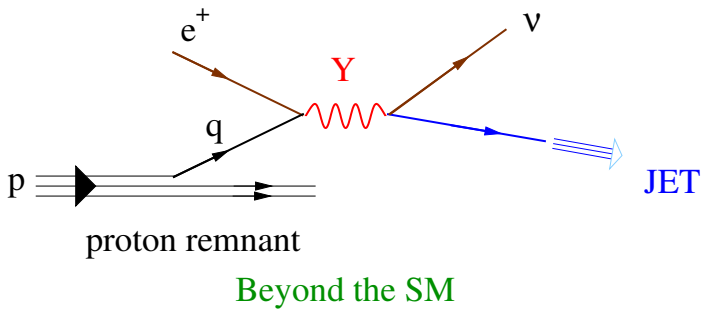

Figure 3.6 - An example of production of a new particle in Charged Current DIS.

Jet production in CC-DIS ($e^+p \rightarrow \overline{\nu_e} + \text{jet(s)} + X$) is described in the SM at lowest order in perturbation theory by the Born process (see figure 3.5), i.e. the scattering of the lepton off a quark in the proton via the exchange of a virtual W boson. Multi-jet production is described up to order $\mathcal{O}(\alpha_s)$ by the QCD Compton (QCDC) and boson-gluon fusion (BGF) processes (see figure 3.5). Due to the latter contribution multi-jet cross sections are directly sensitive to the gluon density of the proton.

The measurement of jet cross sections via charged current interactions provides a test of QCD and is sensitive to the production of new particles and new interactions (see figure 3.6).

Chapter 4

Data Selection

In this chapter the selection criteria for the charged current event sample is presented. The data used for the present analysis were collected with the ZEUS detector during the 1995-1997 data runs and correspond to an integrated luminosity of 44.97 pb^{-1}.

4.1 The $\not{p}_t$ threshold and background events

CC DIS events can be distinguished from events originated from NC DIS processes by the presence of a large missing transverse momentum ($\not{p}_t$) due to the undetected outgoing neutrino. The $\not{p}_t$ value is related to the event kinematics (see equation 1.8). In figure 4.1 lines of constant $\not{p}_t$ in the (x, Q^2) plane are shown. In order to obtain events in the lower Q^2 and higher y regions, it is preferable to keep the $\not{p}_t$ threshold as low as possible. In this analysis a threshold of $\not{p}_t > 11$ GeV is used.

However, the low $\not{p}_t$ threshold allows for more background events from other ep processes. Possible sources of background are photoproduction and NC DIS events with large transverse energy. This type of events can display relative large values of $\not{p}_t$ due to the limited resolution of the CAL or due to the presence of muons resulting from the decay of heavy quarks. Although the probability for these configurations is very low, the contamination from these processes is important since they have much larger cross sections than that of CC DIS. The most effective criterion to reduce this contamination is to require a large value of $\not{p}_t/E_t$ since the $\not{p}_t$ in such background events is likely to be caused by a fluctuation in the measurement of a large tranverse energy deposit.

Furthermore, there are considerable amount of events with a large $\not{p}_t$ originating from non-ep interactions. Cosmic-ray muons falling on the top part of the detector (called "*cosmic ray*" events) and beam-halo muons passing through the detector along the z-direction (called "*halo-muon*" events) can give rise to a large and localized energy deposit in the CAL, which results in a large value of $\not{p}_t$. Another important source of background is the p-gas porcess (called "*beam-gas*" events). In these events, large energy deposits are detected close to the forward beam pipe, mostly in the innermost ring of the FCAL. To remove this type of events the value of

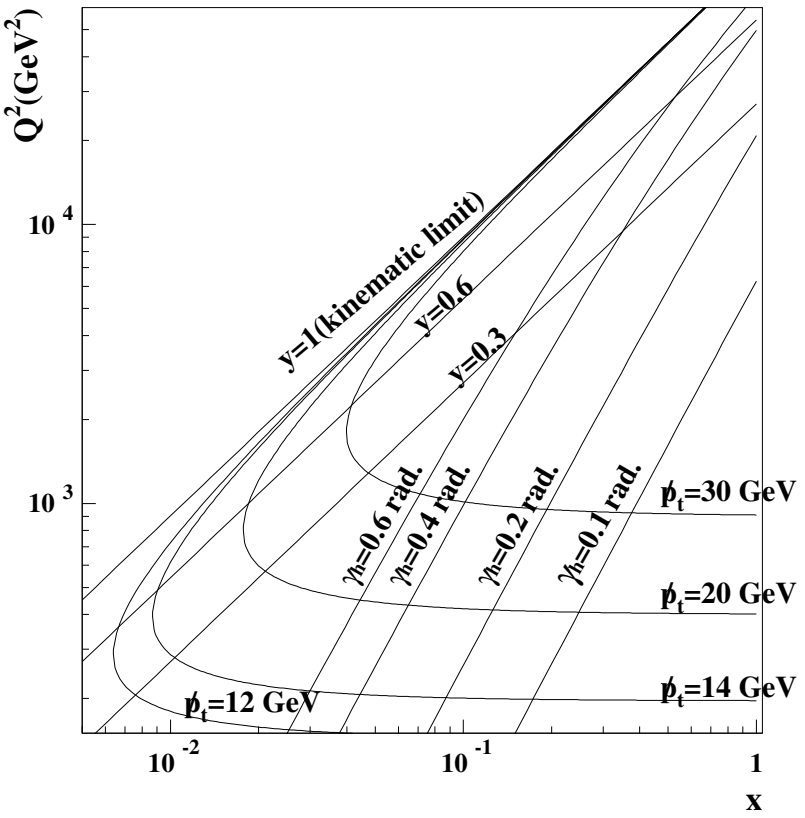

Figure 4.1 - Lines of constant p_t, γ_h and y in the (x, Q^2) kinematic plane.

$\not{p}_t$ excluding the FCAL first ring, $\not{p}_t^{1r}$, is calculated and it is required to be above a certain threshold.

The CC data sample was selected by applying both online and offline cuts. The details of the selection procedure are presented in the forthcoming sections.

4.2 Online Event Selection - Trigger Logic

The CC sample was selected online with the ZEUS three level trigger system. The cuts applied by the first, second and third level trigger constitute the online selection. The particular trigger algorithms used in this analysis select events with missing transverse momentum measured from the main calorimeter. These events are good candidates for charged-current interactions.

4.2.1 First Level Trigger

The First Level Trigger requires a certain minimum amount of energy to be detected in the main calorimeter (CAL). At least one of the following conditions must be ful-

filled for the event to pass the first level trigger :

- the missing transverse momentum ($\not{p}_t$) and the transverse energy excluding the innermost and second innermost FCAL rings (E_t^{-2r}) have to be greater than 5 GeV and the presence of at least one *good track* [1] is required in the event.
- the missing transverse momentum must be greater than 8 GeV and either the energy in the FCAL must be greater than 10 GeV or the event must contain at least one CTD track.

To increase the trigger efficiency for CC DIS events , other subtriggers based on calorimeter energies are also used. If the event verifies at least one of the requirements listed below is also selected :

- the transverse energy in the calorimeter must be greater than 30 GeV;
- at least one *good track* is required and at least one of the following conditions must be fullfilled :

- the total energy in the calorimeter is greater than 15 GeV;
- the transverse energy is greater than 11.5 GeV;
- the total calorimeter energy deposited in the EMC cells is greater than 10 GeV;
- the total energy deposited in the EMC cells of the BCAL is greater than 3.4 GeV;
- the total energy deposited in the EMC cells of the RCAL is greater than 2 GeV;

- the total energy deposited in the EMC cells of the BCAL (RCAL) is greater than 4.8 GeV (3.4 GeV).

4.2.2 Second Level Trigger

The Second Level Trigger has a larger latency than the first level trigger, but has access to the entire calorimeter event information (pulse times of the photomultipliers and a preliminary vertex from the central tracking detector CTD). Therefore, more precise selection algorithms are applied at this stage.

One of the following conditions has to be fulfilled for the event to be accepted by the SLT :

- $\not{p}_t^{SLT} > 6$ GeV , $E_t^{-2r} > 6$ GeV and at least one *good track* is required;
- $\not{p}_t^{SLT} > 9$ GeV , $E_t^{-1r} > 8$ GeV and $E_{FCAL} > 20$ GeV ,

[1] A good track at FLT is defined as a CTD track with the hits aligned in the z-direction so that they point to the nominal interaction point

where E_t^{-1r} (E_t^{-2r}) is the transverse energy in the calorimeter calculated excluding the first (first and second) ring of the FCAL.

All the readout systems of the ZEUS sub-components are synchronous to the HERA clock. The calibration of them is such that an ep collision occuring at the ZEUS nominal interaction point results into a measured event time equal to zero. An interaction occurring outside the interaction region will produce time shifts in one direction or the other. Cuts are applied to the times measured by different components in order to reject events coming from outside the interaction region. The second level trigger rejects more precisely beam-gas events and other non-ep background events.

In the case of the trigger designed for selection of CC events, the accepted events must verify that :

- the average CAL timing, t_{global}, must be less than 7 ns in absolute value.

4.2.3 Third Level Trigger

The time the third level trigger has available for making a decision is about $100ms$. This is much larger than the corresponding times at the first level trigger, $5\mu s$, and the second level trigger, $20ms$. The full event information from the different components of the ZEUS detector is available at the third level, allowing more stringent and finer cuts to be applied. At this level a complete tracking reconstruction is performed. In comparison to the offline level the tracking is not as refined due to time limits.

One of the following conditions has to be fulfilled for the event to be accepted by the TLT :

- $\not{p}_t^{TLT} > 8$ GeV and either $E_{FCAL}^{TLT} > 10$ GeV or the event has at least one TLT *good track* [2];
- $\not{p}_t^{FLT} > 6$ GeV and at least one *good track* is required.

Non-ep background contaminations are further reduced by requiring all the following conditions :

- A vertex cut is applied, $|z_{vertex}| < 60$ cm. The ep interactions occur around the region $z_{vertex} = 0$. Beam-gas events can occur anywhere and the restriction on the vertex will cut out much more background than ep events. If no information on the CTD vertex exists, the vertex is set to zero (all three coordinates);
- $t_{BCAL\,top} - t_{BCAL\,bottom} > -10$ ns, which rejects events due to cosmic muons leaving energy in the calorimeter and moving from top to bottom. The event times are calculated using energy weighted means of calorimeter channels above a threshhold of 200 MeV.

[2] A good track at TLT is defined as a CTD track with $p_t > 0.5$ GeV, the distance of closest approach (DCA) of the extrapolated track to the z-direction is less than 1.5 cm and the DCA in the z-direction must be less than 60 cm.

4.3 Offline Event Selection

Detailed calibration of the detectors, noise studies and the full reconstruction can only be made offline and not during data taking. Therefore, the offline selection cuts are more accurate than the ones at the trigger level and increase the purity of the sample.

4.3.1 General Selection

The event sample selected with online cuts is further required to verify the following cuts :

- $\not{p}_t > 11$ GeV. The trigger simulation indicates that this cut is sufficiently far above the 9 GeV trigger threshold to ensure high trigger efficiency;
- the event has to have a fitted tracking vertex, determined from at least one track compatible with intersecting the beam line. The vertex position must verify $|Z_{vertex}| < 50$ cm. This cut eliminates a large fraction of non-ep background;
- $\frac{\not{p}_t^{-1r}}{\not{p}_t} > 0.8$. This cut rejects beam-gas events and p-beampipe colisions, in which the $\not{p}_t$ is concentrated in the first ring around the forward beampipe;
- at least one *good track* [3] is required. This requirement removes cosmic-ray events and beam-gas interactions with spurious vertices caused by low-energy secondary interactions in the beampipe;
- $|\Delta\phi| < 1$ rad, where $\Delta\phi$ is the difference between the azimuthal angle of the net momentum calculated with *good tracks* and the azimuthal angle measured by the calorimeter. This requirement removes events with overlays of a cosmic ray and ep interactions;
- $\not{p}_t^{\text{good tracks}}/\not{p}_t > 0.1$, where $\not{p}_t^{\text{good tracks}}$ and $\not{p}_t$ are the transverse momentum calculated with *good tracks* and the calorimeter, respectively. This cut removes non-ep related energy deposits in the calorimeter and is complementary to the previous requirement;
- $\not{p}_t/E_t > 0.5$. This cut requires an azimuthal collimated energy flow and rejects photoproduction and beam-gas background events;
- if the cell with maximal transverse energy in the CAL has more than 70% of the total transverse energy in the CAL, the event is removed from the sample. This criterium is used to exclude events in which a cosmic muon or a spark produces large values of $\not{p}_t$;
- A pattern recognition algorithm, MUFFIN [Kr98], based on the topology of the calorimeter energy distribution and the signals detected in the muon chambers is applied to reject cosmic-rays and halo-muons.

[3] A *good track* is defined as a reconstructed CTD track originated from the vertex with a polar angle between $15°$ and $164°$ and a transverse momentum exceeding 0.2 GeV.

Simulations of ep background due to NC DIS show that some of these events still pass the above cuts so that additional cuts must be applied to remove them.

4.3.2 Rejection of NC DIS events

The rejection of NC DIS events is based on the fact that in this type of events there is a positron in the final state. To reject NC-DIS events the electron finder Sinistra95 [Ab95] is used, this algorithm searches for positron candidates in the main calorimeter. Sinistra analyses clusters ("islands" of $3x3$ calorimeter cells around the highest energy cell) of energy depositions in the calorimeter and information such as the ratio of energy deposited in the electromagnetic part to the total energy deposited, the shower profile, tracking information, etc. A neural network is used to optimize the electron identification.

The event is removed from the sample if one of the following conditions is verified :

- $20^\circ < \theta_{e^+} < 140^\circ$
  - there is a positron candidate with energy larger than 10 GeV, which is *isolated* and the energy distribution is *narrow*;
- $\theta_{e^+} > 140^\circ$
  - there is a positron candidate with energy larger than 10 GeV and transverse momentum $\not{p}_t^{e^+} > 11$ GeV;
  - $y_{e^+} < 0.7$ and the Sinistra probability for the positron candidate is larger than 0.95.

A e^+ candidate is said to be *isolated* if the ratio of the energy of the CAL not associated to the candidate within a cone of radius $R = 0.7$ around the candidate over the energy of the positron is smaller than 0.1.

A e^+ candidate is said to be *narrow* if at least 90% of the energy of the positron is contained in a cone of radius $R = 0.3$ around the positron direction.

4.3.3 Uranium-noise and spark suppression

As the calorimeter uses depleted uranium as an absorber, the radioactivity of the uranium produces background noise. An energy cut of 60 (100) MeV was applied to the EMC (HAC) cells. This threshold was raised to 100 (150) MeV for isolated EMC (HAC) cells. These tresholds were determined in a study using randomly triggered events [Sa98].

Photomultipliers sometimes suffer a discharge ("spark"), which results in a fake energy deposit in the calorimeter. This effect can be avoided by removing cells which have a large energy imbalance between the pulse-heights measured by the two photomultipliers of the cell. For all cells with measured energy greater than 1.5 GeV, the

following condition is required :

$$\frac{|E_L - E_R|}{E_L + E_R} > 0.9/;, \tag{4.1}$$

where E_L and E_R are the energies measured by the left and right side photomultipliers, respectively. The threshold was also determined from the study based on randomly triggered events.

4.4 Jet selection

Jets are found using the k_T jet finding algorithm applied to the UCAL cells in the laboratory frame. Events with one or more jets in the final state are selected. The jets are ordered according to transverse energy. The jet selection is then done in the following way :

- in the laboratory frame
  - $-1 < \left(\eta^{jet}\right)_i < 2$
  - $\left(E_T^{jet}\right)_i > 8$ GeV

4.5 Kinematic cuts

The analysis is restricted to the kinematic region

$$\begin{aligned} Q^2 &> 200 \text{ GeV}^2 \quad \text{and} \\ y &< 0.9 \, . \end{aligned} \tag{4.2}$$

The y cut is needed since the x and Q^2 resolutions degrade at high y. From equation 1.8, the Q^2 resolution is expressed as

$$\frac{\Delta Q^2}{Q^2} = \sqrt{4\left(\frac{\Delta p_t}{p_t}\right)^2 + \left(\frac{\Delta y}{1-y}\right)^2} \, , \tag{4.3}$$

which degrades at $y \approx 1$.

In addition, for a NC-DIS event without any initial-state QED radiation, the value of $E - P_z$ is conserved since the particles which escape through the forward beampipe carry little $E - P_z$. Hence, $E - P_z$ peaks at $2 \cdot E_e = 55$ GeV for NC-DIS events. From equation 1.8 it can be infered that $y_{JB} \sim 1$ for NC-DIS events. Therefore, the cut $y < 0.9$ reduces the NC-DIS background.

4.6 Charged Current event sample

After applying the above selection criteria to the data collected with the ZEUS detector during the years 1995-1997, 860 charged current candidates were selected (see table 4.1). After applying the jet selection criteria an inclusive jet sample of 764 events remained; 61 of these events have two or more jets in the final state.

Events passing selection cuts (44.97 pb^{-1})	
	Number of Events
CC selection	860
Kinematic cuts	825
Inclusive Jet cuts	764
Dijet cuts	61

Table 4.1 - Number of events passing the cuts for the CC sample. The total luminosity for this sample is 44.97 pb^{-1}.

An example of a charged current event with one jet registered with the ZEUS detector is shown in figure 4.2 . The energy and position measurements of the uranium calorimeter and the central tracking chamber for the event are displayed in the left side of the plot, where the $r - Z$ projection is shown. A large energy deposit in the barrel region associated to the jet. There is a well defined vertex defined by the tracks close to the nominal interaction point and a large energy deposit around the beampipe, associated with the proton remnant. The transverse momentum in the calorimeter is not compensated. The right side of the figure shows the transverse energy deposits in the calorimeteras viewed in the $\eta - \phi$ plane. A clear hadronic jet is distinguished.

An example of a charged current dijet event registered with the ZEUS detector is shown in figure 4.3 . Large energy deposits in the barrel and forward regions associated to the two jets are seen. There is a well defined vertex defined by the tracks close to the nominal interaction point. The left side of the figure shows the transverse energy deposits in the calorimeter as viewed in the $\eta - \phi$ plane. Two clear hadronic jets are distinguished.

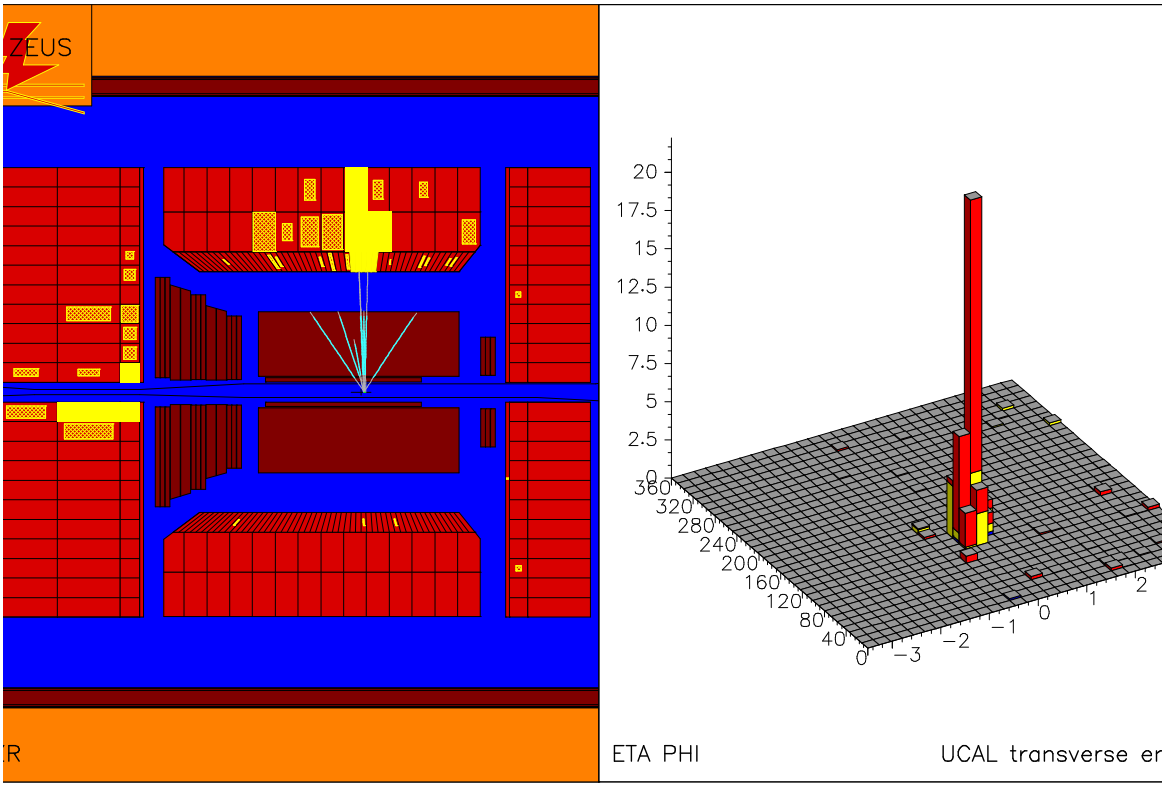

Figure 4.2 - Example of a charged current one-jet event registered with the ZEUS detector. The energy and position measurements of the uranium calorimeter and the central tracking chamber for the event are displayed in the left side of the plot, where the $r - Z$ projection is shown. The right side of the figure shows the transverse energy deposits in the calorimeter as viewed in the $\eta - \phi$ plane.

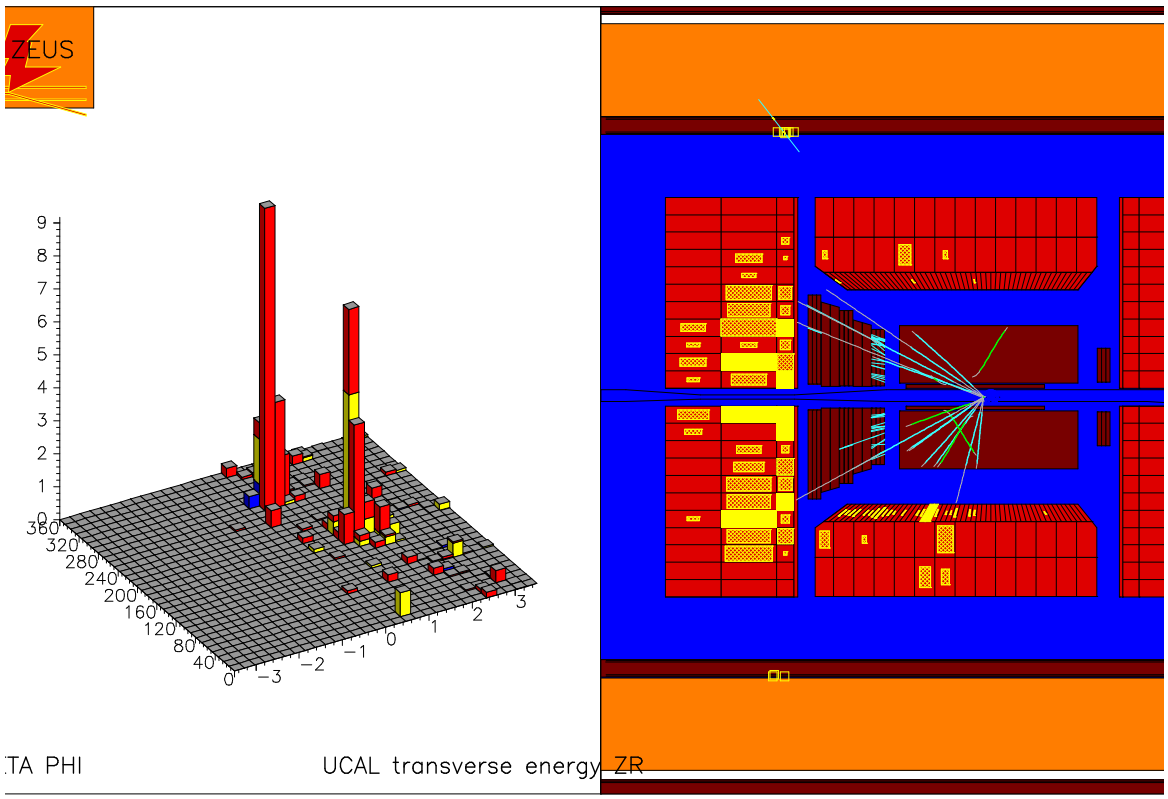

Figure 4.3 - Example of a charged current dijet event registered with the ZEUS detector. The energy and position measurements of the uranium calorimeter and the central tracking chamber for the event are displayed in the right side of the plot, where the $r - Z$ projection is shown. The left side of the figure shows the transverse energy deposits in the calorimeter as viewed in the $\eta - \phi$ plane.

Chapter 5

Event and Detector Simulation

The experimental measurements result from the convolution of hard-scattering processes with various detector effects. This gives rise to complex final states. Therefore, the relation of the measurements with the physical quantities is not straight forward: first, we do not always understand completely the physics of the hard-scattering processes; second, the detector effects cannot be described analytically. In order to extract the physical observables from the measured quantities one has to correct for all detector related effects. This is usually done by using Monte Carlo methods.

Monte Carlo methods are an essential tool in experimental HEP. They are used to simulate complete events. The simulation is divided into the *physics simulation* and *detector simulation*. The generated events (MC events) can be used to correct the data for detector effects (acceptance, smearing, kinematic cuts, etc.) and for the extraction of physical quantities from the measurements. This can be done under the condition that the simulated final-state quantities model well those measured with the detector. Under this condition it is ensured that both the detector and the underlying physics are simulated properly.

The physics simulation at HERA is divided into separate steps:

- **Hard Scattering**: perturbative QCD is used for calculating the cross section of the hard scattering at leading or higher orders.
- **Parton Showering**: simulation of the initial- and final-state QCD radiation.
- **Hadronization**: Partons fragment into color neutral hadrons. This process is called hadronization. Hadronization is a non-perturbative process and various models are used for its simulation.

The output of the physics simulation is the four-vectors of all particles (hadrons and leptons) which are fed into the detector simulation, which is based on the GEANT package [Br87]. A detailed simulation of the geometry and materials of the detector is performed at this stage. In addition, the three level trigger is simulated. The program used for detector simulation is has been developed so as to give the best possible description of the response of the detector. The full GEANT simulation

of the ZEUS detector is done using the program MOZART (Monte Carlo for Zeus Analysis, Reconstruction and Trigger). For every particle MOZART simulates its interaction with the detector material, possible decays, the signals produced in the different components (tracking, calorimeters) and the digitisation of the signals, including the various sources of noise. Finally, the information from the detector and trigger simulation of the events is written to tape in an identical format as the real data. This allows to pass the Monte Carlo events through the same reconstruction chain and selection as the data.

The stage after the parton showering is called *parton level*, the one after the hadronization *hadron level* and the final one *detector level*.

In this chapter the following topics are considered :

- The Monte Carlo models used for correcting the data are described.
- Comparisons between data and MC generated events made in order to show the description of the data by the simulation.

5.1 Monte Carlo Models

In this analysis the DJANGOH [Sc91] Monte Carlo package is used to correct the data (DJANGOH6 v2.4). DJANGOH is an interface between HERACLES [Kw92] and LEPTO [In97] or ARIADNE [lö02].

The HERACLES program simulates the ep-DIS process including first-order EW radiative corrections An incoming parton is generated according to the SM EW cross-section formula and the corresponding PDF so that a hard scattering between the parton and the virtual boson is simulated. This is the Born process $V^*q \rightarrow q'$, where V^* denotes generally a virtual vector boson, q denotes a quark and q' denotes the scattered quark. The parton distribution functions used can be selected from many parametrizations compiled in the PDFLIB [Pl93] library. In this analysis the CTEQ4 [**?**] set of proton PDFs is used.

The programs LEPTO or ARIADNE are used for the QCD corrections so that a complete simulation of the ep-DIS process is made. The first-order QCD effects can be simulated using the exact matrix elements. There are two such processes: the QCD Compton process (QCDC), $V^*q \rightarrow qg$, and the boson-gluon fusion process (BGF), $V^*g \rightarrow q\overline{q}$. For higher-order QCD corrections the two programs use different models :

- LEPTO uses the MEPS (Matrix Element plus Parton Shower) model. In this model, additional parton radiation is generated according to the DGLAP-splitting functions. This corresponds to a leading-log approximation of gluon emission.
- ARIADNE uses the colour dipole model (CDM). This model is based on the idea to treat gluon emission from a $q\overline{q}$ pair as radiation from the colour dipole between de q and the $\overline{q}$. This model incorporates BGF as an extra process, while the QCDC is already included in the colour dipole radiations.

Finally the partons are simulated to fragment into a set of primary hadrons which subsequently may decay further. Both ARIADNE and LEPTO use the Lund String model as implemented in the JETSET [Sj94] program for the simulation of fragmentation.

5.2 Description of Data by the Simulation

Comparisons of event distributions between data and Monte Carlo generated samples are shown. In general, the Monte Carlo generated events should describe the data and if it significantly fails to do so, the correction for detector effects might be miscalculated. It is shown that the MC samples describe the data well enough to keep the systematic uncertainties below the statistical uncertainties of the data. This agreement allows for a bin-by-bin correction, which will be discussed in the next chapter, to be applied.

Particularly important is the Monte Carlo description of the data for the quantities used in the event selection and for the determination of the kinematics. Therefore, is put on the comparisons of the calorimeter and tracking quantities.

Various data distributions are compared with the simulations in the following plots. The points (back dots) are the data measured with the ZEUS detector, the solid lines are the predictions of ARIADNE and the dashed lines are the predictions of MEPS.

The distributions of the kinematic variables Q^2, x and y reconstructed with the Jacquet-Blondel Method are shown in figure 5.1. The missing transverse momentum ($\not{p}_t$) measured with the CAL is also shown. The agreement between data and both Monte Carlo samples is reasonable.

Distributions of calorimenter quantities are shown in figure 5.2: the ratio of the missing transverse momentum over the total transverse energy ($\not{p}_t/E_t$), the ratio of the missing transverse momentum excluding the first ring of the FCAL over the missing transverse momentum ($\not{p}_t^{-1r}/\not{p}_t$), and the ratio of the transverse energy of the calorimeter cell with highest transverse energy over the total transverse energy (E_t^{max}/E_t^{cal}). The distribution of $E-P_z$ is shown. The tranverse energy flow measured by the calorimeter is well described by both Monte Carlo samples.

The distributions of the tracking quantities measured with the CTD and used in the data selection are presented in figure 5.3 . The description of the tracking variables in the data are reasonably by both MC samples is reasonable.

The distributions of the transverse energy (E_T^{jet}) and pseudorapidity (η^{jet}) of the jets reconstructed with the calorimeter are shown in figure 5.4 . The description of the jet variables in the data by both MC samples is reasonable.

It is concluded that for both Monte Carlo samples, ARIADNE and MEPS, the agreement between data and MC is satisfactory. These Mc samples are used to correct the data to hadron level (see sections 6.2).

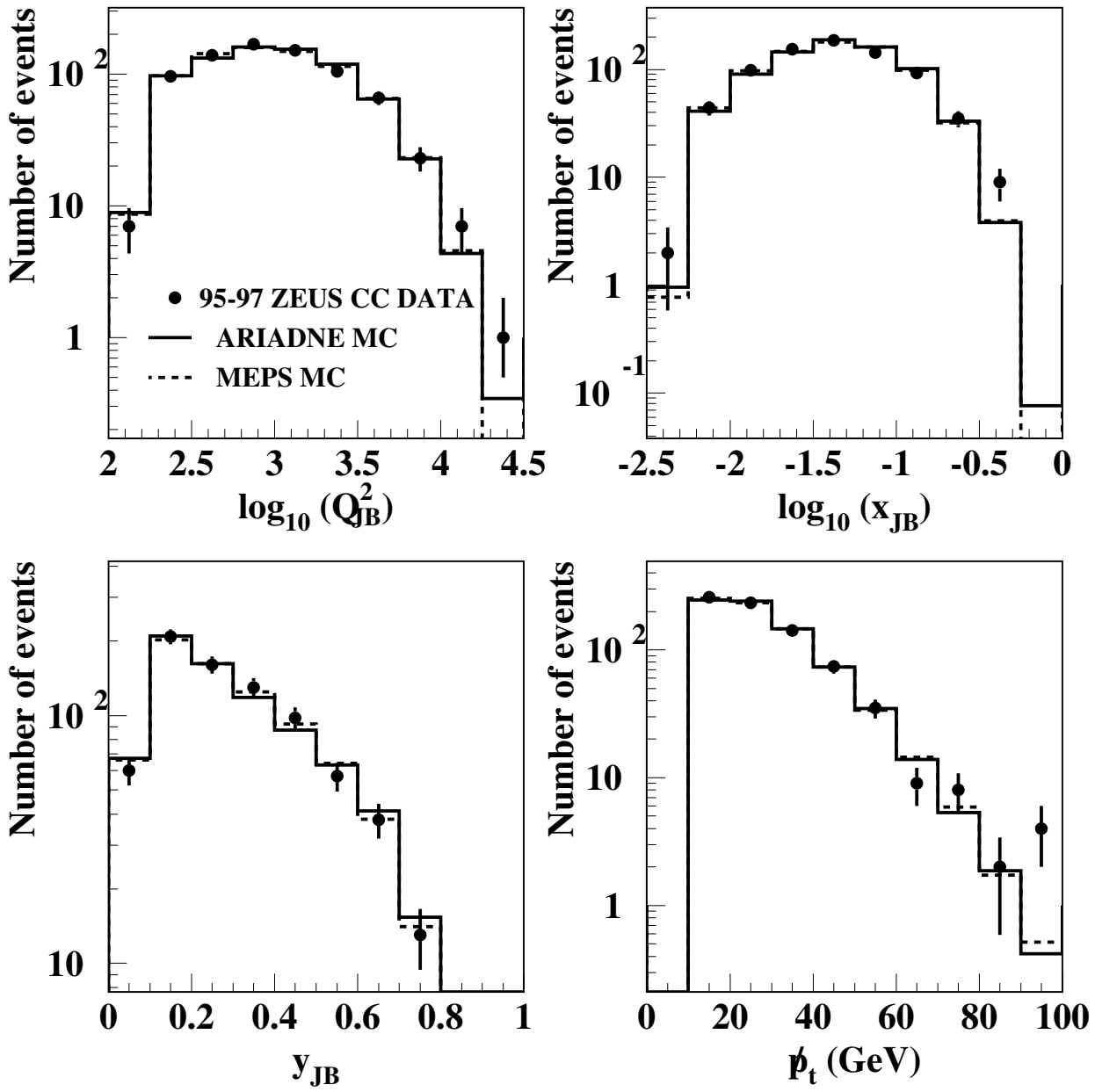

Figure 5.1 - Distributions of the kinematic variables Q^2, x and y reconstructed with the Jacquet-Blondel Method. The transverse momentum (p_t) measured with the CAL is also shown. The points are the ZEUS data and the solid(dashed) lines represent the ARIADNE(MEPS) Monte Carlo simulations. The Monte Carlo predictions are normalised to the data points.

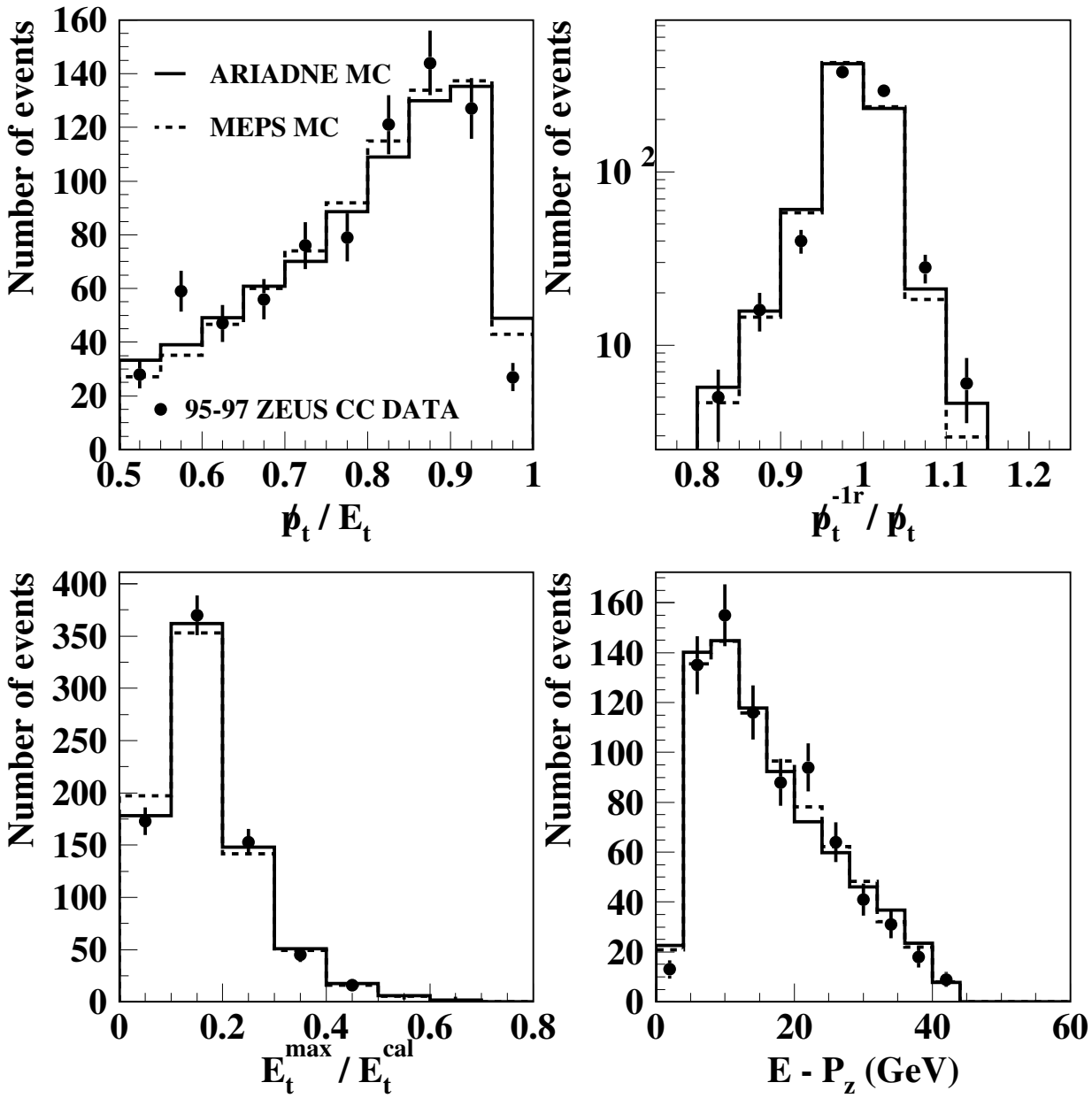

Figure 5.2 - Distributions of calorimeter quantities: the ratio of the total transverse momentum over the total transverse energy ($\not{p}_t/E_t$), the ratio of the total transverse momentum excluding the first ring of the FCAL over the total transverse momentum ($\not{p}_t^{-1r}/\not{p}_t$) and the ratio of the transverse energy of the calorimeter cell with highest transverse energy over the total transverse energy (E_t^{max}/E_t^{cal}). The distribution of the $E - P_z$ measured with the CAL is also shown. The points are the ZEUS data and the solid (dashed) lines represents the ARIADNE (MEPS) Monte Carlo simulations. The Monte Carlo predictions are normalised to the data points.

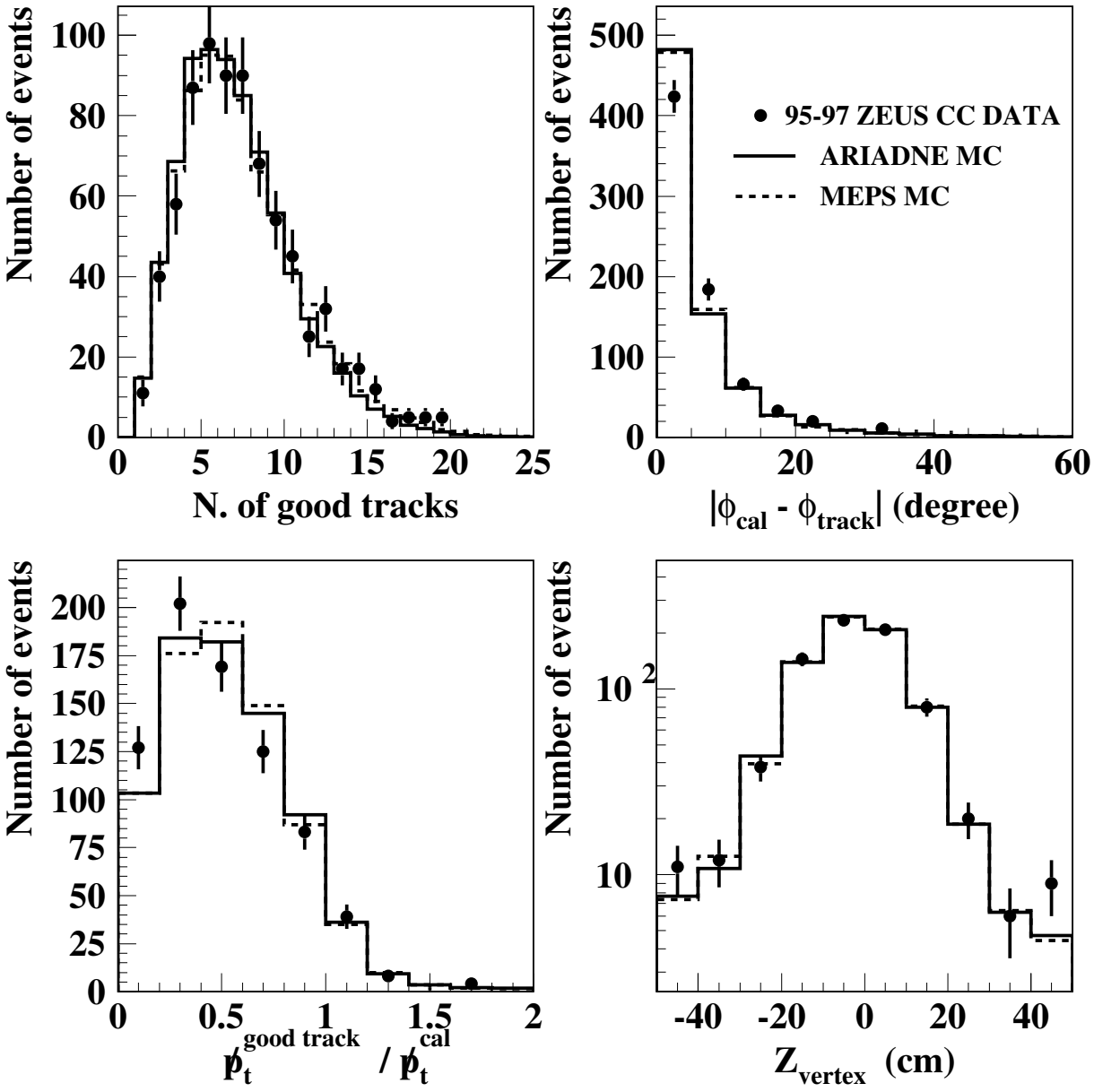

Figure 5.3 - Distributions of tracking quantities measured with the CTD: the number of *good tracks*, the absolute difference between the azimuthal angle of the net momentum calculated with *good tracks* and the azimuthal angle measured by the calorimeter ($|\phi_{cal} - \phi_{track}|$), the ratio of the transverse momentum calculated with *good tracks* and the calorimeter ($\not{p}_t^{\text{good tracks}}/\not{p}_t^{cal}$) and the Z_{vertex} distribution. The points are the ZEUS data and the solid (dashed) lines represents the ARIADNE (MEPS) Monte Carlo simulations. The Monte Carlo predictions are normalised to the data points.

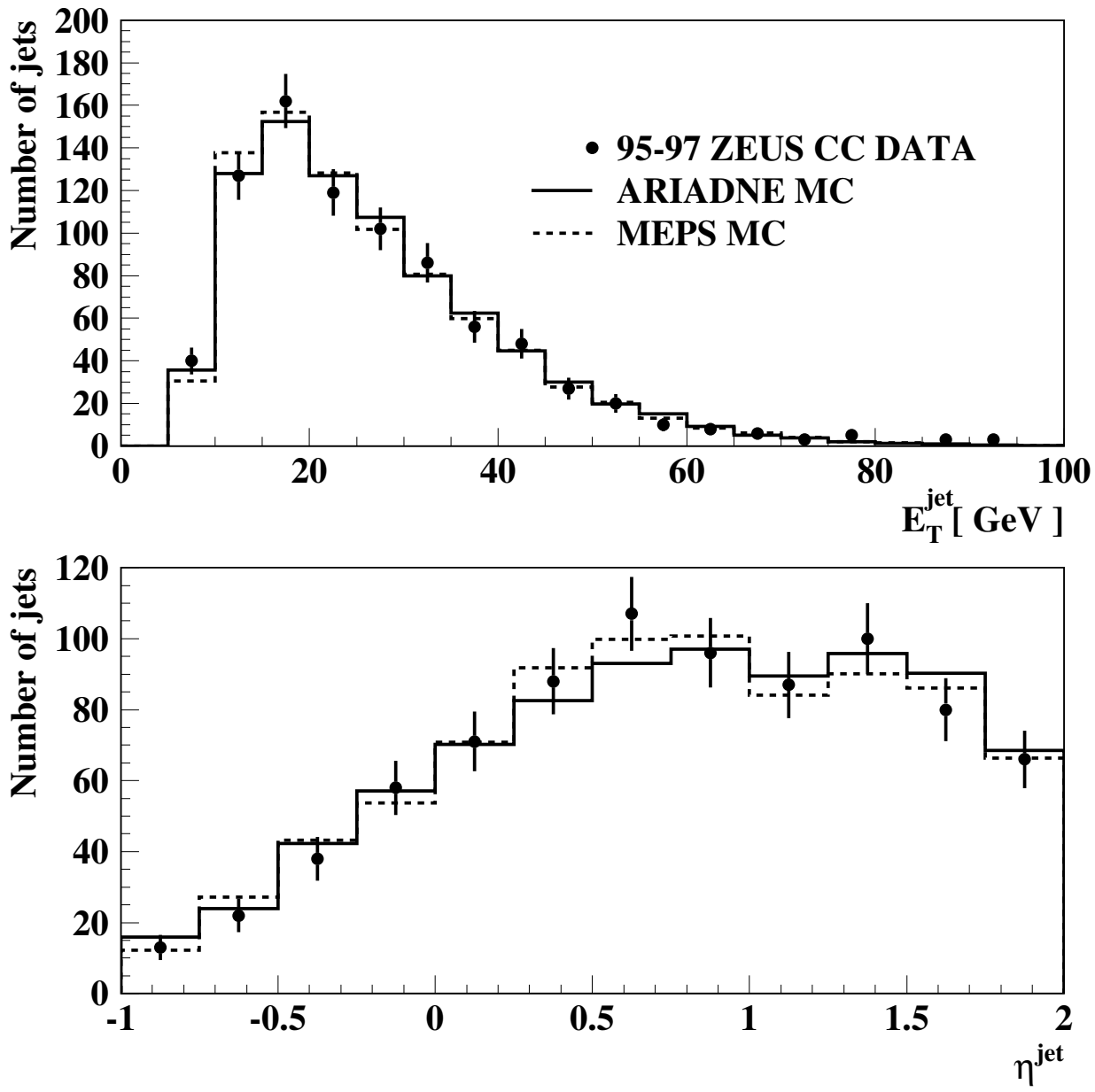

Figure 5.4 - Distributions of the transverse energy (E_T^{jet}) and pseudorapidity (η^{jet}) of the jets reconstructed with the calorimeter. The points are the ZEUS data and the solid (dashed) lines represents the ARIADNE (MEPS) Monte Carlo simulations. The Monte Carlo predictions are normalised to the data points.

Chapter 6

Analysis Method

6.1 Resolution in jet and kinematic variables

The data measured in the ZEUS detector are a convolution of the physical quantities with detector effects. In general, if the true physical quantity has a certain value, the distributions of the measured values displays a shift, called *bias*, and a spread with respect to the true value, called *resolution*. A good measurement should have both a small bias and a small resolution. The evaluation of the systematic uncertainties assigned to the corrected data depends on the resolution of the measurement. The size of the bins of a measured distribution, for example a cross section, are chosen such that they are much larger than the resolution in order to keep the number of events that migrate outside the bin or into the bin low.

The determination of the resolution for a certain quantity X is done using the Monte Carlo simulation since this quantity is known both at the generator level (in our case: hadron level) and at the detector level. In the case of a dimensionful variable the resolution is defined as:

$$\delta_X = \frac{X^{\mathrm{GEN}} - X^{\mathrm{DET}}}{X^{\mathrm{GEN}}} \,, \tag{6.1}$$

where GEN and DET stay for generator level and detector level, respectively. The variable δ_X defined above has a certain distribution. Its mean value is the bias and the spread is the resolution. For a dimensionless variable, the following definition is more appropriate:

$$\delta_X = X^{\mathrm{GEN}} - X^{\mathrm{DET}} \,. \tag{6.2}$$

In both cases, the resolution δ_X is a dimensionless variable. The study of the resolution for some measured quantities is discussed in what follows.

6.1.1 Jet Energy Correction

A jet measured in the calorimeter has a transverse energy that differs from that of the hadron level. A jet measured in the calorimeter usually has a smaller transverse energy $E_T^{cal}(jet)$ than the "true" value $E_T^{had}(jet)$ of the set of hadrons. This energy loss is due to dead material in front of the calorimeter and particles which do not deposit a significant amount of energy in the main calorimeter, such as muons and neutrinos. The transverse jet energy as measured with the UCAL needs therefore to be corrected. By correcting for the bias an improvement of the purities and efficiencies is achieved. The ARIADNE Monte Carlo sample was used for calculating the energy correction. In order to compare jets at the detector (cal) and hadron (had) level, definite ranges in η^{jet} and thresholds in E_t^{jet} have to be considered. The following ranges were used:

$$\begin{aligned} E_T^{cal}\,(jet) \;&\geq\; 6\ \text{GeV} \quad ; \quad -1 \;\leq\; \eta^{cal}\,(jet) \leq 2 \\ E_T^{had}\,(jet) \;&\geq\; 8\ \text{GeV} \quad ; \quad -1 \;\leq\; \eta^{had}\,(jet) \leq 2 \end{aligned}$$

A matching of the hadron and calorimeter jets was done. For each hadron jet the distance in the $\eta - \phi$ plane between that jet and each calorimeter jet is computed as:

$$d(had - cal) = \sqrt{(\,\eta^{had}\,(jet) - \eta^{cal}\,(jet))^2 + (\phi^{had}\,(jet) - \phi^{cal}\,(jet)\,)^2} \qquad (6.3)$$

The pair with the minimum $d(had - cal)$ is taken, provided this distance itself is smaller than 1 unit. The jet variables for this hadron-calorimeter pair of jets are then compared and used to estimate the biases and resolutions.

The distributions of $\delta_{E_T(jet)}$, $\delta_{\eta(jet)}$ and $\delta_{\phi(jet)}$ in the ARIADNE MC sample are shown in figure 6.1. The resolution in E_T^{jet} is about 12% and the bias is 13%. For the η^{jet} and ϕ^{jet} variables there is no bias. The resolution in η^{jet} is about 0.04 units and in the case of ϕ^{jet} is 2.3 degrees.

The energy correction has been constructed as:

$$\left(E_T^{jet}\right)_{corrected} = C_1(E_T^{cal}, \eta_{jet}) \;+\; C_2(E_T^{cal}, \eta_{jet}) \;\cdot\; E_T^{cal} \qquad (6.4)$$

The mean transverse energy of the jets at CAL level, $< E_T^{cal}(jet) >$, as function of the transverse energy at hadron level, $E_T^{had}(jet)$, is shown in figure 6.2 for 12 different bins in η^{jet}. The correction energy correction was determined by a linear fit of the form:

$$< E_T^{cal}(jet) > = P_0 \;+\; P_1 \;\cdot\; E_T^{had}(jet)\,. \qquad (6.5)$$

The parameters C_1 and C_2 of equation 6.4 are then determined in each η^{jet} bin as follows:

$$C_1 \;=\; -\,\frac{P_0}{P_1} \;\;,\;\; C_2 \;=\; \frac{1}{P_1} \qquad (6.6)$$

As can be seen from figure 6.2, the linear fits with the above function (see equation 6.5) describe reasonably well the results. The fact that the parameters depend on η_{jet}^{cal} is due to the fact that the distribution of the dead material varies with the

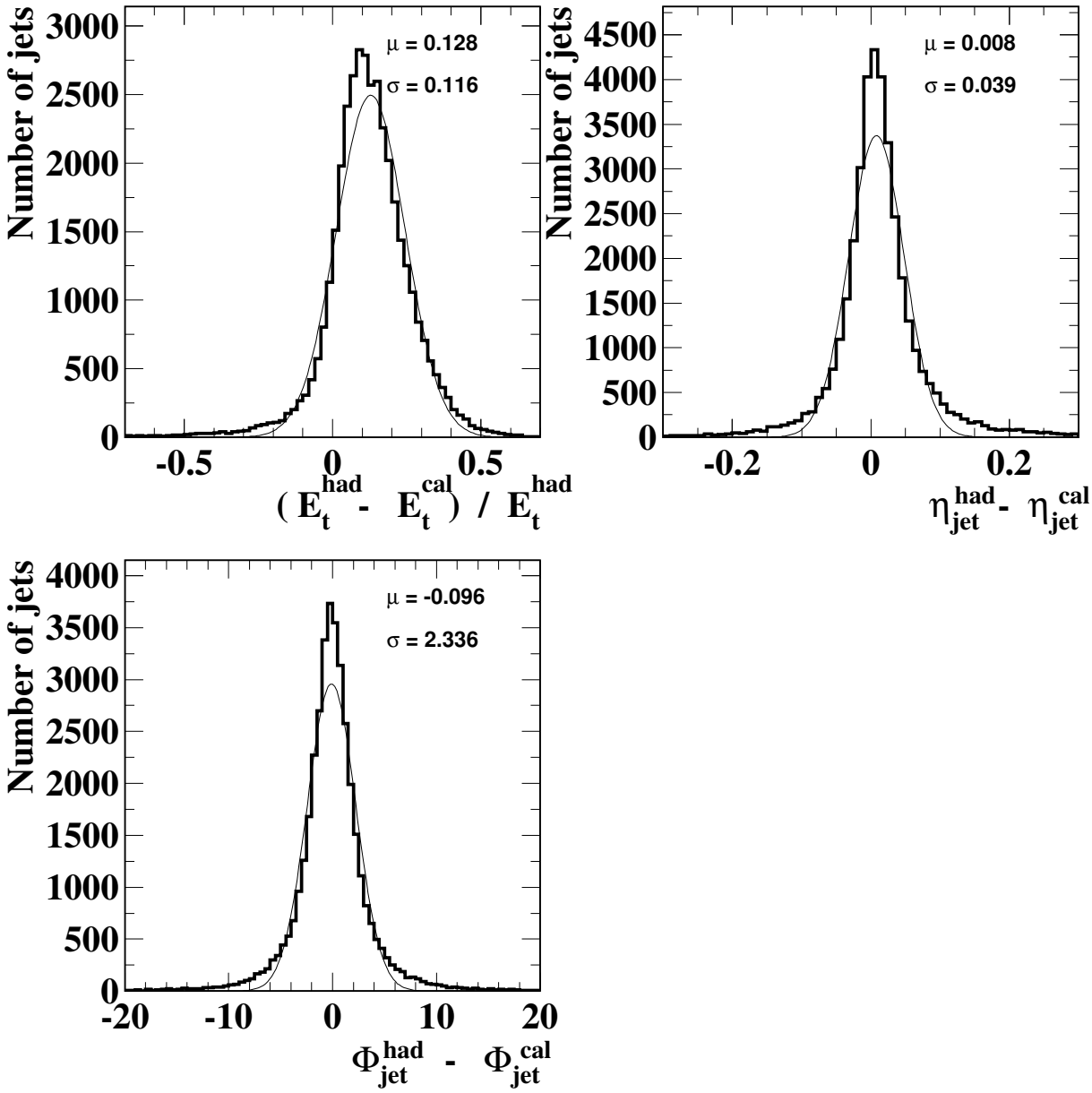

Figure 6.1 - The distributions of $(E_T^{had} - E_T^{cal})/E_T^{cal}$, $\eta_{jet}^{had} - \eta_{jet}^{cal}$ and $\phi_{jet}^{had} - \phi_{jet}^{cal}$ using the ARIADNE MC sample.

pseudorapidity η. This dependence of the correction factors on η^{jet} is shown in figure 6.3: the mean value of $E_T^{had}(jet) - E_T^{cal}(jet)/E_T^{cal}(jet)$ as a function of η_{jet} (upper-left) and ϕ_{jet} (upper-right) has been considered. The former shows two peaks, one at $\eta^{jet} \approx 1.1$ and another at $\eta^{jet} \approx -1$ which are understood in terms of the increase in dead material in front of the calorimeter in those two regions. The azimuthal angle ϕ^{jet} dependence is pretty much constant. For this reason the above parametrization was made η^{jet} dependent only.

After applying the above correction to the jet transverse energy, the bias in $E_T^{corr}(jet)$ is reduced to less than 2%, as shown in figure 6.3.

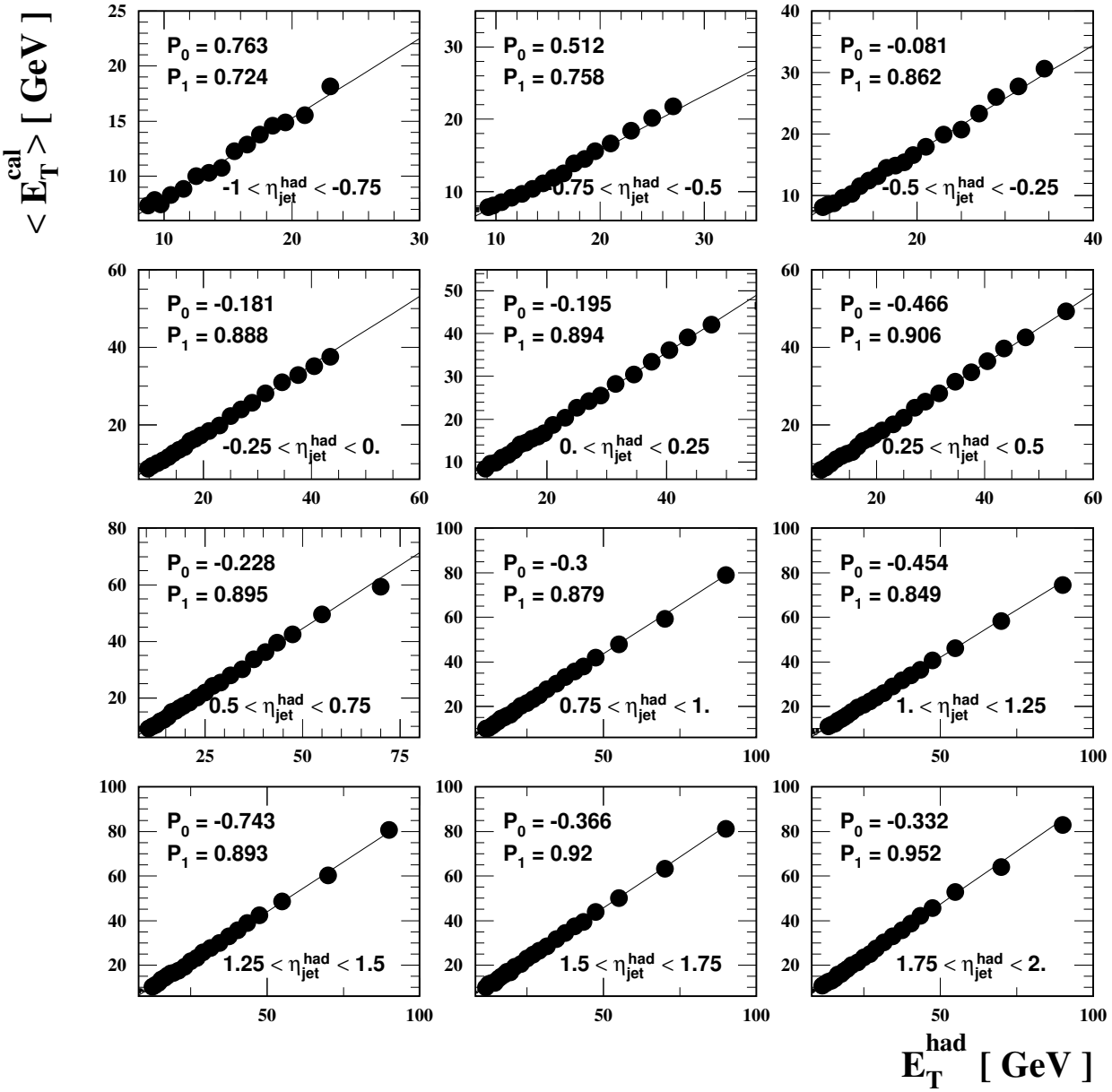

Figure 6.2 - The mean value $< E_T^{cal}(jet) >$ as a function of $E_T^{had}(jet)$ in different η^{jet} bins. The fits with the functional form $P_0 + P_1 \cdot < E_T^{cal} >$ as well as the values of the parameters are also shown.

6.1.2 Correction of the Kinematic Variables

Due to energy losses in the calorimeter both $\not{p}_t$ and $E - P_z$ reconstructed with the UCAL underestimate the true values; these biases produce a shift in the measured value of Q^2_{JB} with respect to the true value. The detector simulation was used to determine corrected values of the kinematic, Q^2_{corr} and y_{corr}. In the previous section it was shown that the resolution in the pseudorapidity of the jets is very good. Therefore, the correction for the kinematic variables has also been made in bins of

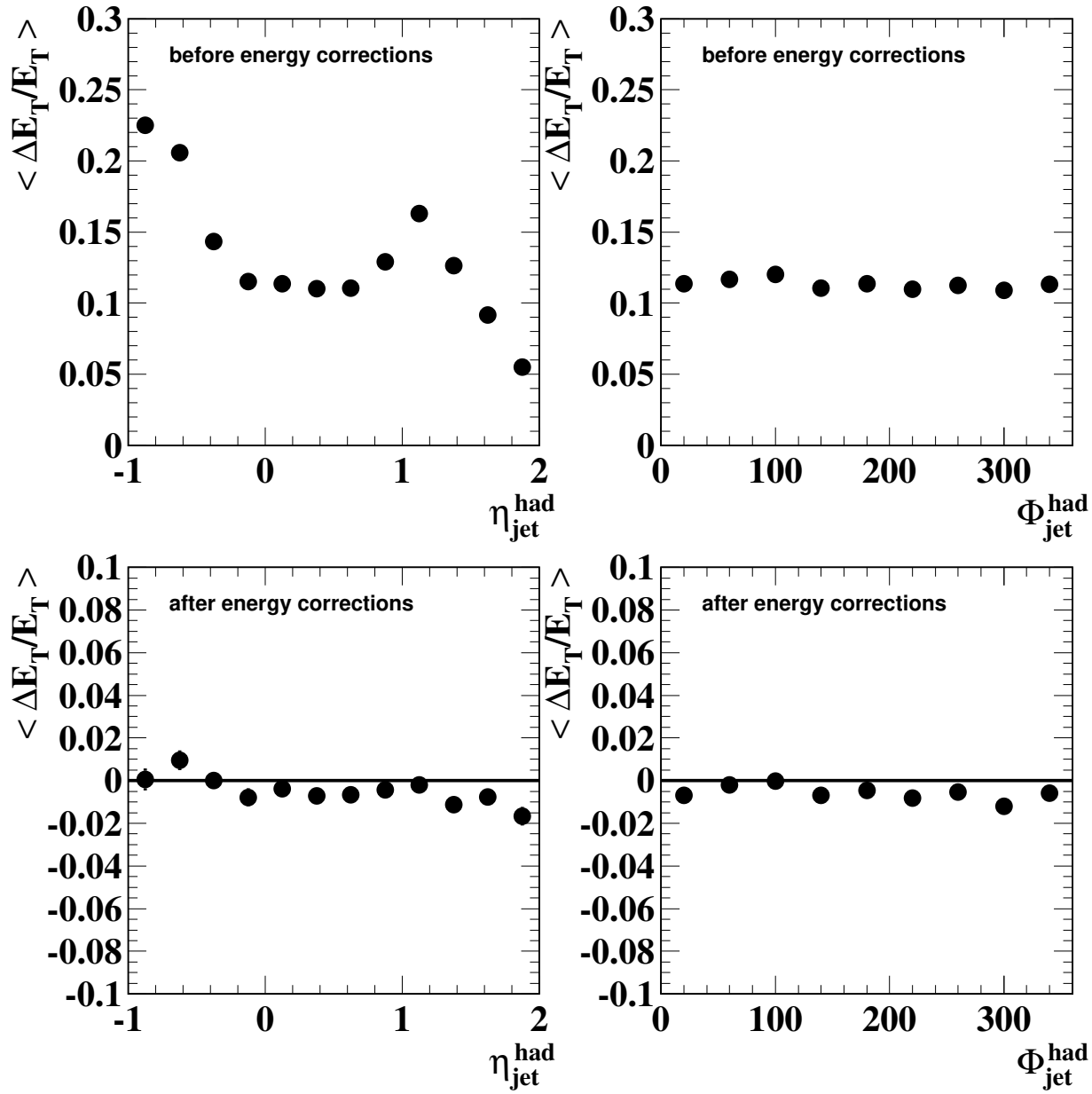

Figure 6.3 - The mean value $< E_T^{had} - E_T^{cal}/E_T^{cal} >$ as a function of η_{jet} (left) and ϕ_{jet} (right) before (top) and after (bottom) jet transverse energy corrections are applied. The ARIADNE MC sample has been used.

the pseudorapidity of the jet with highest E_T^{jet} in the event. In the case of CC DIS, events with only one jet are predominant and, in this case, the value of η_{jet} is closely related to the angle of the hadronic system, γ_h.

The distribution of $(Q^2_{TRUE} - Q^2_{JB})/Q^2_{TRUE}$ and the mean value $< (Q^2_{TRUE} - Q^2_{JB})/Q^2_{TRUE} >$ as a function of η_{jet}^{had} are shown in figure 6.4 before and after energy corrections. The resolution in Q^2 is about 21% and the bias is 31%. The dependence of $< (Q^2_{TRUE} - Q^2_{JB})/Q^2_{TRUE} >$ on η_{jet} can be understood in terms of the distribution of the dead material in the central calorimeter.

The logarithm of the mean Q^2 reconstructed in the calorimeter using the Jacquet-Blondel method, $\log < Q^2_{JB} >$, as a function of $\log Q^2_{TRUE}$ is shown in figure 6.5 for 12 different bins in η^{jet} . The correction to Q^2_{JB} was determined by a linear fit of the form:

$$\log < Q^2_{JB} > = P_0 + P_1 \cdot \log Q^2_{TRUE} . \tag{6.7}$$

The corrected value of Q^2 was determined as follows:

$$\log (Q^2)_{corrected} = \frac{\log < Q^2_{JB} > - P_0}{P_1} \tag{6.8}$$

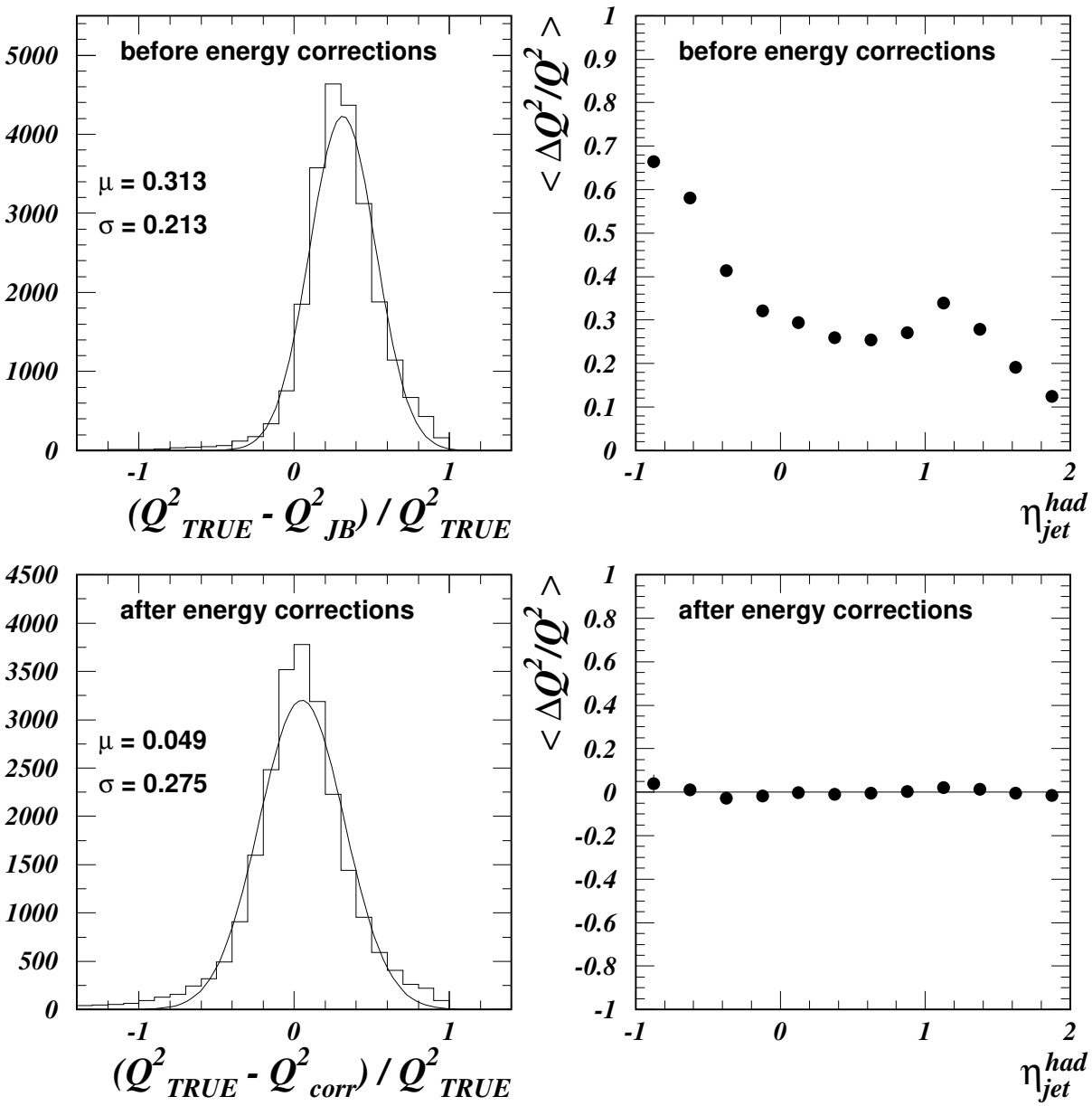

Figure 6.4 - The distribution of $(Q^2_{TRUE} - Q^2_{JB})/Q^2_{TRUE}$ (left) and the mean value $< (Q^2_{TRUE} - Q^2_{JB})/Q^2_{TRUE} >$ as a function of η^{had}_{jet} before (top) and after (bottom) energy corrections are applied.

After corrections the bias in Q^2_{corr} is reduced to less than 5% (see figure 6.4).

The energy losses also produce a bias in the reconstructed value of y_{JB} using the calorimeter. The distribution of $(y_{TRUE} - y_{JB})/y_{TRUE}$ is shown in figure 6.6 before and after the energy corrections are applied. The resolution in y is about 11% and the bias is 12%. In a similar way as for Q^2_{JB} a correction factor has been determined for y_{JB} in bins of the pseudorapidity of the jet with highest E_t^{jet} in the event.

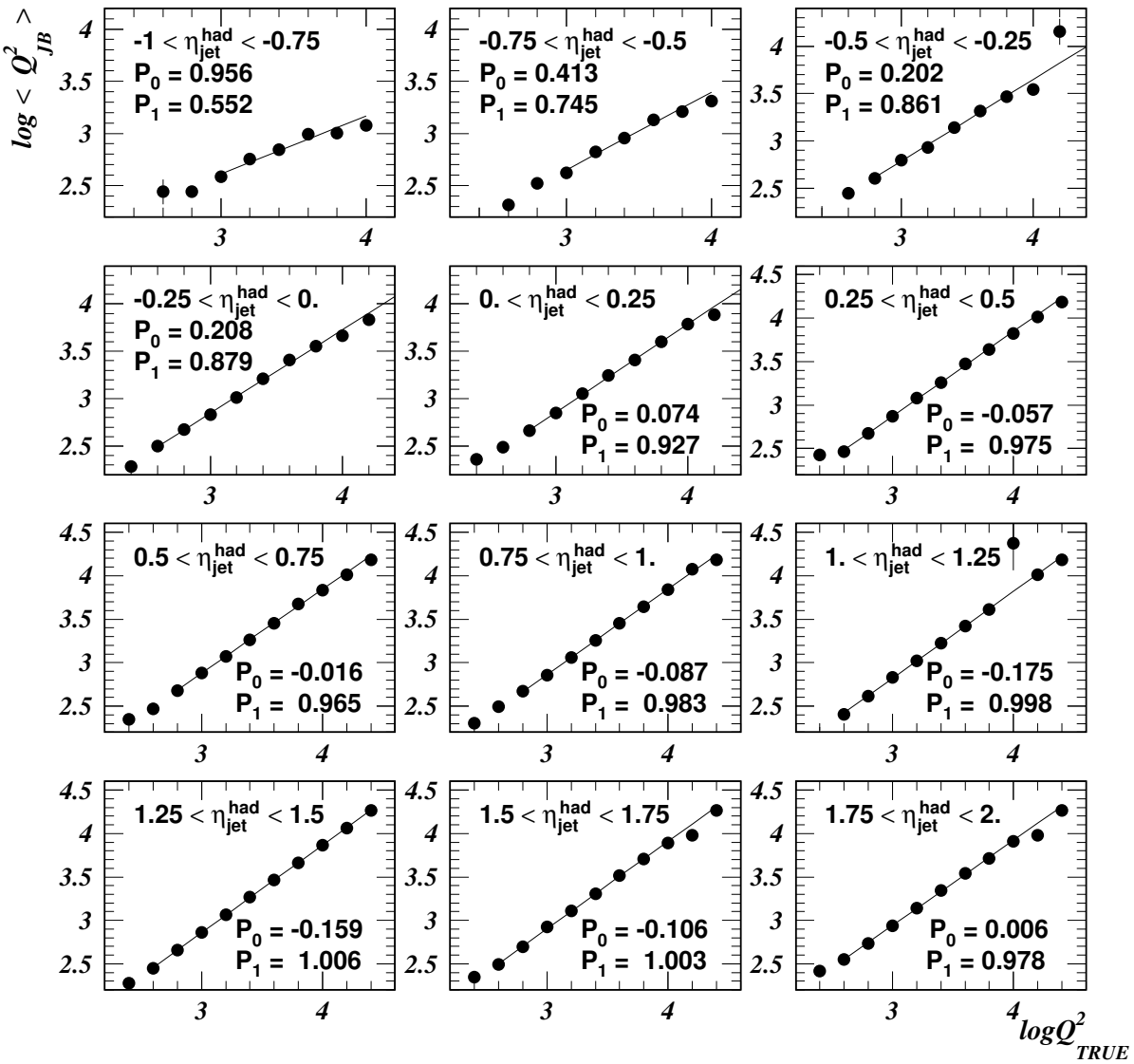

Figure 6.5 - The value of $\log < Q^2_{JB} >$ as a function of $\log Q^2_{TRUE}$ in different η^{jet} bins. The fits with the functional form $P_0 + P_1 \cdot \log Q^2_{TRUE}$ as well as the values of the parameters are shown.

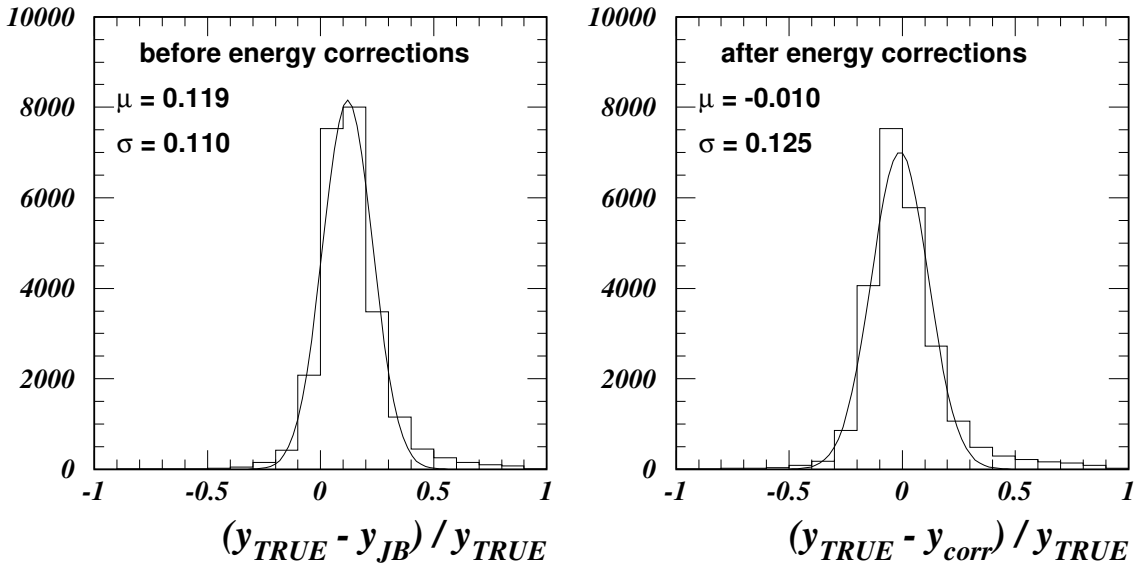

Figure 6.6 - The distribution of $(y_{TRUE} - y_{JB})/y_{TRUE}$ before (left) and after (right) energy corrections are applied.

6.2 Correction of measured distributions

The various observables measured in this analysis are obtained from the ZEUS data at the calorimeter level. The hadron level results are determined by correcting

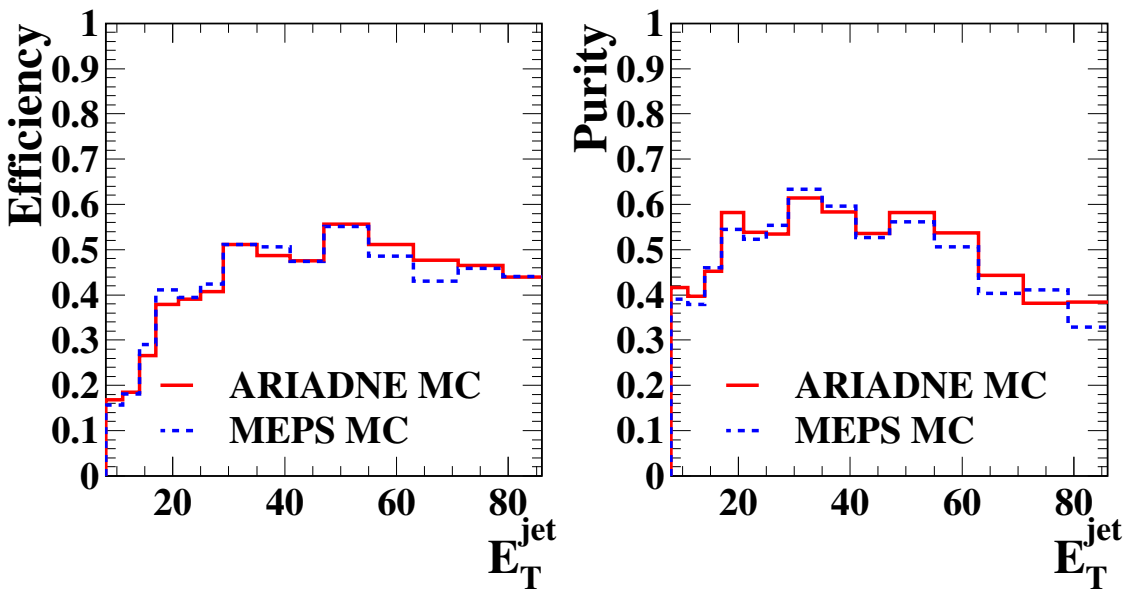

Figure 6.7 - Efficiency (left) and Purity (right) of the E_T^{jet} distribution in inclusive jet CC DIS. The ARIADNE (solid lines) and MEPS (dashed lines) MC samples have been used.

for detector effects. The correction factors are calculated using the Monte Carlo simulations.

6.2.1 Determinatin of of cross sections

A *bin-by-bin correction* method has been used in this analysis. In this method, the number of data events in each bin of a given distribution is counted (at the detector level) as well as the number of Monte Carlo events in that bin at both detector and hadron levels. The efficiency in bin i $\mathcal{E}_i$ is defined as:

$$\mathcal{E}_i \equiv \frac{N_i^{GEN\&DET}}{N_i^{GEN}} \ , \tag{6.9}$$

where N_i^{GEN} is the number of generated events in that bin and $N_i^{GEN\&DET}$ is the number of events generated and reconstructed in that bin. The efficiency displays the fraction of the generated events that "remain" in the bin. Another important quantity is the purity in bin i $\mathcal{P}_i$ that is defined:

$$\mathcal{P}_i \equiv \frac{N_i^{GEN\&DET}}{N_i^{DET}} \ , \tag{6.10}$$

where N_i^{DET} is the number of Monte Carlo events reconstructed in bin i . The purity shows quantifies the fraction of events reconstructed in bin i that were indeed generated in that bin.

The efficiency and purity of the E_T^{jet} distribution in inclusive jet CC DIS is shown in figure 6.7. The efficiency is about 50% and the purity is about 60%.

The efficiency and purity of the measurement of the η^{jet} distribution in inclusive jet CC DIS events is shown in figure 6.8. There is no dependence of the purity with the pseudorapidity of the jet and the efficiency drops for jets in the backward region. The efficiency is about 70% and the purity is about 90%.

The number of data events N_i^{DAT} in bin i of a given distribution is corrected to the hadron level by multiplying with a correction factor as follows:

$$N_i^{COR} \ = \ N_i^{DAT} \cdot C_i^{MC} \tag{6.11}$$

The correction factor C_i^{MC} is calculated from the MC samples as follows:

$$C_i^{MC} \ = \ \frac{\mathcal{P}_i}{\mathcal{E}_i} \ = \ \frac{N_i^{GEN}}{N_i^{DET}} \tag{6.12}$$

The cross section in each bin is determined as the ratio of the corrected number of events in bin i with the integrated luminosity. The statistical uncertainty of the corrected number of events is calculated using standard error propagation methods. The data and the correction factor C_i^{MC} are independent of each another. The statistical uncertainty of the data is calculated as the square root of the number of events:

$$\left(\frac{\sigma_i^{COR}}{N_i^{COR}}\right)^2 = \left(\frac{\sqrt{(N_i^{DAT})}}{N_i^{DAT}}\right)^2 + \left(\frac{\sigma_{C_i^{MC}}}{C_i^{MC}}\right)^2 \tag{6.13}$$

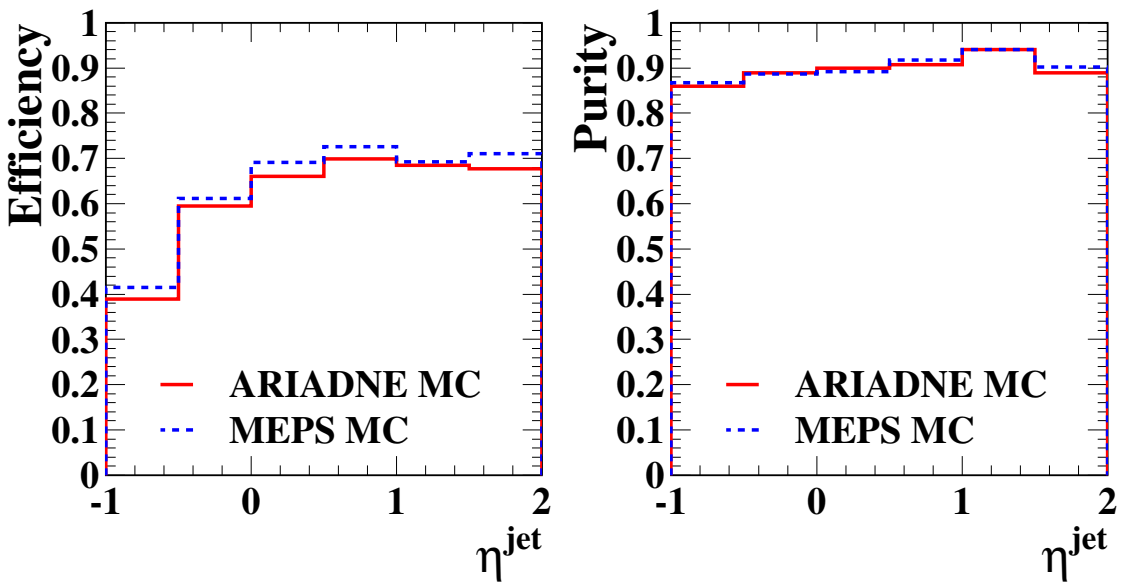

Figure 6.8 - Efficiency (left) and Purity (right) of the η^{jet} distribution in inclusive jet CC DIS. The ARIADNE (solid lines) and MEPS (dashed lines) MC samples have been used.

It is not possible to calculate the uncertainty of the correction factor directly from the formula 6.12 because the number of generated (N_i^{GEN}) and reconstructed (N_i^{DET}) not independent[1]. To apply error propagation the following quantities are defined for each bin:

$$\begin{aligned} A1 &= N(GEN \ \& \ DET) = N^{GEN\&DET} \\ A2 &= N(GEN \ \& \ \overline{DET}) \\ A3 &= N(\overline{GEN} \ \& \ DET) \end{aligned} \tag{6.14}$$

$\overline{DET}$ is the set of events not reconstructed in this bin and $\overline{GEN}$ is the set of events not generated in this bin. The three numbers above are independent of each other and, their respective statistical uncertainties can be calculated using Poisson statistics. The following relations are true:

$$\begin{aligned} N_i^{GEN} &= A1_i + A2_i \\ N_i^{DET} &= A1_i + A3_i \\ C_i^{MC} &= \frac{A1_i + A2_i}{A1_i + A3_i} \end{aligned} \tag{6.15}$$

The statistical uncertainties of the correction can be calculated from the above relations using error propagation:

$$\left(\frac{\sigma_{C_i^{MC}}}{C_i^{MC}}\right)^2 = \left(\frac{\partial C_i^{MC}}{\partial A1_i} \cdot \frac{\sigma_{A1_i}}{A1_i}\right)^2 + \left(\frac{\partial C_i^{MC}}{\partial A2_i} \cdot \frac{\sigma_{A2_i}}{A2_i}\right)^2 + \left(\frac{\partial C_i^{MC}}{\partial A3_i} \cdot \frac{\sigma_{A3_i}}{A3_i}\right)^2 \tag{6.16}$$

[1] In the case of an ideal detector these two sets of events would be exactly the same.

The three partial derivatives and the statistical uncertainties of the quantities $A1$, $A2$, and $A3$ are:

$$\begin{aligned}
\frac{\partial C_i^{MC}}{\partial A1_i} &= \frac{A3_i - A2_i}{(A1_i + A3_i)^2} \quad , \ \sigma_{A1_i} = \sqrt{A1_i} \\
\frac{\partial C_i^{MC}}{\partial A2_i} &= \frac{1}{A1_i + A3_i} \quad , \ \sigma_{A2_i} = \sqrt{A2_i} \\
\frac{\partial C_i^{MC}}{\partial A3_i} &= -\frac{A1_i + A2_i}{(A1_i + A3_i)^2} \quad , \ \sigma_{A3_i} = \sqrt{A3_i}
\end{aligned} \tag{6.17}$$

Using the relations (6.13), (6.14),(6.16) and (6.17), and the statistical uncertainty of the corrected number of events is calculated.

6.2.2 Determination of the corrected distributions in jet internal structure variables

The jet internal structure can be studied in terms of many observables. In this analysis jet shapes and mean subjet multiplicities are considered. The observables reconstructed with the calorimeter are corrected to hadron level using Monte Carlo techniques and with a *bin-by-bin correction* method in a similar way as for the cross-sections. This procedure corrects for acceptance and smearing effects. The corrections factors also take into account the efficiency of the trigger, the selection criteria, the efficiency and purity of the jet reconstruction.

For a given observable $\mathcal{O}$, the corrected observable is obtained as follws:

$$\mathcal{O}_{corr} \ = \ C^{MC} \ \cdot \ \mathcal{O}_{cal} \ , \tag{6.18}$$

where $\mathcal{O}_{cal}$ is the observable as reconstructed with the calorimeter and C^{MC} is the MC correction factor. C^{MC} is calculated as:

$$C^{MC} \ = \ \frac{\mathcal{O}_{had}^{MC}}{\mathcal{O}_{det}^{MC}} \ , \tag{6.19}$$

where $\mathcal{O}_{had}^{MC}$ and $\mathcal{O}_{det}^{MC}$ are the values of the observable at hadron and detector level, respectively.

The corrected value of the observable may depend on the particular Monte Carlo model used. If the Monte Carlo model considered does not describe the data, the bin-by-bin correction method becomes model dependent. In the present case it has been shown that the MC describes the data.

6.3 Study of Systematic Uncertainties

Uncertainties coming from the simulation are in always smaller than the statistical uncertainties of the data. There are other sources of uncertainty in the measurements. It is possible that the measured quantity is systematically mismeasured.

This mismeasurement comes from a non-perfect understanding and simulation of the physics and of detector effects. Studies have been done in order to estimate the size of the systematic uncertainties. One source of uncertainty is the mismeasurement of the variables on which cuts are applied at the detector level. Therefore, the cuts at the calorimeter level are varied by one standard deviation in both directions around the cut value and keeping the hadron level cut fixed. In the ideal case of the Monte Carlo model describing perfectly the data, such a change of a the cut would not affect at all the final result. However, since this is not always true, the variations (if any) in the measured quantities would indicate a possible systematic effect.

A preliminary study has been made by raising the cut in $\not{p}_t$ from 11 GeV to 12 GeV. This produces a variation on the jet cross sections of less than 1% and on the mean subjet multiplicities of less than 1.5%. Other sources of uncertainties are listed below:

- the description of the hadronization corrections in the simulation is model dependent;
- different parametrizations of the proton parton densities.

In order to evaluate the systematic uncertainty on the modelling of the hadronization process, the corrections with ARIADNE and LEPTO-MEPS have been compared. This variation is typically $\sim 5\%$ for the inclusive jet cross sections, $\sim 15\%$ for the dijet cross sections and less than 2.4% for the mean subjet multiplicity.

To study the dependence with the parametrizations of the parton density , MRSA set of PDFs were used instead of the CTEQ4 set in the Monte Carlo programs. The variation of the measured cross sections is typically $\sim$ 1%. The systematic uncertainties discussed above are uncorrelated and, therefore, in evaluating the total systematic uncertainty they have been added in quadrature.

There are sources of systematic errors which are correlated, since they affect simultaneously all the measurements. The most important ones are:

- the integrated luminosity is measured with an uncertainty of 1.6% ;
- the energy scale of the calorimeter is known with an uncertainty of $\pm 3\%$.

The luminosity uncertainty gives rise to an overall normalisation uncertainty of 1.6% in the measurement of cross sections which is not included in the plots.

The uncertainty on the absolute energy scale of the jets and the energy measured in the CAL ($\pm 3\%$) was estimated by varying E_T^{jet} and the variables measured with the CAL ($\not{p}_t$, E_T) separately. The variation is typically $^{+(2-7)}_{-(5-12)}$% for the cross section measurements and $^{+2.8}_{-1.5}$% for the mean subjet multiplicity. All the correlated systematic uncertainties are added in quadrature and are shown as shaded band in the plots.

The ratio $(\mathcal{O}^* - \mathcal{O})/\mathcal{O}$ is shown for each source of systematic in figures 6.9 to 6.13 : $\mathcal{O}$ is the measured observable with the standard method and $\mathcal{O}^*$ is the value of the observable obtained upon variation of one of the aspects of the method. The shaded

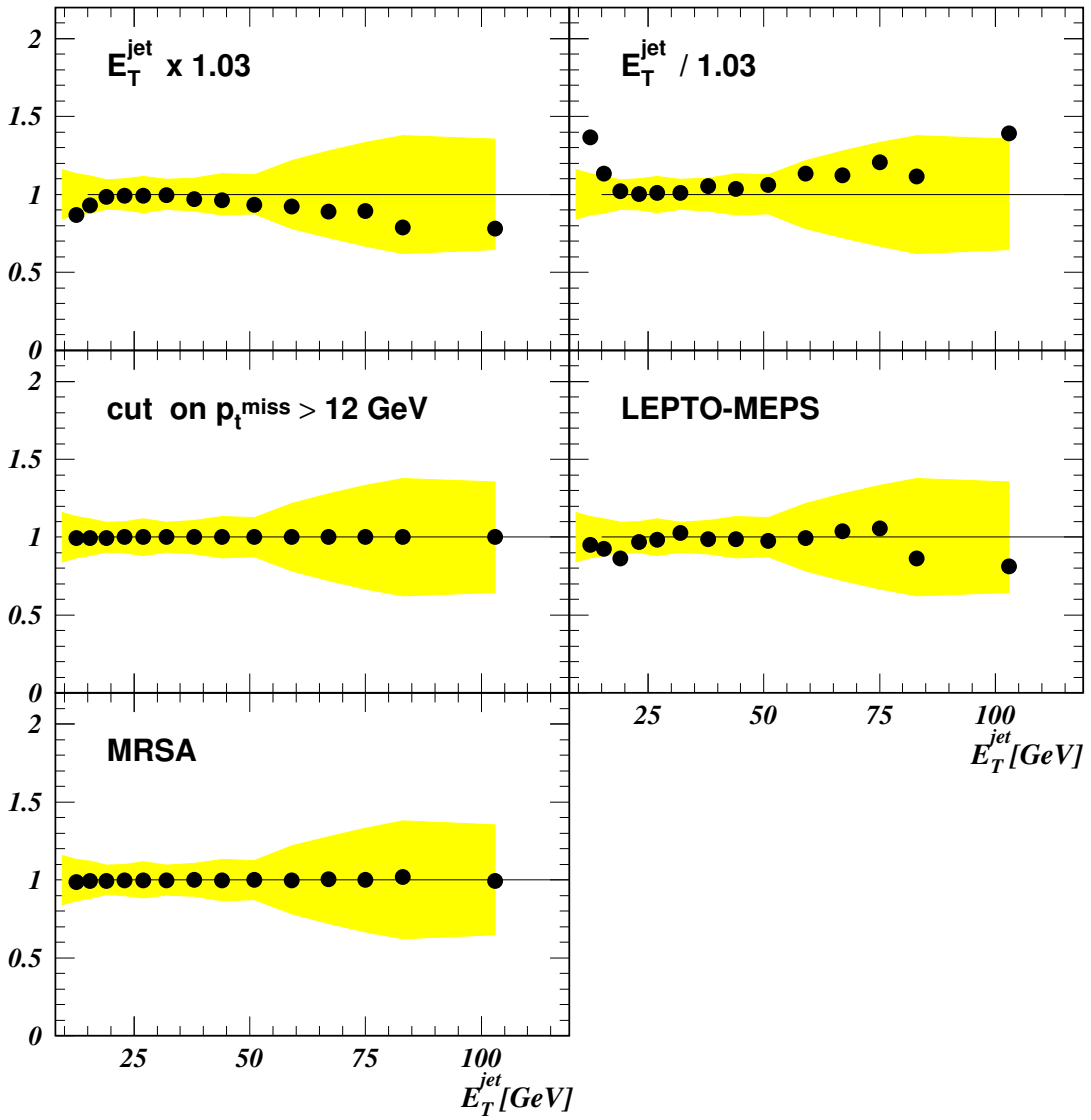

Figure 6.9 - Systematic uncertainties of the measured inclusive jet cross section as a function of E_T^{jet}. The shaded band shows the statistical uncertainty of the data. a) the transverse energy of the jets, E_T^{jet}, is varied by $\pm 3\%$ b) the cut $\not{p}_t$ is raised from 11 to 12 GeV c) The Monte Carlo LEPTO-MEPS is used instead of ARIADNE-CDM to correct the data to hadron level d) The MRSA set of proton PDFs is used instead of the CTEQ4 set.

band in these figures show the statistical uncertainty of the data. In all the observables considered here, the correlated and uncorrelated systematic uncertainties are smaller than statistical uncertainty.

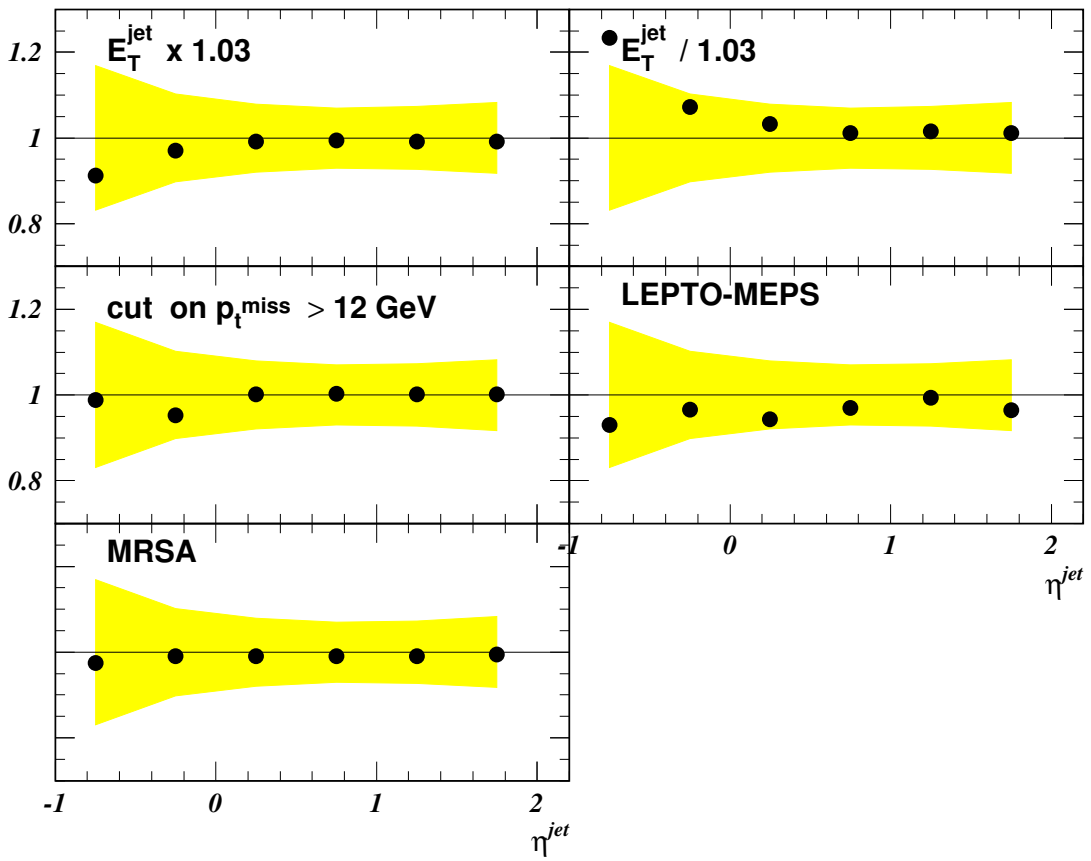

Figure 6.10 - ystematic uncertainties of the measured inclusive jet cross section as a function of η^{jet}. The shaded band shows the statistical uncertainty of the data. a) the transverse energy of the jets, E_T^{jet}, is varied by $\pm 3\%$ b) the cut $\not{p}_t$ is raised from 11 to 12 GeV c) The Monte Carlo LEPTO-MEPS is used instead of ARIADNE-CDM to correct the data to hadron level d) The MRSA set of proton PDFs is used instead of the CTEQ4 set.

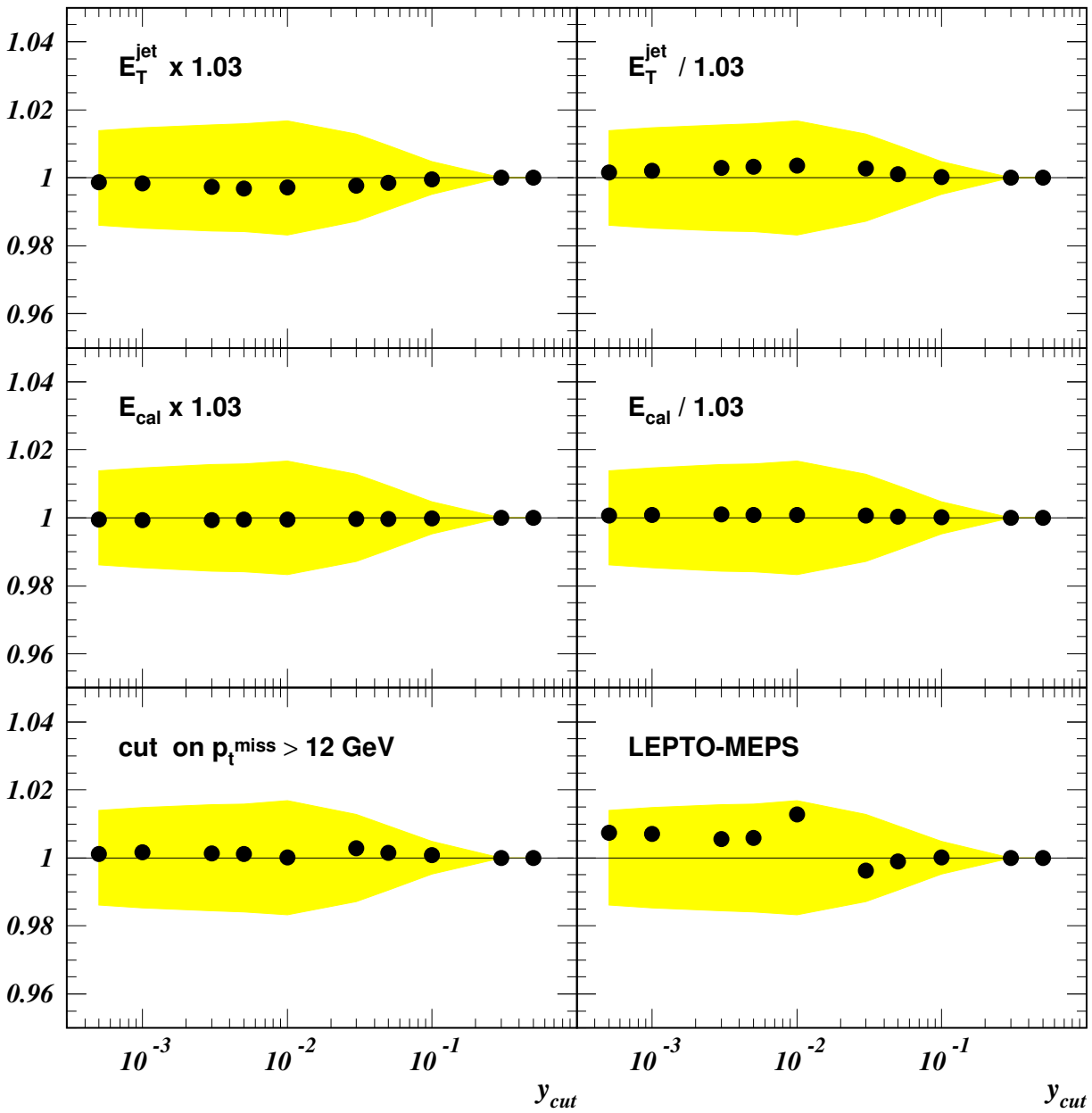

Figure 6.11 - Systematic uncertainties of the measured mean subjet multiplicity as a function of y_{cut}. The shaded band shows the statistical uncertainty of the data. a) the transverse energy of the jets, E_T^{jet}, is varied by $\pm 3\%$ b) the energy in the CAL is varied by $\pm 3\%$ c) the cut $\not{p}_t$ is raised from 11 to 12 GeV d) The Monte Carlo LEPTO-MEPS is used instead of ARIADNE-CDM to correct the data to hadron level.

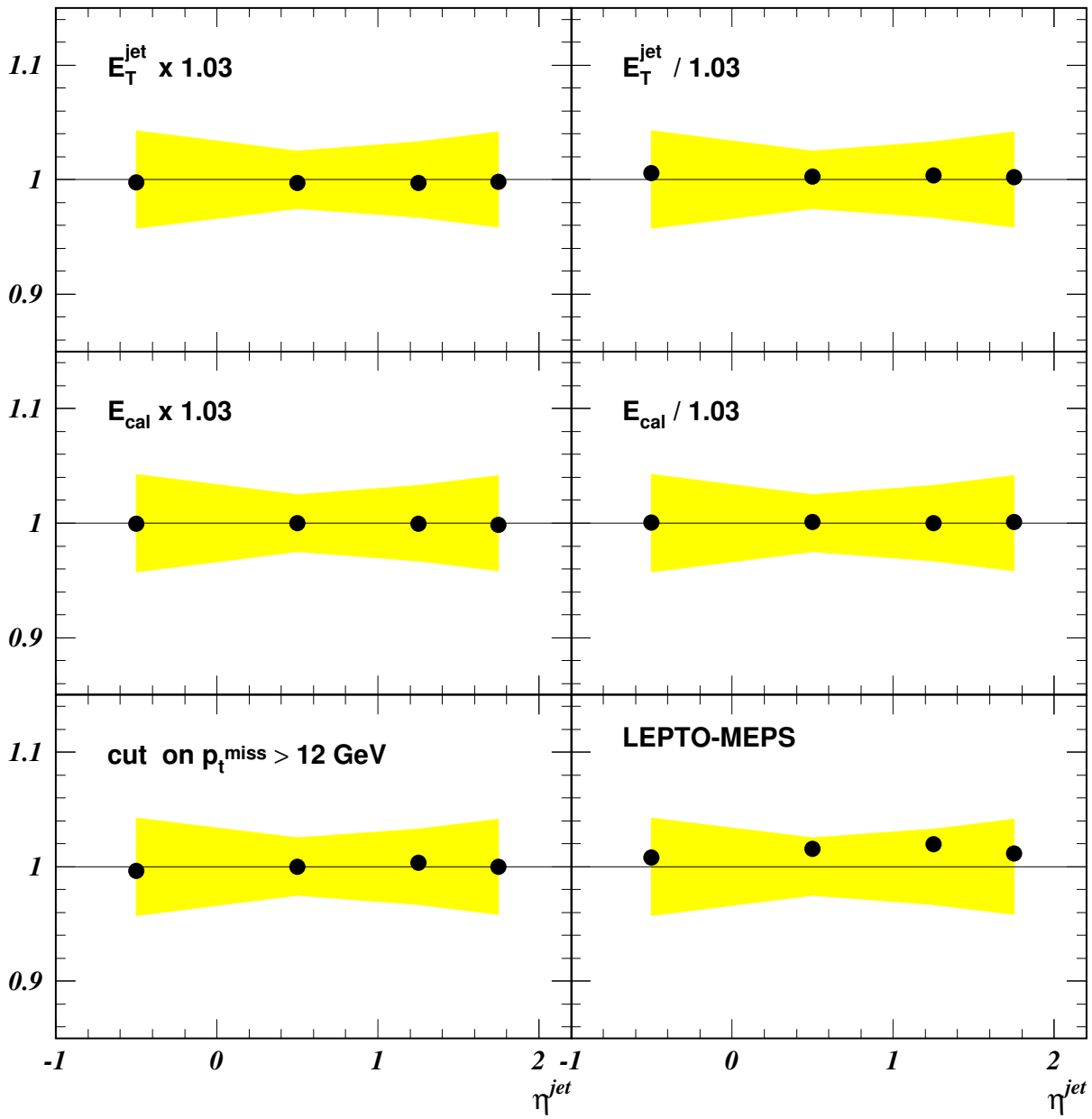

Figure 6.12 - Systematic uncertainties of the measured mean subjet multiplicity as a function of η^{jet}. The shaded band shows the statistical uncertainty of the data.a) the transverse energy of the jets, E_T^{jet}, is varied by $\pm 3\%$ b) the energy in the CAL is varied by $\pm 3\%$ c) the cut $\not{p}_t$ is raised from 11 to 12 GeV d) The Monte Carlo LEPTO-MEPS is used instead of ARIADNE-CDM to correct the data to hadron level.

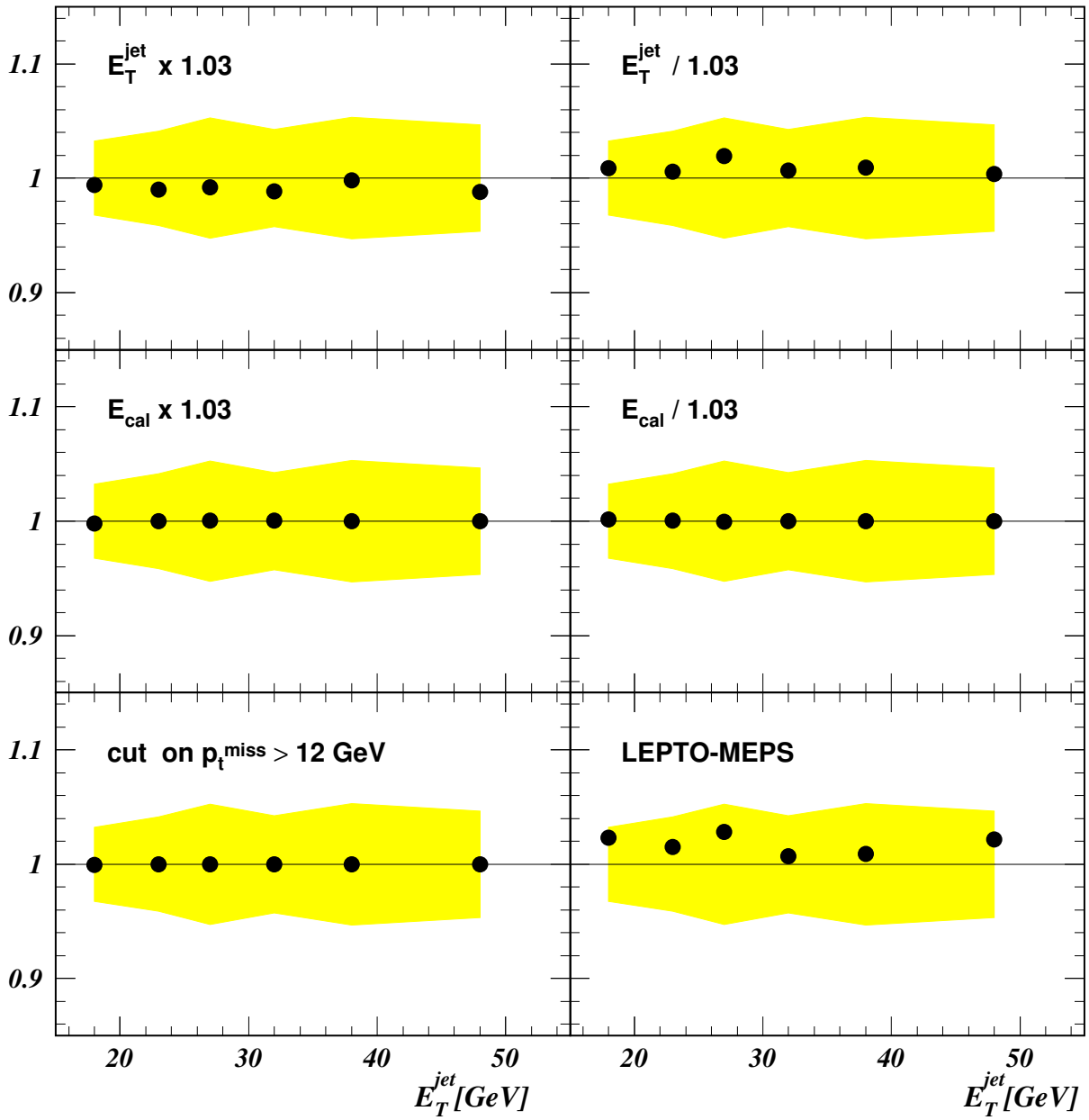

Figure 6.13 - Systematic uncertainties of the measured mean subjet multiplicity as a function of E_T^{jet}. The shaded band shows the statistical uncertainty of the data. a) the transverse energy of the jets, E_T^{jet}, is varied by ±3% b) the energy in the CAL is varied by ±3% c) the cut $\not{p}_t$ is raised from 11 to 12 GeV d) The Monte Carlo LEPTO-MEPS is used instead of ARIADNE-CDM to correct the data to hadron level.

Chapter 7

Results

The internal structure of the jets produced in charged current deep inelastic ep scattering has been investigated. An inclusive sample of jets with transverse energies $E_T^{jet} > 8$ GeV and pseudorapidity in the range between -1 and 2 has been selected. The kinematic region has been restricted to $Q^2 > 200$ GeV^2 and $y < 0.9$. The substructure of jets has been studied by means of the subjet multiplicity and the integrated and differential jet shape.

The measurement of the mean subjet multiplicity, $< n_{sbj} >$, as a function of the resolution scale y_{cut}, for jets in the η^{jet} range between -1 and 2 in different E_T^{jet} regions is shown in figure 7.1. The data have been corrected to the hadron level and the error bars show the statistical and systematic uncertainties added in quadrature. For comparison, the predictions of the leading-order (LO) Monte Carlo models of ARIADNE and LEPTO-MEPS are shown. The measured mean subjet multiplicity in all the regions of E_T^{jet} is well described by the predictions.

The dependence of the substructure of the jets with the jet pseudorapidity has also been studied. The mean subjet multiplicity as function of y_{cut} for jets in the E_T^{jet} range above 8 GeV in different η^{jet} regions has been measured and is shown in figure 7.2. Both Monte Carlo models CDM and MEPS, give a good description of the data. The mean subjet multiplicity for a fixed value of the resolution scale, $y_{cut} = 10^{-2}$, as a function of η^{jet} for jets with $E_T^{jet} > 8$ GeV is shown in figure 7.3 . No significant dependence of the subjet multiplicity on η^{jet}) is observed.

The mean subjet multiplicity at a fixed value of the resolution scale, $y_{cut} = 10^{-2}$, as a function of E_T^{jet} for jets with $-1 < \eta^{jet} < 2$ has also been measured and is shown in figure 7.4. It is observed that the mean subjet multiplicity decreases as E_T^{jet} increases. For comparisons, similiar measurements in neutral current DIS for $Q^2 > 125$ GeV^2 is shown in figure 7.4. The measured $< n_{sbj} >$ at fixed resolution scale, $y_{cut} = 10^{-2}$, in charged current and neutral current DIS are very similar.

A complementary way of studying the internal structure of jets is to through the measurement of the jet shapes. The integrated jet shape corrected to hadron level, $\Psi(r)$, for jets with $E_T^{jet} > 8$ GeV and η^{jet} between -1 and 2 is shown in figure 7.5. Both Monte Carlo models describe well the measurement although MEPS seems to do better. From this measurement it is concluded that around 95% of the jet transverse energy is contained in a cone of radius 0.7 in the $\eta - \phi$ plane around the

jet axis. The differential jet shape, $\rho(r)$, has also been measured. The differential jet shapes corrected to hadron level, for jets with $-1 < \eta^{jet} < 2$ in different E_T^{jet} regions are presented in CC DIS(open circles) for jets with $-1 < \eta^{jet} < 2$ in different in figure 7.6. For comparison, a similar measurement in NC DIS is shown. There is a good agreement between both measurements. The NC DIS measurements were performed with the cone jet algorithm while the CC measurements have been made using the K_T algorithm, which would explain the small differences seen at large value of the r.

It is concluded that Monte Carlo models which include parton cascades describe well the internal structure of the jets. Comparisons with similar measurements in neutral current interactions show that the internal structure of the jets is very similar. This similarity can be attributed to a large content of final-state quark jets in these two processes and, thus, the pattern of QCD radiation close to a primary quark is to a large extent independent of the hard scattering process.

The hadronic final state in charged current DIS can be characterized in terms of the production rate of jets, that is jet cross sections. The differential cross section for producing one or more jets, that is the inclusive jet cross section, has been measured as a function of the jet transverse energy, $d\sigma/dE_T^{jet}$ (see figure 7.7) and the jet pseudorapidity, $d\sigma/d\eta^{jet}$ (see figure 7.9). Jets with $-1 < \eta^{jet} < 2$ and $E_T^{jet} > 8$ GeV have been considered. The measurement has been restricted to the kinematic region defined by $Q^2 > 200$ GeV^2 and $y < 0.9$. In the figures, the inner error bars are the statistical uncertainties and the outer error bars are the statistical and uncorrelated systematic uncertainties added in quadrature. The shaded band is the correlated systematic uncertainty coming from the energy scale.

The measured $d\sigma/d\eta^{jet}$ has a maximum at $\eta^{jet} \sim 0.75$. The measured $d\sigma/dE_T^{jet}$ exhibits a fall-off of 3 orders of magnitude in the E_T^{jet} range studied. For $8 < E_T^{jet} < 20$ GeV the distribution displays almost no dependence on E_T^{jet}. This behaviour of $d\sigma/dE_T^{jet}$ as a function of E_T^{jet} in CC DIS is very different than that observed in NC DIS as seen in 7.8. The CC DIS cross section is found to fall with E_T^{jet} less rapidly and to approach the NC DIS cross section at $E_T^{jet} \sim 80$ GeV. This can be interpreted as due to the presence of a masive propagator in CC interactions. The shape and magnitude of the measured cross sections are described by the predictions of the Standard Model.

The measurement of the dijet cross sections in CC DIS for the two jets of highest E_T^{jet} with $E_T^{jet_{1,2}} > 8$ GeV and $-1 < \eta^{jet_{1,2}} < 2$ has been also performed. The dijet cross section as a function of E_T^{jet}, η^{jet} and the dijet invariant mass, m_{JJ}, are presented in figures 7.10,7.11 and 7.12.

The measured $d\sigma/d\eta^{jet}$ presents a maximum for $\eta^{jet} \sim 1$. The measured $d\sigma/dE_T^{jet}$ presents a steep fall-off of more than two orders of magnitude in the E_T^{jet} range considered. The shape of this distribution is different to that of the inclusive jet sample (see figure 7.7): the inclusive jet cross section is governed by the electroweak interactions and the mass of the intermediate gauge boson W whereas the dijet cross section is governed by QCD effects. Dijet invariant masses of up to ~ 60 GeV are accesible with the luminosity used in this analysis. The shape of the measured cross sections is described by the predictions of the CDM model, but the magnitude of the

measured cross sections is underestimated by typically $\sim 50\%$. The MEPS model gives a worse description of the shape of the data than the CDM model.

The model calculations predict well the shape and normalisation of the inclusive jet cross section but gives only the order of magitude and the rough features of the dijet cross section. This is because the inclusive jet cross section is very similar to the inclusive charged current cross section, which is governed by electroweak interaction and is well described by leading-order calculations (see equation 1.19). The dijet cross section is governed by QCD effects and accurate predictions require the pertubative calculations to be performed at least to next-to-leading order (NLO), since the higher-order corrections to the LO prediction are not negligible. The calculation of the NLO QCD predictions and an estimation of the theoretical uncertainties are in progress. The comparison of the improved calculations with the measurements presented here will allow a stringent test of the Standard Model.

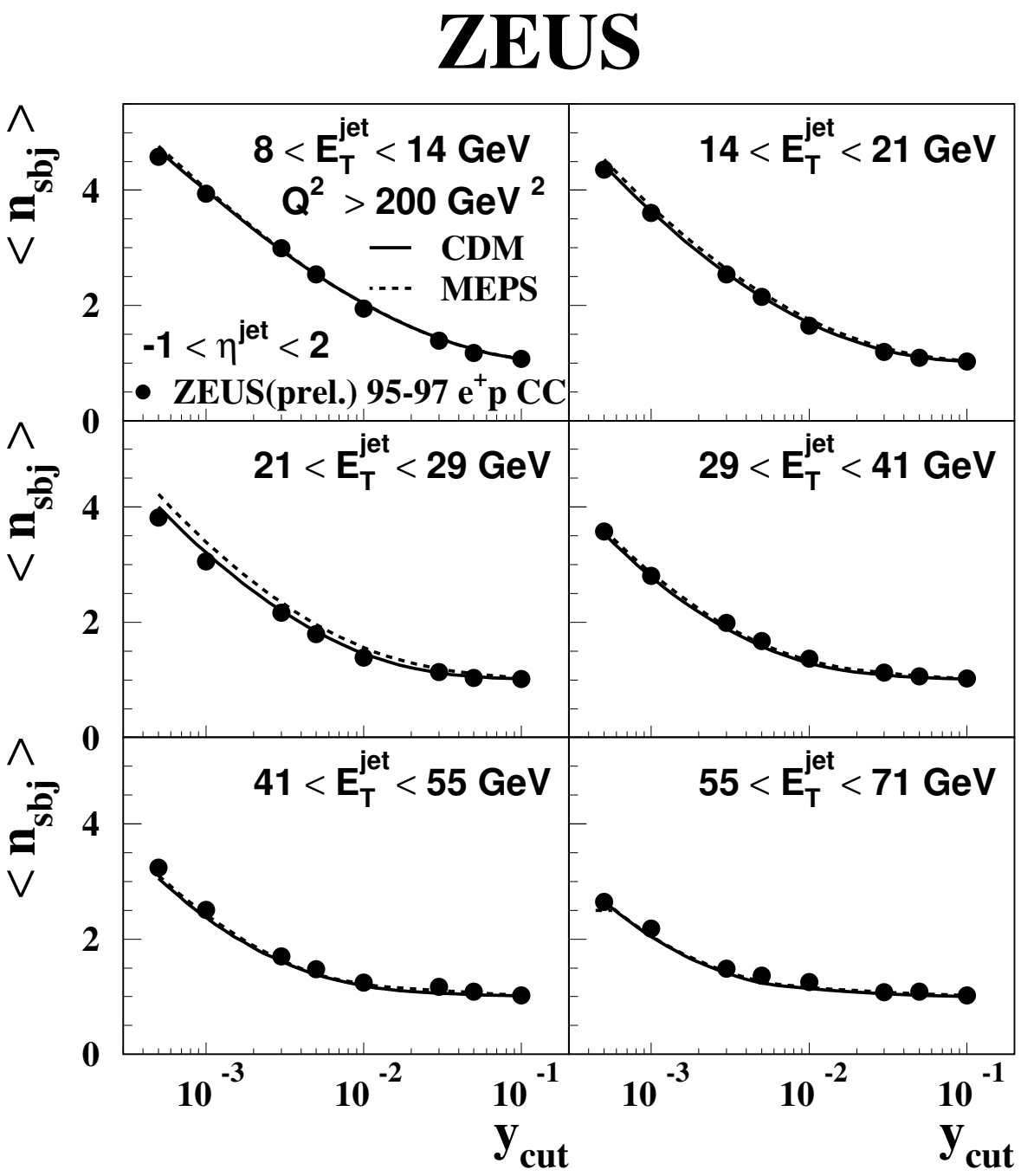

Figure 7.1 - Measured mean subjet multiplicity corrected to hadron level, $< n_{sbj} >$, as a function of y_{cut}, for jets in the η^{jet} range between -1 and 2 in different E_T^{jet} regions (black dots). The error bars show the statistical and systematic uncertainties added in quadrature. For comparison, the predictions of the Monte Carlo models of CDM (solid line) and MEPS (dashed line) are shown.

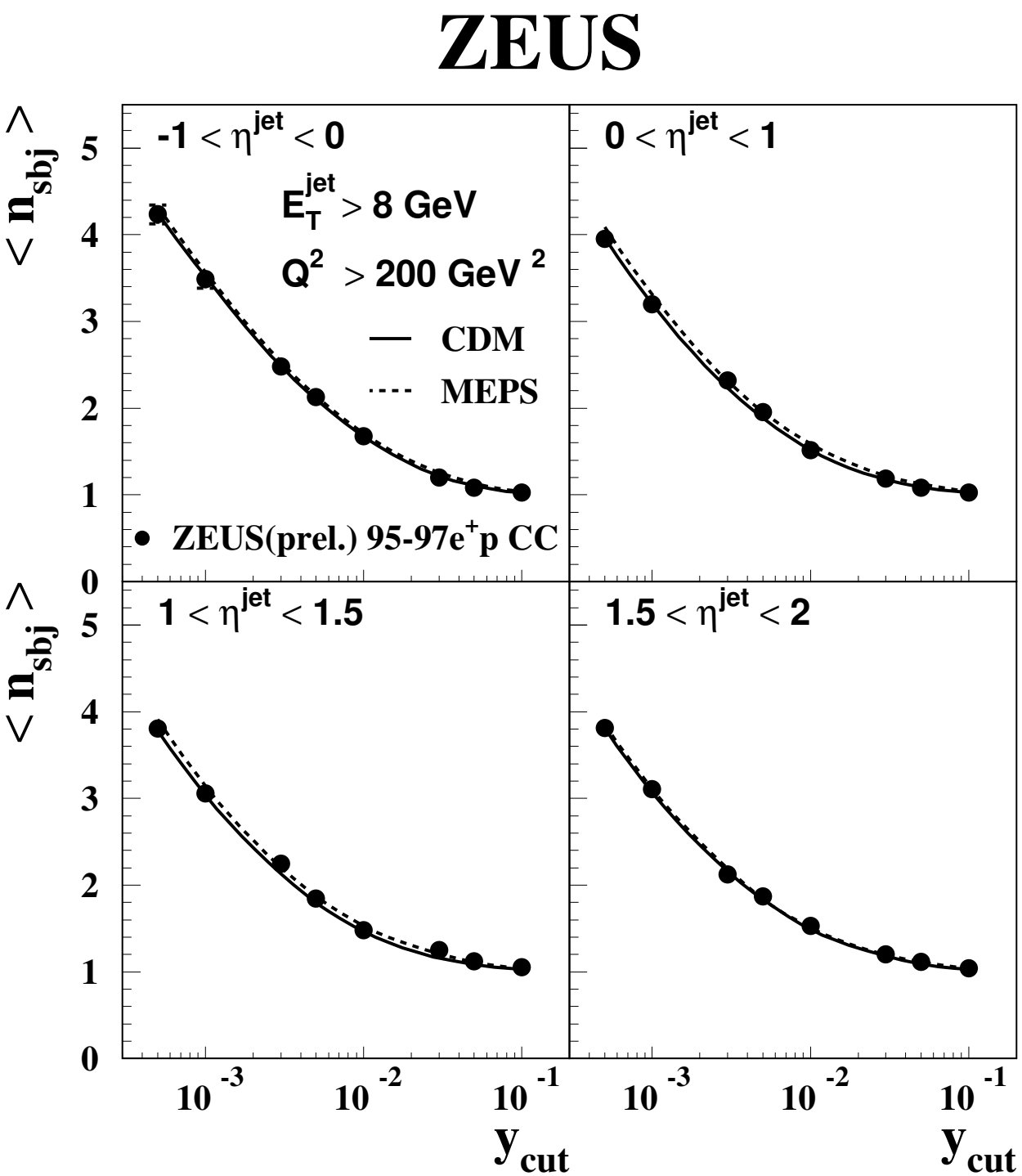

Figure 7.2 - Measured mean subjet multiplicity corrected to hadron level, $< n_{sbj} >$, as a function of y_{cut}, for jets in the E_T^{jet} range above 8 GeV in different η^{jet} regions (black dots). The error bars show the statistical and systematic uncertainties added in quadrature. For comparison, the predictions of the Monte Carlo models of CDM (solid line) and MEPS (dashed line) are shown.

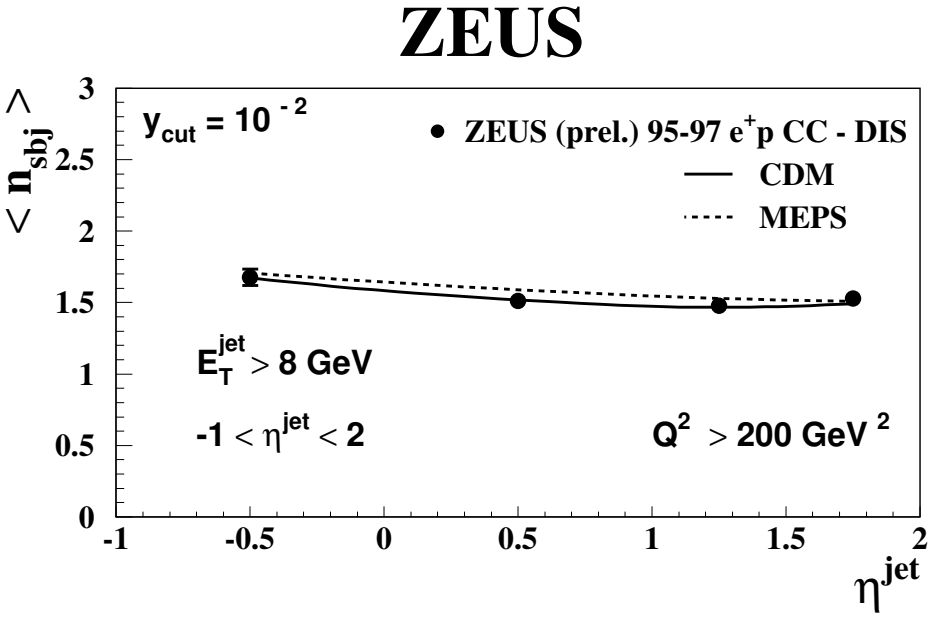

Figure 7.3 - Measured mean subjet multiplicity corrected to hadron level at a fixed value of $y_{cut} = 10^{-2}$ as a function of η^{jet} for jets with $E_T^{jet} > 8$ GeV (black dots). The error bars show the statistical and systematic uncertainties added in quadrature. For comparison, the predictions of the Monte Carlo models of CDM (solid line) and MEPS (dashed line) are shown.

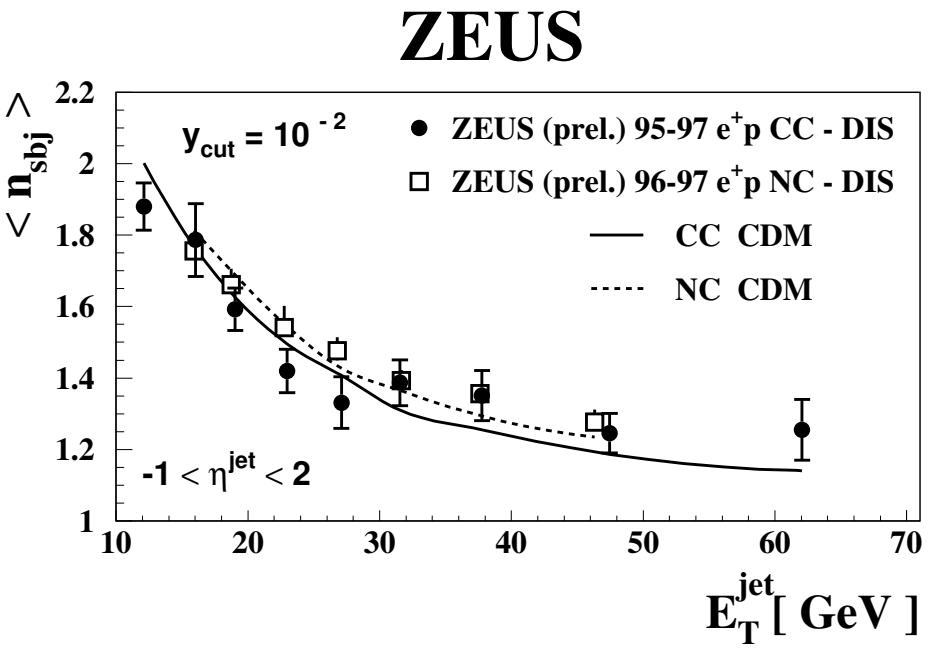

Figure 7.4 - Measured mean subjet multiplicity corrected to hadron level at a fixed value of $y_{cut} = 10^{-2}$ as a function of E_T^{jet} for jets with $-1 < \eta^{jet} < 2$ (black dots). For comparison, $< n_{sbj} >$ as a function of E_T^{jet} for NC DIS (open squares) at a fixed $y_{cut} = 10^{-2}$ is also shown.

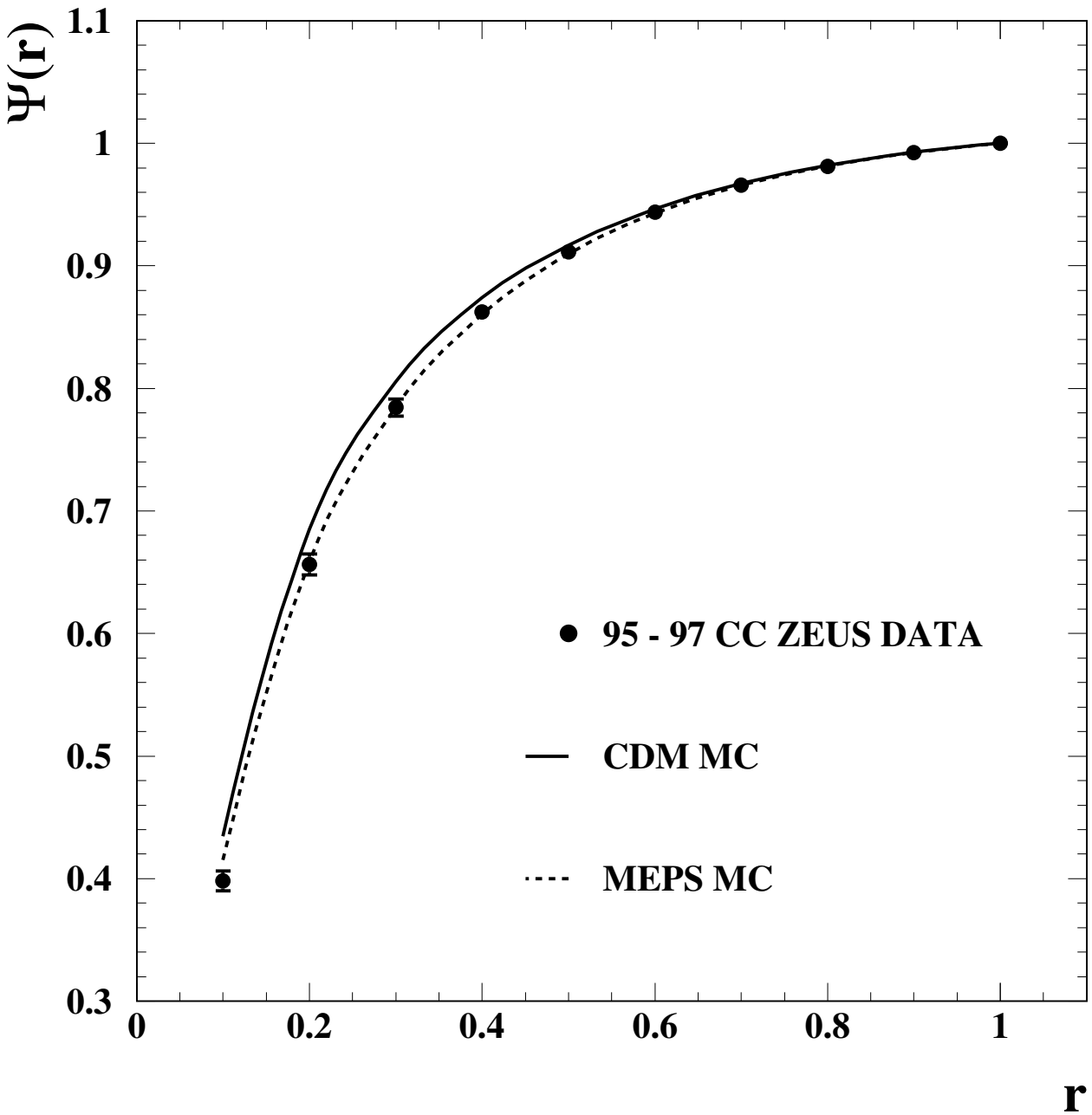

Figure 7.5 - Measured integrated jet shape corrected to hadron level, $\Psi(r)$, for jets with $E_T^{jet} > 8$ GeV and η^{jet} between -1 and 2 (black dots). For comparison, the predictions of the Monte Carlo models of CDM (solid line) and MEPS (dashed line) are shown.

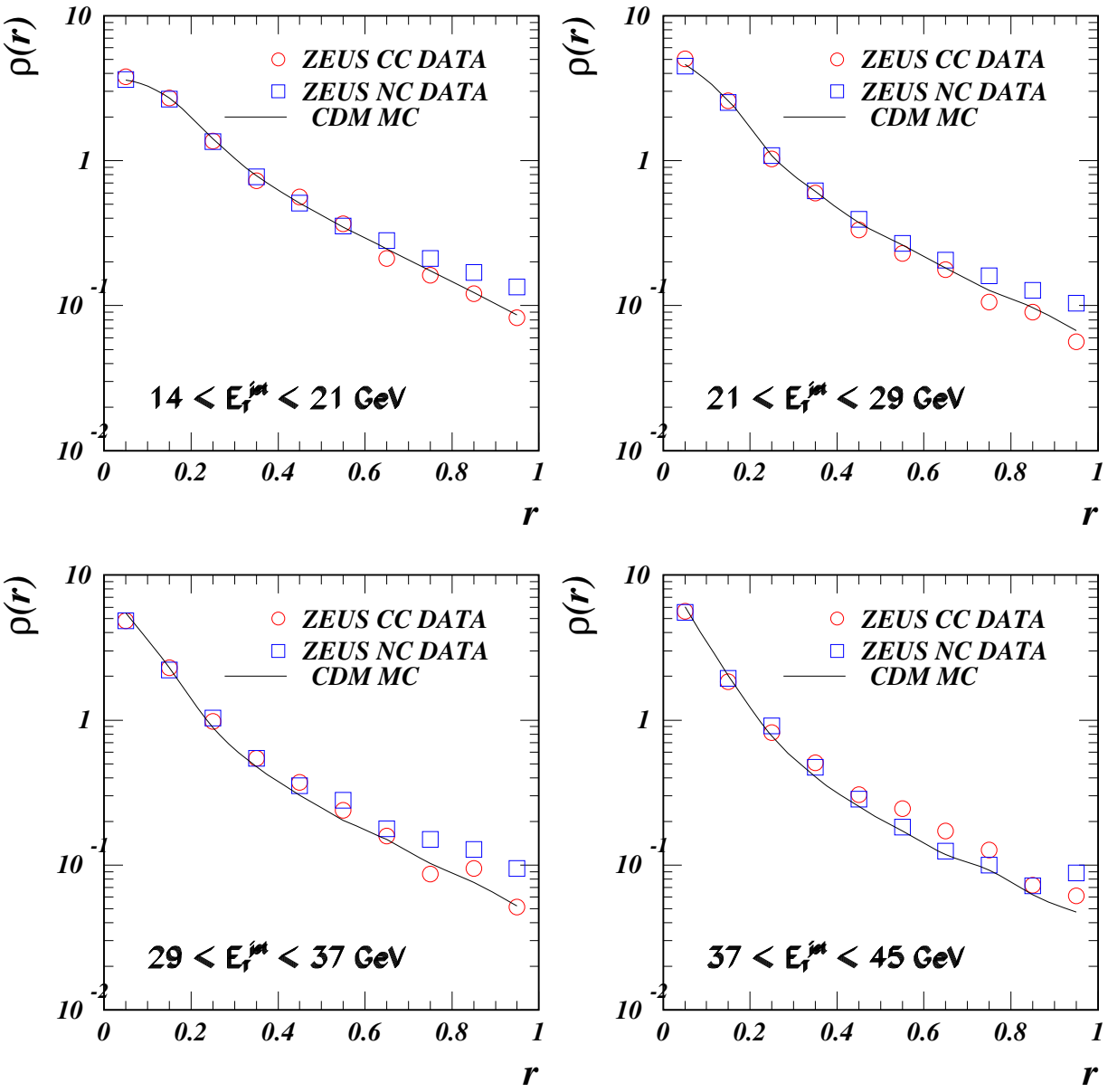

Figure 7.6 - Measured differential jet shapes corrected to hadron level, $\rho(r)$, in CC DIS for jets with $-1 < \eta^{jet} < 2$ in different E_T^{jet} regions (open circles). For comparison, a similar measurement in NC DIS (open squares) is shown.

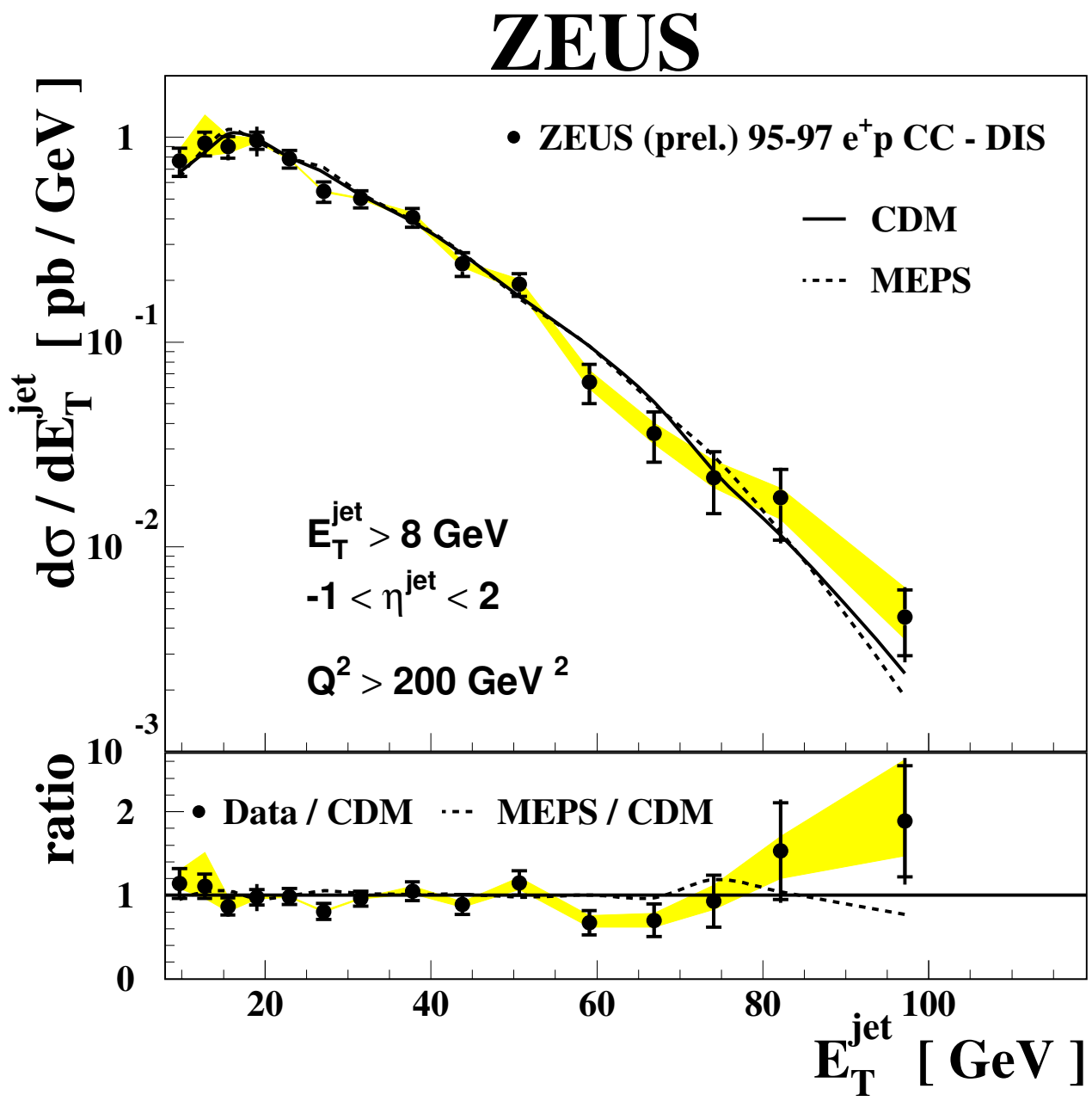

Figure 7.7 - Measured differential inclusive jet cross-section $d\sigma/dE_T^{jet}$ in CC DIS integrated over $-1 < \eta^{jet} < 2$ in the kinematic region defined by $Q^2 > 200$ GeV^2 and $y < 0.9$ (black dots). The inner error bars represent the statistical uncertainties of the data and the outer error bars show the statistical and the uncorrelated systematic uncertainties added in quadrature. The shaded band displays the uncertainty due to the correlated systematics. For comparison, the predictions of the Monte Carlo models of CDM (solid line) and MEPS (dashed line) are shown. In the lower part of the figure the ratio of the measured $d\sigma/dE_T^{jet}$ over the CDM Monte Carlo prediction is shown.

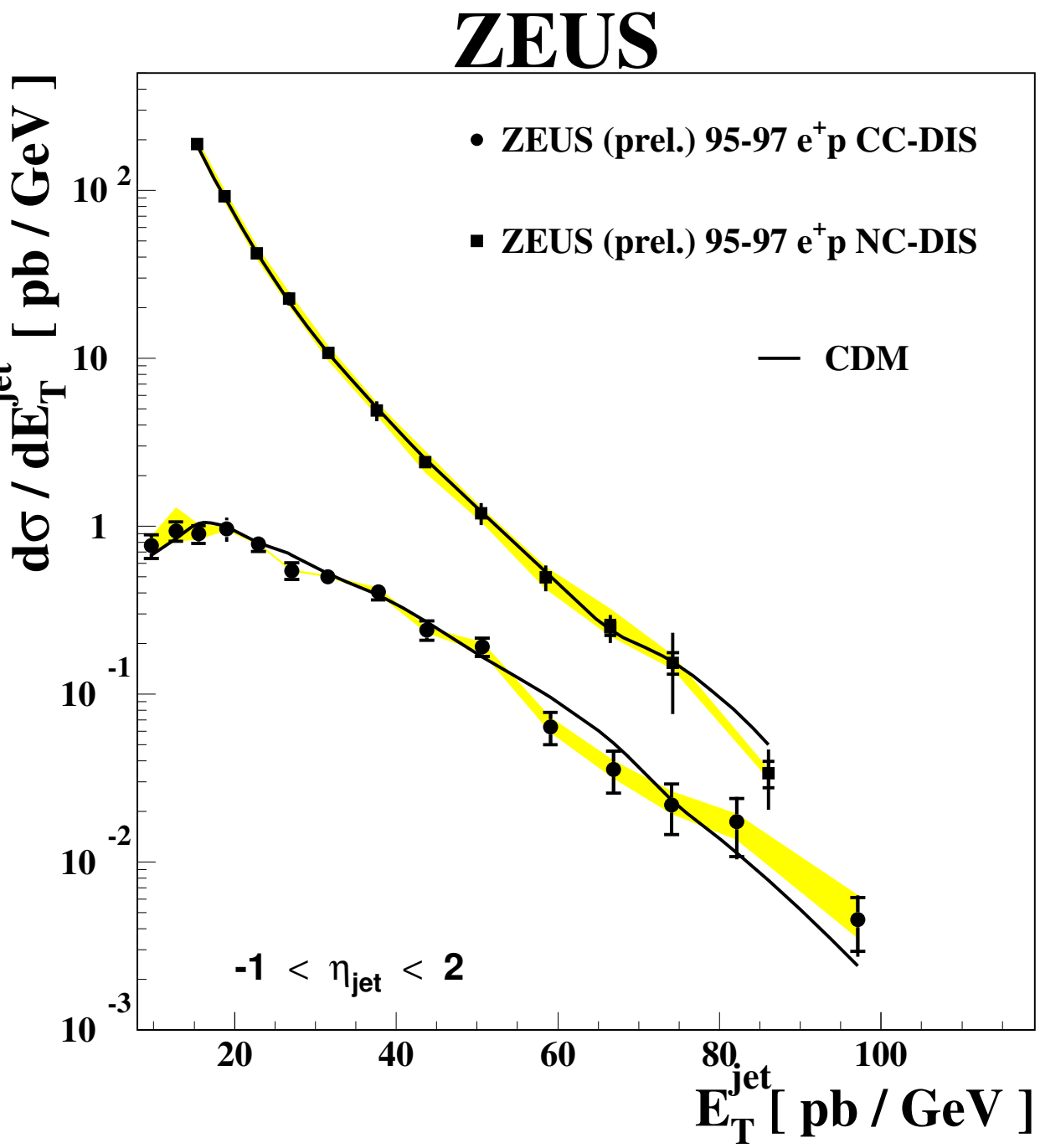

Figure 7.8 - Measured differential inclusive jet cross-section $d\sigma/dE_T^{jet}$ in CC DIS integrated over $-1 < \eta^{jet} < 2$ in the kinematic region defined by $Q^2 > 200$ GeV^2 and $y < 0.9$ (black dots). For comparison the inclusive jet cross-section $d\sigma/dE_T^{jet}$ in NC interactions (black squares) for $Q^2 > 125$ GeV^2 is shown. The inner error bars represent the statistical uncertainties of the data and the outer error bars show the statistical and the uncorrelated systematic uncertainties added in quadrature. The shaded band displays the uncertainty due to the correlated systematics. The prediction of the Monte Carlo model of CDM (solid line) is shown.

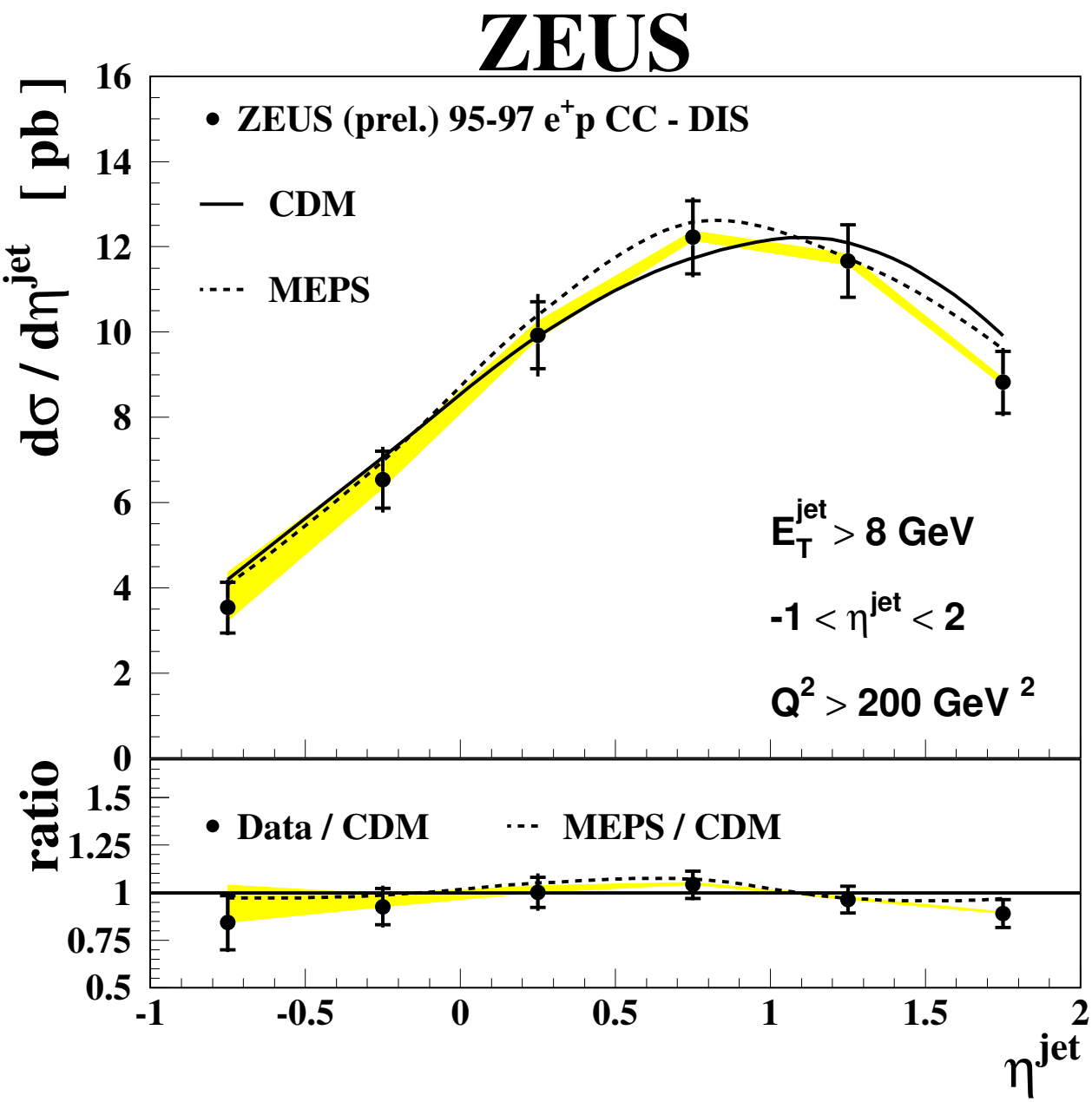

Figure 7.9 - Measured differential inclusive jet cross-section $d\sigma/d\eta^{jet}$ in CC DIS integrated over $E_T^{jet} > 8$ GeV in the kinematic region defined by $Q^2 > 200$ GeV^2 and $y < 0.9$ (black dots). The inner error bars represent the statistical uncertainties of the data and the outer error bars show the statistical and the uncorrelated systematic uncertainties added in quadrature. The shaded band displays the uncertainty due to the correlated systematics. For comparison, the predictions of the Monte Carlo models of CDM (solid line) and MEPS (dashed line) are shown. In the lower part of the figure the ratio of the measured $d\sigma/d\eta^{jet}$ over the CDM Monte Carlo prediction is shown.

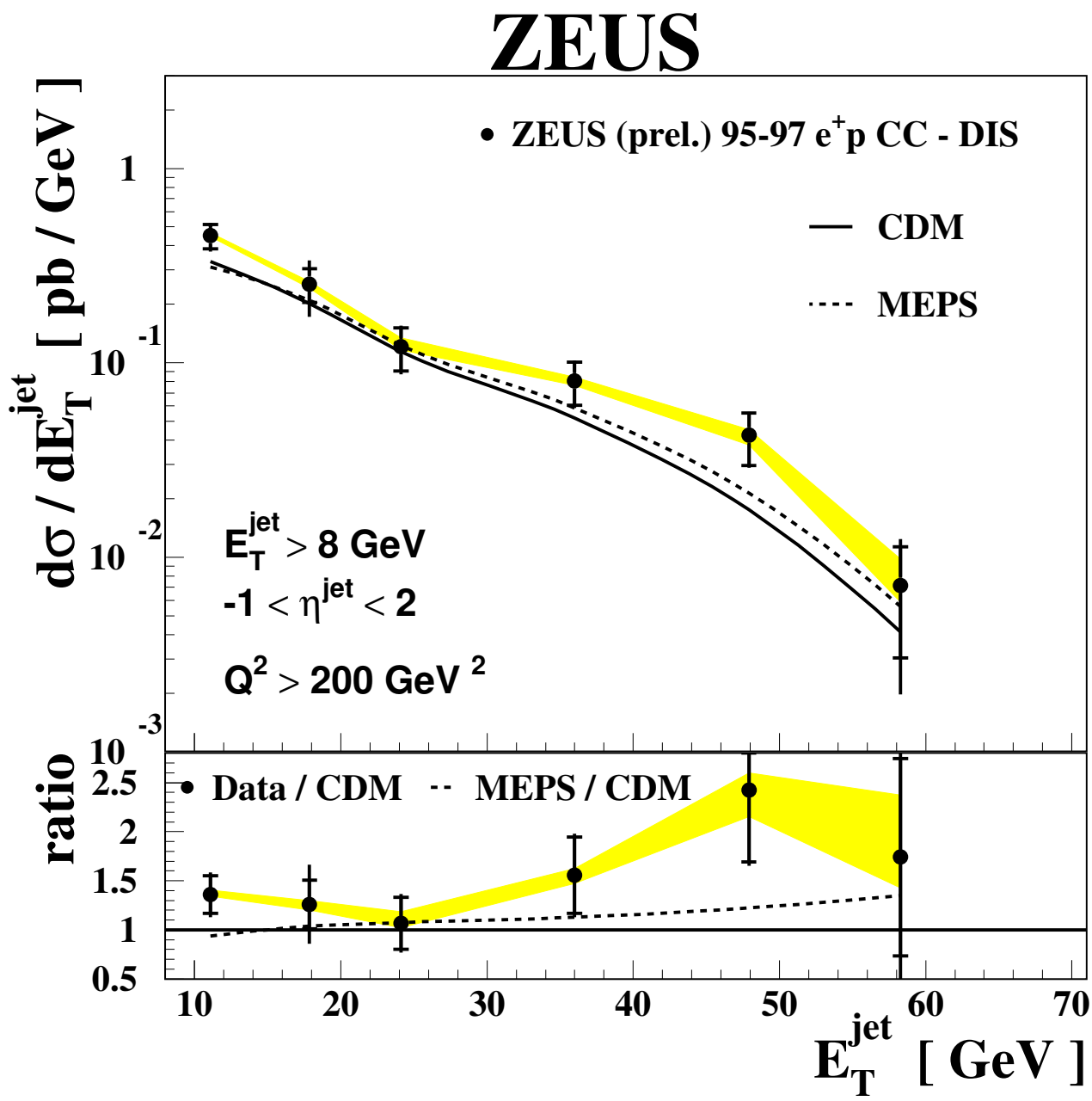

Figure 7.10 - Measured differential dijet jet cross-section $d\sigma/dE_T^{jet}$ integrated over $-1 < \eta^{jet} < 2$ in the kinematic region defined by $Q^2 > 200$ GeV^2 and $y < 0.9$ (black dots). The inner error bars represent the statistical uncertainties of the data, and the outer error bars show the statistical and the uncorrelated systematic uncertainties added in quadrature. The shaded band displays the uncertainty due to the correlated systematics. For comparison, the predictions of the Monte Carlo models of CDM (solid line) and MEPS (dashed line) are shown. In the lower part of the figure the ratio of the measured $d\sigma/dE_T^{jet}$ over the CDM Monte Carlo prediction is shown.

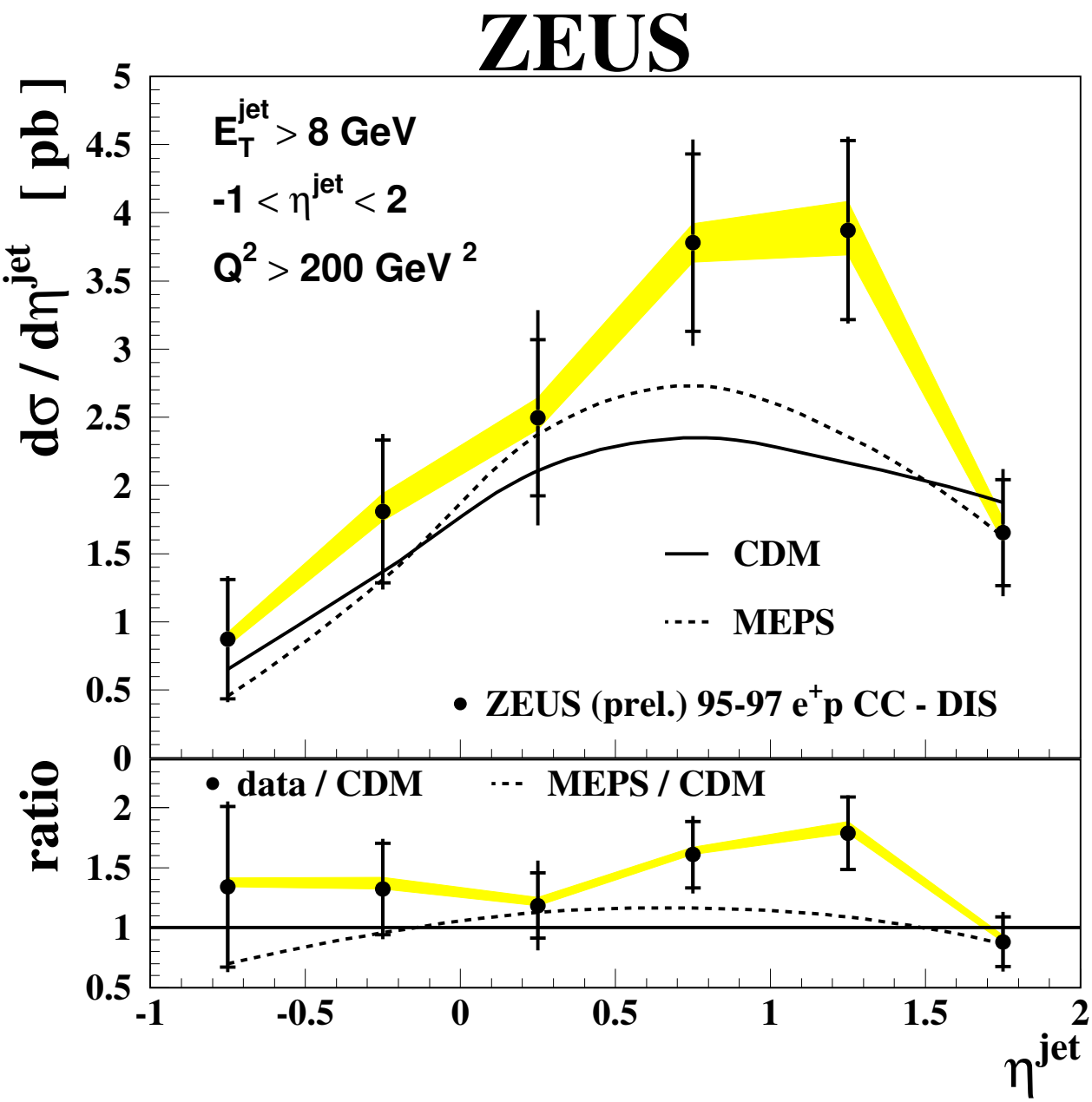

Figure 7.11 - Measured differential dijet cross-section $d\sigma/d\eta^{jet}$ integrated over $E_T^{jet} > 8$ GeV in the kinematic region defined by $Q^2 > 200$ GeV^2 and $y < 0.9$ (black dots). The inner error bars represent the statistical uncertainties of the data and the outer error bars show the statistical and the uncorrelated systematic uncertainties added in quadrature. The shaded band displays the uncertainty due to the correlated systematics. For comparison, the predictions of the Monte Carlo models of CDM (solid line) and MEPS (dashed line) are shown. In the lower part of the figure the ratio of the measured $d\sigma/d\eta^{jet}$ over the CDM Monte Carlo prediction is shown.

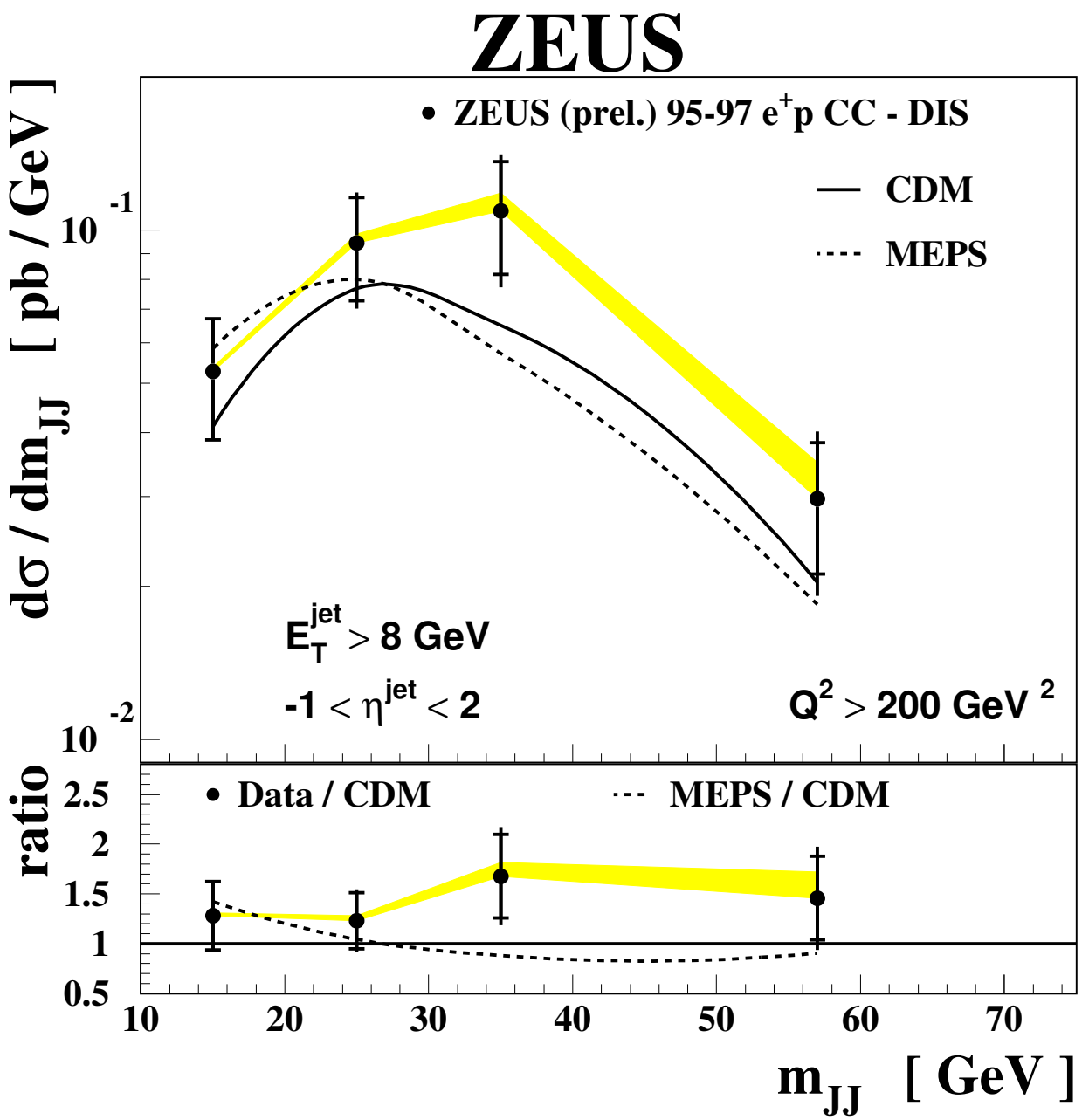

Figure 7.12 - Measured differential dijet cross-section $d\sigma/dm_{JJ}$ integrated over $-1 < \eta^{jet} < 2$ and $E_T^{jet} > 8$ GeV in the kinematic region defined by $Q^2 > 200$ GeV^2 and $y < 0.9$ (black dots). The inner error bars represent the statistical uncertainties of the data and the outer error bars show the statistical and the uncorrelated systematic uncertainties added in quadrature. The shaded band displays the uncertainty due to the correlated systematics. For comparison, the predictions of the Monte Carlo models of CDM (solid line) and MEPS (dashed line) are shown. In the lower part of the figure the ratio of the measured $d\sigma/dm_{JJ}$ over the CDM Monte Carlo prediction is shown.

Chapter 8

Conclusions

The hadronic final state in Charged Current Deep Inelastic Scattering in the kinematic range $Q^2 > 200 GeV^2$ and $y < 0.9$ has been studied by measuring the reaction $e^+p \rightarrow \overline{\nu_e} + +jet(s) + X$ with the ZEUS detector at HERA using an integrated luminosity of 44.97 pb^{-1}. Events having one or more jets with transverse energies $E_T^{jet} > 8$ GeV in the final state have been selected using the longitudinally invariant k_T algorithm in the laboratory frame of reference. The data is compared with the predictions of Leading-Order(LO) perturbative QCD using the CTEQ4 parametrisations of the parton density functions.

The inclusive jet cross sections for jets with $E_T^{jet} > 8$ GeV and $-1 < \eta^{jet_{1,2}} < 2$ has been measured as a function of $E_T^{jet}$and η^{jet}. The behaviour of $d\sigma/dE_T^{jet}$ as a function of E_T^{jet} in CC is very different than the one observed in NC. The CC cross section is found to fall with E_T^{jet} less rapidly and to approach the NC cross section of $E_T^{jet} \sim 80$ GeV. This can be interpreted as due to the presence of a masive propagator in CC events. The shape and magnitude of the measured cross sections are described well by the predictions.

The measurement of the dijet cross sections in CC for the two highest E_T jets with $E_T^{jet_{1,2}} > 8$ GeV and $-1 < \eta^{jet_{1,2}} < 2$ has been performed. The shape of $d\sigma/dE_T^{jet}$ is different to the one observed in the inclusive jet sample: the inclusive jet cross section is governed by electroweak interactions and the mass of the intermediate gauge boson W whereas the dijet cross section is governed by QCD effects. Dijet invariant masses of up to ~ 60 GeV are accesible with the luminosity used in this analysis. The shape of the measured cross sections is described by the predictions of the CDM model, but it underestimates the magnitude of the measured cross sections by typically $\sim 50\%$. The MEPS model gives a worse description of the shape of the data than the CDM model does.

Also, the internal structure of jets in Charged Current events has been studied in terms of the jet shape and subjet multiplicity. Both observables are well described by LO Monte Carlos. No significant dependence of the internal structure of jets with η^{jet} is observed. The subjet multiplicity decreases as E_T^{jet} increases, that is the jets become narrower as E_T^{jet} increases.

Acknowledments

I am deeply grateful to Prof. Fernando Barreiro and Prof. Luis Labarga for their continuous support, affection and for giving me the opportunity to join the ZEUS experiment and to study interesting physics topics.

I sincerely thank to Prof. Juan Terrón for his guidance, valuable advice and suggestions. I also thank both Prof. Jose del Peso and Juan Terrón for reading and commenting on this manuscript. I am also very grateful to Dr. Claudia Glasman for her enormous help during the analysis.

I would like to express my gratitude to Dr. Dorian Kçira, who has helped me so much while writing this manuscript. Finally, particular thanks to Oscar González who has supported and helped me so much.

I desire all the best for all of them.

Bibliography

[Ab95] H. Abramowitz, A. Caldwell, R. Sinkus. *Neural Network based electron identification in the ZEUS Calorimeter* DESY 95-054 (1995).
R. Sinkus. *Nucl. Instrum. Methods* **A361** 290 (1995).

[Al77] G. Altarelli and G. Parisi. *Nucl. Phys.* **B126** 298 (1977).
V.N. Gribov and L.N. Lipatov. *Sov. J. Nucl Phys.* **15** 438 (1972).
L.N. Lipatov. *Sov. J. Nucl. Phys.* **20** 96 (1975).
Y.L. Dokshitzer. *Sov. Phys. JETP.* **46** 641 (1977).

[An92] J. Andruskow et al. *DESY 92-066* (1992).
K. Piotrzkowski. *DESY F35D-93-06* (1993).

[Ba95] L.A.T. Bauerdick et al. *DESY-95-236* (1995).

[Be34] H. Bethe and W. Heitler. *Proc. Roy. Soc.* **A146** 83 (1934).

[Bl69] E.D. Bloom et al. *Phys. Rev. Lett.* **23** 930 (1969). W. Pankofski. *Proceedings of the International Conference in High Energy Physics* Vienne / Austria (1968).

[Br87] R. Brun et al. *Geant3.13* CERN DD/EE/84-1.

[Br89] R. Brun et al. *GEANT3, CERN DD/EE/81-1* (1989).

[Ca69] C.G. Callan and D. Gross. *Phys. Rev. Lett.* **22** 156 (1969).

[Ca93] S. Catani et al. *Nucl. Phys.* **B406** 187 (1993)
S.D. Ellis and D.E. Soper. *Phys. Rev.* **D48** 3160 (1993).

[Ci88] M. Ciafaloni *Nucl. Phys.* B **296** 49 (1988)
S. Catani, F. Fiorani and G. Marchesini, *Phys. Lett.* B **234** 339 (1990); *Nucl. Phys.* B **336** 18 (1990).

[Co85] J.C.D. Collins, D.E. Soper and G. Sterman. *Nucl. Phys. B* **261** 104 (1985).

[De91] M. Derrick et al. *Nucl. Instr. and Meth.* **A309** 77 (1991)
A. Andresen et al. *Nucl. Instr. and Meth.* **A309** 101 (1991)
B. Bernstein et al. *Nucl. Instr. and Meth.* **A336** 23 (1993)

[DE94] DESY. *Annual report* (1994).

[El92] S.D. Ellis, Z. Kunszt, D.E. Soper, *Phys. Rev. Lett.* **69** 3615 (1992).

[El96] R.K. Ellis, W.J. Stirling and B.R. Webber *QCD and Collider Physics*. Cambridge Unversity Press (1996).

[Fe69] R.P. Feynman. *Phys. Rev. Lett.* **23** 1415 (1969).

[Fi93] S.M. Fisher et al. *ADAMO Entitiy-Relationship Programming System : User's Guide* CERN (1993).

[Fo93] B. Foster et al. *Nucl. Instr. and Meth.* **A338** 254 (1993).

[Gl61] S.L. Glashow. *Nucl. Phys.* **22** 579 (1961).
A. Salam. *"Weak and Electromagnetic Interactions" - Proceedings of The Nobel Symposium / Lerum, Sweden* (1968).
S. Weinberg. *Phys. Rev. Lett.* **19** 1264 (1967).

[Ge64] M. Gell-Mann. *Phys. Lett.* **8** 214 (1964).
G. Zweig. *CERN-8192/TH 401* (1964).
G. Zweig. *CERN-8419/TH 402* (1964).

[Ha84] F. Halzen and A.D. Martin. *Quarks and Leptons*.
(John Wiley Sons Inc., New York, 1984).

[HB94] HERA-B Collaboration. *Technical Design Report* DESY-PRC 95/01 (1995).

[HE93] HERMES Collaboration. *Technical Design Report* (1993).

[Ho53] R. Hofstadter et al. *Phys. Rev.* **91** 422 (1953).
R. Hofstadter, R.W. McAllister . *Phys. Rev.* **98** 217 (1955).
R. Hofstadter. *Ann. Rev. Nucl. Part. Sci.* **7** 458 (1957).

[Hu90] J.E. Huth et al., *Proc. of the 1990 DPF Summer Study on High Energy Physics, Colorado, edited by E¿L¿ Berger*, (World Scientific, Singapore, 1992) 134.

[In97] G. Ingelman, A. Edin and J. Rathsman, *"LEPTO 6.5 - A Monte Carlo Generator for Deep Inelastic Lepton-Nucleon Scattering"* Comput. Phys. Commun. **101**, 108 (1997).

[Ja79] M.Krawczyk et al., *Proc. of the study for an* ep *facility for Europe*, DESY79-48 391

[Kr98] A.Kruse et al., *MUFFINCUP - A Wrapper for MUFFIN*, ZEUS-NOTE 98-025

[Ku76] E.A. Kuraev, L.N. Lipatov and V.S. Fadin. *Sov. Phys. JETP* **44** 443 (1976).
E.A. Kuraev, L.N. Lipatov and V.S. Fadin. *Sov. Phys. JETP* **45** 199 (1977).
Y.Y. Balitzki and L.N. Lipatov. *Sov. J. Nucl. Phys.* **28** 822 (1978).

[Kw92] A. Kwiatkowski, H. Spiesberger and H. J. Mohring, *"HERACLES: AN EVENT GENERATOR FOR e p INTERACTIONS AT HERA ENERGIES INCLUDING RADIATIVE PROCESSES: VERSION 1.0,"* Comput. Phys. Commun. **69**, 155 (1992).

[LE00] The LEP Higgs Working Group. *A Hint of the Standard Model Higgs Boson at LEP* (2000).

[Lo92] E. Lohrmann. *Hochenergiephysik* (1992).

[lö02] L.Lönnblad, *"ARIADNE version 4: A Program for simulation of QCD cascades implementing the color dipole model,"* Comput. Phys. Commun. **71**, 15 (1992).

[Ne00] Neutrino 2000. *XIX International Conference on Neutrino Physics and Astrophysics - Sudbury/Canada June 16-21* (2000).
`http://nu2000.sno.laurentian.ca`

[Pa00] Particle Data Group *Eur. Phys. J.* **C 15** (2000).

[Pl93] H. Plothow-Besch, *"PDFLIB: A Library of all available parton density functions of the nucleon, the pion and the photon and the corresponding alpha-s calculations"* Comput. Phys. Commun. **75**, 396 (1993).

[Sa98] A. Savin. *Study of Calorimeter Noise in the 1996 Data* ZEUS-Note 98-07.

[Sc91] G. A. Schuler and H. Spiesberger, *"DJANGO: The Interface for the event generators HERACLES and LEPTO,"* In *Hamburg 1991, Proceedings, Physics at HERA, vol. 3* 1419-1432.

[Se95] M.H.Seymour. *Jets in QCD* hep-ph/9506421, CERN-TH/95-176.

[Sj94] T. Sjöstrand. *Computer Phys. Commun.* **82** 74 (1994).

[Sm84] W.H. Smith et al. *'The ZEUS Trigger System'* ZEUS-note 89-084.

[Ui92] H. Uijterwaal. *'The Global Second Level Trigger for ZEUS'* PhD Thesis - University of Amsterdam (1992).

[Yo92] C. Youngman. *'The ZEUS Data Acquistion System'* DESY 92-150A .

[ZE93] ZEUS Collaboration, *The ZEUS Detector* Status Report (1993).

[ZE01] ZEUS. Collab. *Measurement of jet cross sections and jet substructure in charged current deep inelastic scattering at HERA* . Contributed paper to the International Europhysics Conference on High Energy Physics, Budapest, Hungary(2001). Abstract 646.

Claudia Glasman and Mónica Vázquez *Measurement of jet cross sections and jet substructure in charged current deep inelastic scattering at HERA* . ZEUS-Note 01-023